Search for Ultra High Energy Photons with the Hybrid Detector of the Telescope Array Experiment

(テレスコープアレイ実験ハイブリッド検出器による極高エネルギーガンマ線探索)

理学研究科
数物系専攻

平成26年度

Katsuya Yamazaki
(山﨑 勝也)

Search for Ultra High Energy Photons with the Hybrid Detector of the Telescope Array Experiment

Katsuya Yamazaki

Abstract

After the discovery of cosmic rays many of the features of cosmic rays, such as the energy spectrum, primary mass composition, and anisotropies are studied in the wide energy range from 10^9 eV to beyond 10^{20} eV. In particular, recent progresses of cosmic ray studies in the energy range above 10^{18} eV, called *ultra high energy cosmic rays* (UHECRs), are remarkable. However, the origins of UHECRs are still unknown. This is one of the largest problem in the area of UHECR study.

Currently, there are two major experiments for observing and studying UHECRs, that is the Telescope Array (TA) experiment in the northern and Pierre Auger Observatory (PAO) in the southern hemisphere. These two observatories publish the results of the energy spectrum, primary mass composition, and anisotropy studies. However, the nature of UHECRs has not been fully revealed yet, especially origins of UHECRs have not been discovered.

In this thesis I will report the studies for the nature of extensive air showers induced by primary photons and the observational results of searching for UHE photons as another approach to understand the nature of UHECRs. The flux of UHE photons depends on the major composition of UHECRs due to their generation and propagation mechanisms. Furthermore, they arrive at the Earth with no magnetic deflection. Thus, the detection of UHE photons and determination of their flux can be critical clues to reveal the nature and origins UHECRs.

TA is a hybrid detector consisting of an array of scintillator detectors and fluorescence detector stations. This hybrid detector measures incoming cosmic ray induced air showers with about 700 km^2 effective detection area in the central Utah. We searched for UHE photons using the TA detectors in the hybrid mode. The hybrid data set used in this thesis were accumulated in the period from March 2008 to July 2013.

The depth of shower maximum ($\mathrm{X}_{\mathrm{max}}$) is used to select *photon-like* events since photon induced air showers are expected to have significantly larger X_{max} in the atmosphere than hadroni induced showers. In order to determine a selection criterion a full Monte Carlo (MC) simulation including air shower simulations and hybrid

detector simulations are used.

As a result of UHE photon search we found 24, 11, 3, and 0 photon-like events in the energy range greater than 2, 3, 5, and 10 EeV, respectively. The number of photon-like events found in the hybrid data set are consistent with the number of expected false selected events, which are caused by primary protons. Therefore, the photon fraction upper limits with 95% confidence level are derived from the numbers of photon-like events. In order to calculate the upper limits the detection bias of primary photons and primary protons and the selection efficiency are calculated with the MC simulations. The systematic uncertainty on the photon fractions which comes from the uncertainty on the energy determination with hybrid analysis are also considered. Finally, the upper limits of photon fractions are derived as 9.4, 9.0, 9.8, and 26.6% in the energy range greater than 2, 3, 5, and 10 EeV, respectively. These upper limits are the first result which measured by the hybrid detection technique in the northern hemisphere.

As a result of the upper limits the predicted photon fraction with top-down models which considered in this thesis are not constrained, but in consideration of combination with the TA surface detector result, super heavy dark matter models and topological defect model of the UHECR generation are constrained with 95% confidence level, and Z-Burst model are survived with these upper limits in the norther hemisphere. In addition, the result ensure the uncertainties caused by photon contaminations on other analyses, such as composition analysis using average of the $X_{\rm max}$, are reasonably small.

Acknowledgements

I wish to express my sincere appreciation to my supervisor Dr. Shoichi Ogio[1], Associate Professor, for the opportunity to be part of the Telescope Array collaboration, and for his many advices and supports for my thesis. I learned many things from him. I also would like to offer my great appreciation to Dr. Yoshio Hayashi[1], Professor, and Dr. Koji Kojima[1], Visiting Professor, they has given me many helpful advices and discussions.

I would like offer my appreciation to Dr. Masaki Fukushima[2], Professor, and Dr. Hiroyuki Sagawa[2], Associate Professor for the great management of the Telescope Array experiment and for the helpful discussions. I also express my appreciation to Dr. Gordon B. Thomson[3], Professor, Dr. John N. Matthews[3], Research Professor, for their kindly support at the US.

I wish to offer my deep gratitude to Dr. Toshihiro Fujii[4], Dr. Daisuke Ikeda[2], and Dr. Yuichiro Tameda[2]. They have been done the pioneer work on developing the analysis software package for fluorescence detectors, and also they have given me great helps and advices. I also would like to express my deep gratitude to Dr. Benjamin Stokes[3] for helpful technical advices and helps.

Telescope Array is supported by many staff members that help with issues both technical and administrative work. Without their support neither this work nor any other would be possible. These people include Mr. Gary McDonough, Mr. Frank Misak, Mr. Jeremy Smith, Dr. Robert Cady, Mr. Stan Thomas, Mr. Dave Barr, and Ms. Cindy Barr.

I would like to thank the members of the Telescope Array collaboration for making the chance to participate in the grate collaboration, especially I would like to thank Dr. Kazumasa Kawata[2], Project Assistant Professor, Dr. Eiji Kido[2], Project Assistant Professor, Dr. Toshiyuki Nonaka[2], Assistant Professor, Dr. Takeshi Okuda5 Project Assistant Professor,, Dr. Nobuyuki Sakurai[2], Project Assistant Professor, Dr. Tatsunobu Shibata[2], Project Assistant Professor, Dr. Masahiro Takeda[2], Assistant Professor, Dr. Hisao Tokuno[2], Project Assistant Professor, Dr. Takayuki Tomida[6], Assistant Professor, Dr. Yoshiki Tsunesada[7], Assistant Professor, and Dr. Shigeharu Udo[8], Assistant Professor, for many helps and comments.

I would like to thank the members of our laboratory including graduated students, Ms. Mayuko Minamino, Mr. Yu Yamashita, Mr. Daisuke Matsumiya, Mr. Kazuyuki Kuramoto, Mr. Ryo Yamane, Mr. Yasuhisa Yoneda, Mr. Hyouei Nanpei, Mr. Takashi Goto, Mr. Shogo Kobayashi, Ms. Ayaka Mori, Mr. Junya Kobayashi, Mr. Atsushi Terano, Mr. Yasuhiro Yamaguchi, Mr. Shogo Konishi, Mr. Shingo Wachi, Mr. Yoshiki Nishimoto, Ms. Mika Yamamoto, Mr. Shoichi Kishigami, Mr. Ryota Onogi, Mr. Yuichi Takahashi for their pleasant communications and encouragements.

Finally, I am deeply grateful to my family, especially Yasuo Yamazaki and Miki Yamazki for numerous supports and encouragements, and also I would like to thank Naho Sasaki for kindly encouragements.

[1] Graduate School of Science, Osaka City University

[2] Institute for Cosmic Ray Research, University of Tokyo

[3] Physics and Astronomy, University of Utah

[4] Kavli Institute for Cosmological Physics, University of Chicago

[5] Department of Physical Sciences, Ritsumeikan University

[6] Faculty of Engineering, Department of Computer Science&Engineering, Shinshu University

[7] Graduate School of Science and Engineering, Tokyo Institute of Technology

[8] Faculty of Engineering, Kanagawa University

The Telescope Array experiment is supported by the Japan Society for the Promotion of Science through Grants-in-Aid for Scientific Research on Specially Promoted Research (21000002) “Extreme Phenomena in the Universe Explored by Highest Energy Cosmic Rays”, Grant-in-Aid for Scientific Research(B) (20340057) “Calibrations of atmospheric fluorescence detectors of the Telescope Array experiment using a portable UV laser”, and the Inter-University Research Program of the Institute for Cosmic Ray Research; by the U.S. National Science Foundation awards PHY-0307098, PHY-0601915, PHY-0703893, PHY-0758342, PHY-0848320, PHY-1069280, and PHY-1069286 (Utah) and PHY-0649681 (Rutgers); by the National Research Foundation of Korea (2006-0050031, 2007-0056005, 2007-0093860, 2010-0011378, 2010-0028071, R32-10130); by the Russian Academy of Sciences, RFBR grants 10-02-01406a and 11-02-01528a (INR), IISN project No. 4.4509.10 and Belgian Science Policy under IUAP VI/11 (ULB). The foundations of Dr. Ezekiel R. and Edna Wattis Dumke, Willard L. Eccles and the George S. and Dolores Dore Eccles all helped with generous donations. The State of Utah supported the project through its Economic Development Board, and the University of Utah through the Office of the Vice President for Research. The experimental site became available through the cooperation of the Utah School and Institutional Trust Lands Administration (SITLA), U.S. Bureau of Land Management and the U.S. Air Force. We also wish to thank the people and the officials of Millard County, Utah, for their steadfast and warm support. We gratefully acknowledge the contributions from the technical staffs of our home institutions as well as the University of Utah Center for High Performance Computing (CHPC) and computing system at Institute for Cosmic Ray Research (ICRR) of University of Tokyo.

This work is supported by the Japan Society for the Promotion of Science (JSPS) through Grant-in-Aid for JSPS Fellows and by the Japan Student Services Organization (JASSO) through Student Exchange Support Program (Scholarship for Short-Term Study Abroad).

Contents

List of Figures

List of Tables

Chapter 1

Introduction

Cosmic rays are relativistic energy particles traveling through the universe, some of these particles reach the Earth. They were firstly discovered by V. F. Hess in 1912. After the discovery, cosmic rays have been measured in the broad energy range which is form 10^8 eV to beyond 10^{20} eV.

The energy spectrum of cosmic rays roughly follow a power low with the index of -3, but some fine structures, such as bends and dips, can be found in the spectrum [1]. These structures are changes of the power low index, and they are called "knee" (at around $10^{15.5}$ eV), "second knee" (at around $10^{17.5}$ eV), "ankle" (at around $10^{18.5}$ eV) and "cutoff" (at around $10^{19.6}$ eV), respectively. In order to understand the nature of these structures, the chemical composition of cosmic rays in each energy range is also important. Furthermore, the anisotropies in the distribution of cosmic ray arrival directions is also important keys to discover origins of cosmic rays and reveal the nature of the cosmic ray physics.

We have not understood all of the nature of cosmic rays, but it is widely believed low energy ($\leq 10^{15}$ eV) cosmic rays are accelerated by SNR shocks and propagate through the galactic halo. On the other hand, the nature of cosmic rays with energies greater then 10^{18} eV, which are called Ultra High Energy Cosmic Rays (UHECRs), has not been understood yet, because the flux of UHECRs are quite low.

Currently, some experiments continue observing UHECRs. One of them is the Telescope Array (TA) experiment, which is the largest observatory in the northern hemisphere, and other one is the Pierre Auger Observatory (PAO), which is the largest one in the southern hemisphere. These two observatories have published the results of energy spectrum, primary composition and anisotropy studies. The reported anisotropies results are almost consistent, and the energy spectra have a small difference at the cutoff energy region, but it is consistent within systematic uncertainties. In contrast with the spectra, the interpretation on the observed results of the primary composition have large discrepancy between the observatories. TA reported that the primary composition of UHECRs is consistent with the purely proton at $E > 10^{18.2}$ eV, on the other hand, the PAO claimed that the dominant component is gradually changing from protons to heavier nuclei at $E > 10^{18.2}$ eV. This discrepancy is critical to understand the nature of UHECRs. To overcome this problem, we need to check and compare both of the results carefully. Today, they are trying that exchange each detectors and compare the detector biases.

In addition to understanding the discrepancy, we should attempt other approaches to understand the nature of UHECRs, such as using neutral particles. It is expected that there are neutral particles, such as photons and neutrinos, in UHECRs. Charged particle are deflected by the magnetic field in the universe in their propagation. In contrast, neutral particles are not deflected by the magnetic filed

Observation of neutral particles is one of the approaches for understanding the nature of UHECRs. Fluxes of these particles can depend on the primary composition of the UHECRs because of their generation and propagation mechanism. Furthermore, they arrive at the earth with no deflection by the magnetic fields in the universe. Especially for the UHE photon, the arrival directions can be a direct key to search for UHECR sources. Arrival directions of these photons directory point to their sources, and source candidates of these photons are limited to nearby sources, because the mean free path of such high energy photon is constrained by the interaction with the cosmic microwave background radiation (CMBR). In addition to that, if UHE photons are generated with transient phenomena, such as GRB, simultaneous detection with multi-wavelength experiments is expected. That can be a evidence of discovery of UHECR sources. Thus, UHE photons can be a "smoking-gun" of UHECR sources.

In this thesis, Chapter 2 gives a overview of cosmic rays, UHECRs physics and review the recent results. In Chapter 4, the TA detectors are reviewed. Monte Carlo simulation and the reconstruction procedures are given in Chapter 5. Chapter 6, 7 and 8 give analyses results, discussion and conclusion.

Chapter 2

Cosmic rays

After the discovery of cosmic rays, they have been measured and studied over a long period of time. Today, a great deal is known about cosmic ray physics. These knowledges obtained from many studies are reviewed in this chapter.

This chapter consists of two sections. First, in Section 2.1, overview of cosmic ray physics in the broad energy range is presented. Second, in Section 2.2, I will review the physics related to UHECRs, which is important topics in the field of cosmic ray physics and is the main topic of this thesis.

2.1 Overview of cosmic ray physics

There are three major approaches to cosmic ray studies, such as measurement of energy spectrum, chemical composition and anisotropy in cosmic ray arrival directions. In this section, I describe an overview of these three topics, and additionally, I introduce cosmic ray acceleration models and theoretical discussion about origins of cosmic rays.

2.1.1 Energy spectrum

A cosmic ray energy spectrum for a wide energy range is shown in Figure 2.1. The energy spectrum with energies below about 10^{10} eV is flatten than that of higher energy range due to the shielding effect with the magnetic field of the heliosphere. In contrast to that, above this energy range, the spectrum follows a power low with an index of approximately -3, but there are fine structures called "knee", "2^{nd} knee", "ankle" and "cutoff".

The knee is at around energy of $10^{15.5}$ eV. Below this energy, the power low index is -2.7, and above the energy it is -3. One of possible explanations for this change of the spectral index is that this is caused by the change of dominant origins or acceleration mechanisms. KASCADE and other experiments reported that the dominant chemical composition changes from light to heavy component with increasing energy around the knee region [3]. In common electromagnetic acceleration mechanisms, the maximum accelerated energy depends on the charge of particle. Therefore, the experimental result

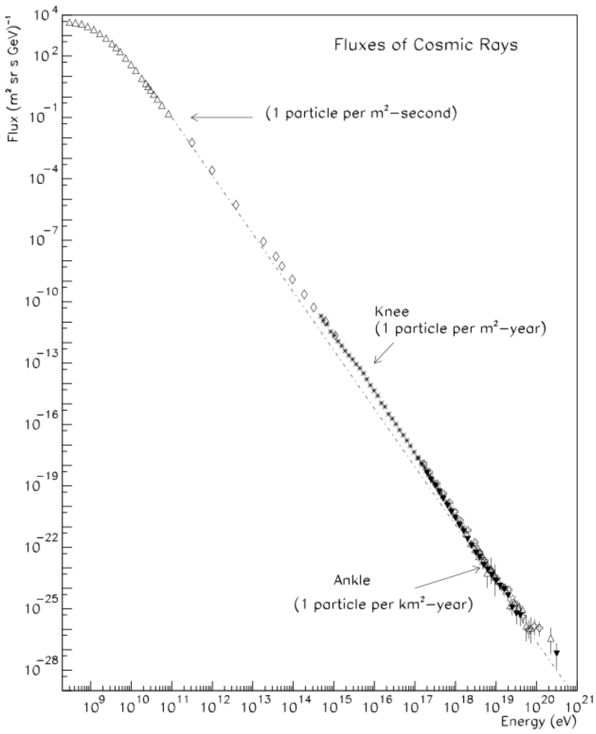

Figure 2.1: The all particle cosmic ray energy spectrum in the broad energy range [1].

supports the model in which a dominant mechanism reaches its acceleration limit with increasing energy at the knee. On the other hand, there is another explanation for the knee, which is caused with the energy and charge dependent leakage of cosmic rays from the confinement volume of our galaxy. The length scale of the motion of the relativistic charged particle with energy of E and with charge of $q = Ze$ (e : the elementary charge) moving in the magnetic field B is equivalent to an order of the its Larmor radius [2],

$$r_L = \frac{E}{qcB} = (1.08\ [\mathrm{pc}])\, \frac{E\ [\mathrm{PeV}]}{Z\,(B\ [\mu\mathrm{G}])}. \tag{2.1.1}$$

Then, for a particle with energy of 10^{15} eV in the galactic magnetic field assumed to be 3 μG, the Larmor radius is 0.36 pc. This is enough smaller than the thickness of the galactic disk (about 100 pc), but above this energy the Larmor radius becomes more larger. Therefore confinement of cosmic rays in the galaxy becomes less effective with increasing energy, and the spectrum appears to be steep.

This is also a natural explanation of the 2^{nd} knee which is small steepening of the spectral shape at energy around $10^{17.5}$ eV. The maximum energy of the acceleration is depend on an atomic number Z. Thus the acceleration limit of nuclei with charge of Ze is expected to be

$$E_{\mathrm{max,Z}} = ZE_{\mathrm{max,p}}, \tag{2.1.2}$$

where $E_{\mathrm{max,p}}$ is the acceleration limit of protons. Therefore, it can be understood that 2^{nd} knee is caused by the acceleration limit of heavy nuclei. However, the chemical composition at the 2^{nd} knee region is poorly probed, and at this time this model is not confirmed. Near future, the low energy extensions of PAO, which are called HEAT and AMIGA, and the low energy extension of TA, which is called TALE, will provide clues to the solution of the problem.

The ankle is at around $10^{18.5}$ eV, which is hardening of the energy spectrum. The index changes to -2.7 above this energy. There are also some models to explain this feature. One of the models predicts that the ankle is caused by the transition from galactic to extragalactic origins of cosmic rays with increasing energy. In the model, we expect a transition from heavy to light compositions at the ankle with increasing energy. Another model is that the ankle is caused by the flux decreasing of extragalactic protons with the energy loss through electron-positron pair production with cosmic microwave background radiation (CMBR) photons, i.e., $\mathrm{p} + \gamma \to \mathrm{p} + \mathrm{e}^+ + \mathrm{e}^-$. This model predicts that the dominant composition is proton in lower and higher energy ranges than the ankle.

If the dominant composition remains proton up to 10^{20} eV, a cutoff is expected at $10^{19.6}$ eV, and it is produced through photo-pion productions with CMBR photons,

$$\mathrm{p} + \gamma \to \Delta^+_{1232} \to \begin{cases} \pi^0 + \mathrm{p}, \\ \pi^+ + \mathrm{n}. \end{cases} \tag{2.1.3}$$

This mechanism had been proposed by Greisen, Zatpin and Kuz'min in 1966 for the first time, and then so called "GZK effect" [4] [5]. The cutoff has been observed by both the TA [6] and PAO [7] experiments. In spite of the fact these two experiments propose different scenarios to explain the cutoff. TA has mentioned that GZK effect is favored to explain the cutoff, with their result of the proton dominant chemical composition. On the other hand, PAO has claimed that the cutoff is caused by an acceleration limit for heavy nuclei from extragalactic origins. This conflict has not been resolved yet. The details of the results of these two experiments are reviewed in Section 2.2.5.

2.1.2 Chemical composition

As discussed in previous section, the chemical composition is a key quantity to examine theoretical theoretical acceleration and propagation models for all the energy ranges. Below 10^{14} eV, the flux of primary cosmic rays is so sufficiently large that we expect to obtain sufficient statistics of events from direct observations of primaries with balloon- or satellite-borne detectors. Thus the chemical abundance can be measured from direct observations of primary cosmic rays. Figure 2.2 shows the chemical abundance of cosmic rays and that of solar system [8]. The cosmic ray composition shows the overabundances at some elements, such as Li–B and Sc–Mn. This is believed to be caused by the spallation process of cosmic ray nuclei with the interstellar matter on the way of travel to Earth.

On the other hand, the flux of cosmic rays above 10^{14} eV is very small, hence we cannot expect to obtain enough statistics with direct measurements. Therefore, such high energy cosmic rays are observed by measuring secondary cosmic rays. *i.e.* an Extensive Air Shower (EAS), which is a complex of electromagnetic and hadronic cascades (detailed in section 2.2.3). Instead of the direct measurements of the mass and the charge of primaries, we use some observable quantities of EAS in order to determine the particle type of primaries. One of such quantities is the depth of the maximum development of EAS, which is called X_{max}. This quantity reflects the atomic mass number of primary particles. The derivation of the dependence of X_{max} on atomic mass numbers for UHECRs is particularly discussed in Section 2.2.3.

2.1.3 Anisotropy

The anisotropy of cosmic ray arrival directions is studied by various methods in order to directly identify sources of cosmic rays or in order to reveal the distribution of sources. One of the simple way to examine the anisotropy is the auto-correlation analysis, which is searching for event concentrations on an arrival direction map. Another approach such as investigation of correlations between the arrival direction of cosmic rays and the position of known astronomical objects is one of the methods to search for sources. The other approach is a comparison between the arrival direction distribution of observed events and simulated one, based on the assumption of some source distributions, matter and photon distributions, and interactions with matter, photons and the magnetic field during their propagations.

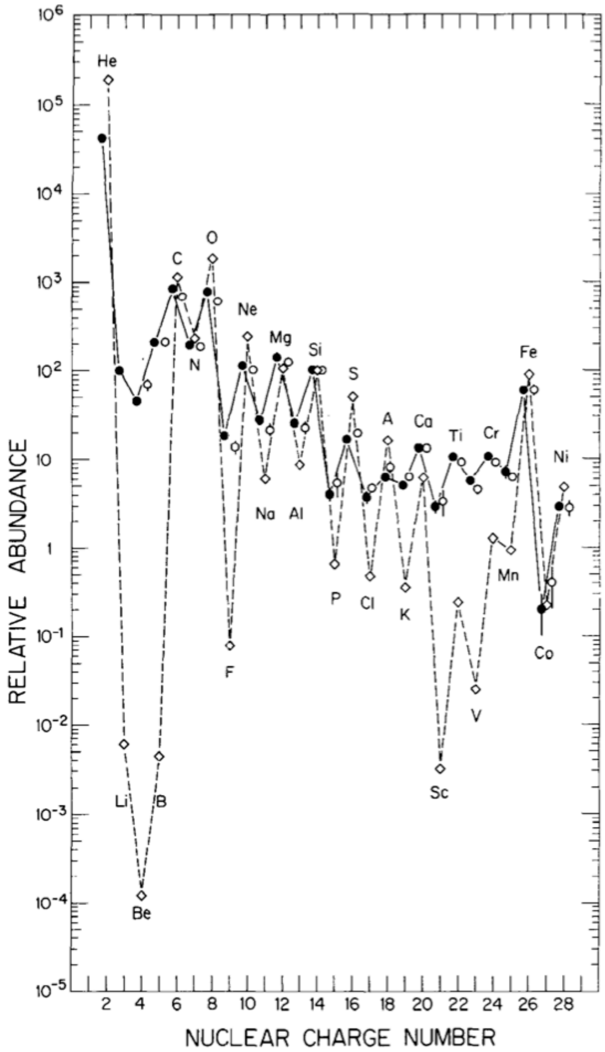

Figure 2.2: The chemical abundance of cosmic rays measured at the Earth compared with the solar system abundances [8]. Vertical axis is the relative abundance based on that silicon equal 100. Filled circle shows the chemical abundance of cosmic rays measured in low energy region (70–280 MeV/nucleon), and open circle shows the chemical abundance of cosmic rays in high energy region (1000–2000 MeV/nucleon). Diamond shows the chemical abundance of the solar system.

Unfortunately, most of the cosmic rays have a non-zero charge, and there is the magnetic field in the universe. The arrival direction of a cosmic ray is expected to be refracted and deviated from its source position, and the distribution of cosmic ray arrival directions is smeared. Therefore, we need a number of statistics to reveal the anisotropy of cosmic ray arrival directions from smeared distribution. However, the magnetic deflection of UHECRs is smaller than that of lower energy cosmic rays, because it depends on the rigidity of particles. Thus, study of the anisotropy for UHECRs is an effective method to identify their sources.

2.1.4 Acceleration mechanisms

Acceleration mechanisms of cosmic rays are not fully understood, and there are some theoretical predictions. The most basic mechanism is a stochastic acceleration model of charged particles, which was originally proposed by Fermi in 1949 [9], and it is called "Fermi mechanism".

Fermi mechanism

The original picture of the Fermi acceleration is transferring macroscopic kinetic energy of a moving magnetized plasma to charged particles. If such energy transfer is repeated many times, then the particle is stochastically accelerated to nonthermal energies. We consider a process that a charged particle interact with magnetized plasma cloud. The particle is accelerated to proportional to its energy with each interaction. Then, the particle obtain the energy $\Delta E = \xi E$ per an encounter, and after n times interactions the energy of the particle reaches E_n

$$E_n = E_0(1+\xi)^n, \tag{2.1.4}$$

where E_0 is the initial energy when it is injected into the accelerator. The number of interactions needed to reach an energy E is

$$n = \ln\left(\frac{E}{E_0}\right)/\ln(1+\xi). \tag{2.1.5}$$

When the escape probability from the acceleration region is $P_{\rm esc}$ per interaction, the energy spectrum of particles accelerated to energies greater than E is

$$N(\geq E) \propto \sum_{m=n}^{\infty}(1-P_{\rm esc})^m = \frac{(1-P_{\rm esc})^n}{P_{\rm esc}}, \tag{2.1.6}$$

and hence

$$N(\geq E) \propto \frac{1}{P_{\rm esc}}\left(\frac{E}{E_0}\right)^{-\gamma}, \tag{2.1.7}$$

where

$$\gamma \equiv \ln\left(\frac{1}{1-P_{\rm esc}}\right)/\ln(1+\xi) \approx \frac{P_{\rm esc}}{\xi}. \tag{2.1.8}$$

Consequently, Fermi mechanism leads to a power low energy spectrum as the observed cosmic ray energy spectrum.

Acceleration at supernova

Supernova (SN) explosions eject materials to the interstellar medium (ISM), and they drive a shock wave with magnetic field where charged particles can be accelerated. The finite lifetime of the SN shock wave limits the maximum energy per particle that can be achieved with the acceleration at SN. The acceleration rate is

$$\frac{\mathrm{d}E}{\mathrm{d}t} = \frac{\xi E}{T_{\mathrm{cycle}}}, \tag{2.1.9}$$

where ξ is the fractional energy gain per single acceleration cycle, and T_{cycle} is the characteristic time for one cycle. In order to estimate the maximum energy E_{max} by integrating (2.1.9), we need to know T_{cycle}.

Firstly, let us consider the upstream region, which is the outer region of a SN shock sphere (Figure 2.3). The particle flow is given by

$$\mathbf{J} = -D\nabla N + \mathbf{u}N, \tag{2.1.10}$$

where D is a diffusion coefficient and N is the number density of particles. In the upstream region, the fluid velocity $\mathbf{u}_1$ is negative in the rest frame of the shock wave. There is no net flow in equilibrium, thereby

$$D_1 \frac{\mathrm{d}N}{\mathrm{d}z} = -u_1 N, \tag{2.1.11}$$

and so in the upstream region

$$N(z) = \rho_{\mathrm{CR}} \exp\left(-\frac{z u_1}{D_1}\right), \tag{2.1.12}$$

where ρ_{CR} is the number density of cosmic rays at the shock front. The total number of particles per unit area in the upstream region is $\rho_{\mathrm{CR}} D_1/u_1$. The rate per unit area at which relativistic cosmic rays cross a shock plane is $c\rho_{\mathrm{CR}}/4$. Thus, the mean time that a particle is remained in the upstream region is $4D_1/(u_1 c)$. The downstream region is somewhat more complicated to analyse because it is necessary to average the residence time only over those particles that do not escape. The analysis is shown explicitly by Druri [12]. According to that, the form of averaged residence time is identical to that in the upstream region. Therefore,

$$T_{\mathrm{cycle}} = \frac{4}{c}\left(\frac{D_1}{u_1} + \frac{D_2}{u_2}\right). \tag{2.1.13}$$

To proceed the calculation, we need to estimate the diffusion coefficients. Lagage and Cesarsky argued that the diffusion length of charged particles cannot be smaller than its

Larmor radius $r_{\rm L} = E/(ZeB)$ [13], where Z is the charge of the particle, E is the total energy and B is the magnetic field strength. Hence, the minimum diffusion coefficient, which gives the maximum acceleration rate is calculated with r_L as

$$D_{\rm min} = \frac{r_{\rm L} c}{3} \sim \frac{1}{3}\frac{Ec}{ZeB}. \tag{2.1.14}$$

Therefore, when we substitute $D_1 = D_2 = D_{\rm min}$ and $u_2 = u_1/4$ with a strong shock assumption,

$$T_{\rm cycle} \geq 20E/(3u_1 ZeB), \tag{2.1.15}$$

Finally, the maximum energy of charged particles in the SN shock wave acceleration is derived from eq. (2.1.9) and (2.1.15) as

$$E_{\rm max} \leq \frac{3}{20}\frac{u_1}{c} ZeB(u_1 T_{\rm A}), \tag{2.1.16}$$

where $T_{\rm A}$ is lifetime of the SN shock wave. For example, the SN which ejects 10 $M_\odot$ at 5×10^6 m/s during $T_A \sim 1000$ years, into the ISM with the density of 1 cm^{-3} and with the magnetic field the order of μG. In such situation, the maximum energy is derived from eq (2.1.16) as

$$E_{\rm max} \leq Z \times 10^{14} \text{ eV}. \tag{2.1.17}$$

As a result of the rough estimation, SN shock waves can only accelerate cosmic ray protons up to 10^{14} eV.

2.2 Ultra high energy cosmic rays

The cosmic ray energy spectrum continues to above 10^{18} eV and such high energy cosmic rays are called ultra high energy cosmic rays (UHECRs). The flux of UHECRs is extremely small reflecting the stochastic nature of unknown acceleration mechanisms to such ultra high energies. Moreover, UHECRs are affected by the magnetic fields and the cosmic microwave background radiation (CMBR) photons in their propagation to the Earth. In this section, a general overview and recent results of UHECR studies are described.

2.2.1 Propagations

UHECRs interact with CMBR photons and with intergalactic and galactic magnetic fields in their propagations. The interaction with CMBR photons causes important processes, which are photo-pion production, electron positron pair-production and photo-disintegration. These processes are important to understand origins of UHECRs.

Photo-pion production and electron-positron pair production

Greisen, Zatsepin and Kuzmin pointed out that the universe is opaque for cosmic rays which have sufficiently high energies. This is called GZK effect. When cosmic ray protons have energies around 10^{20} eV, the energy of CMBR photons approximately corresponds to the pion rest mass in the rest frame of protons. In this case, the interaction of an UHE proton with a CMBR photon creates pions, and as a result the proton loses its energy. The most important process which contributes the total cross-section of the photo-pion production is the $\Delta^+(1232)$ resonance production, such as

$$\mathrm{p} + \gamma \rightarrow \Delta^+_{1232} \rightarrow \begin{cases} \pi^0 + \mathrm{p} \\ \pi^+ + \mathrm{n} \end{cases} . \tag{2.2.18}$$

The energy threshold of photons for this interaction in the rest farme of the proton is approximately equivalent to the rest mass of π. It correspond to the primary proton energy of 6.79×10^{19} eV for 2.7 K photons.

UHECR protons also lose their energies by the electron-positron pair production,

$$\mathrm{p} + \gamma \rightarrow \mathrm{p} + \mathrm{e}^+ + \mathrm{e}^-. \tag{2.2.19}$$

Figure 2.4 shows the attenuation length of UHECRs in the CMBR photon field. The attenuation length for UHECRs energies above 10^{20} eV is less than 100 Mpc, therefore, these extremely high energy cosmic rays can only reach us from relatively nearby sources.

Photo-disintegration

UHE nuclei also interact with CMBR photons, and they are broken in fragments, *i.e.*, into lighter nuclei. This process is called photo-disintegration. This is an important energy loss mechanism for UHECR nuclei. UHECR nuclei are strongly affected by this process in the energy range from 10 MeV to 30 MeV in the rest frame of UHECR nuclei.

The attenuation lengths for four species are shown in Figure 2.5 [18]. For the nuclei, this process is dominant energy loss mechanism in the energy range above $10^{18.0}$ eV. In addition, this mechanism also predicts the cutoff at approximately same energy as the GZK cutoff. Thus, the mass composition of cosmic rays and the dominant energy loss mechanism are important to discuss the propagation of UHECRs.

Propagation in the magnetic fields

Most of cosmic rays are charged particles, therefore they are affected and deflected by magnetic fields in the universe. The Larmor radius of cosmic ray protons with energy of 10^{19} eV is about 3 kpc in the 3 μG interstellar magnetic field. This radius is larger than the thickness of the galactic disk, thus cosmic rays which have energies above 10^{19} eV cannot be confined in our galaxy. Therefore, the hypothesis that origins of UHECRs are

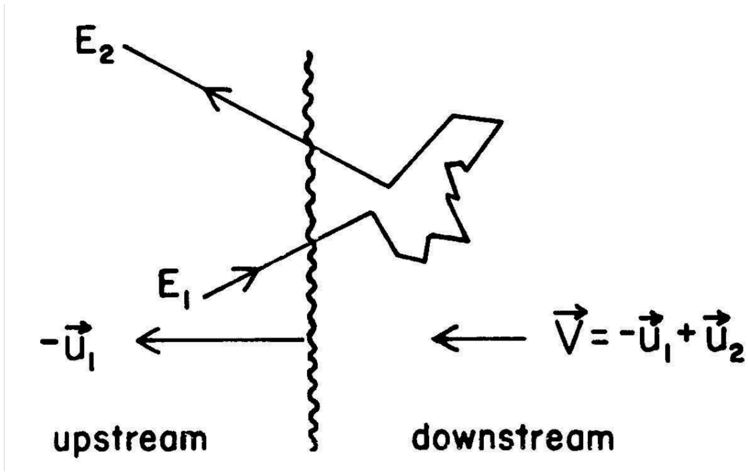

Figure 2.3: Acceleration at supernova shock front [11].

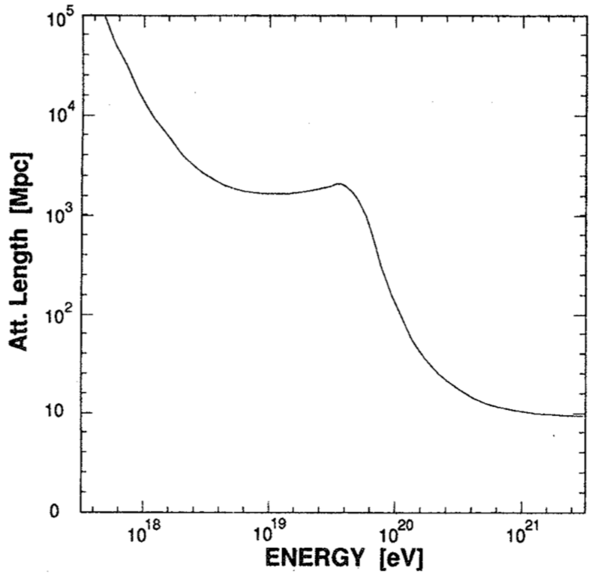

Figure 2.4: The attenuation length of UHECR protons in the CMBR photon field [15]. This calculation including the photo-pion production and electron-positron pair production. First dip around 10^{19} eV is caused by the pair production, and the second dip is created by the photo-pion production.

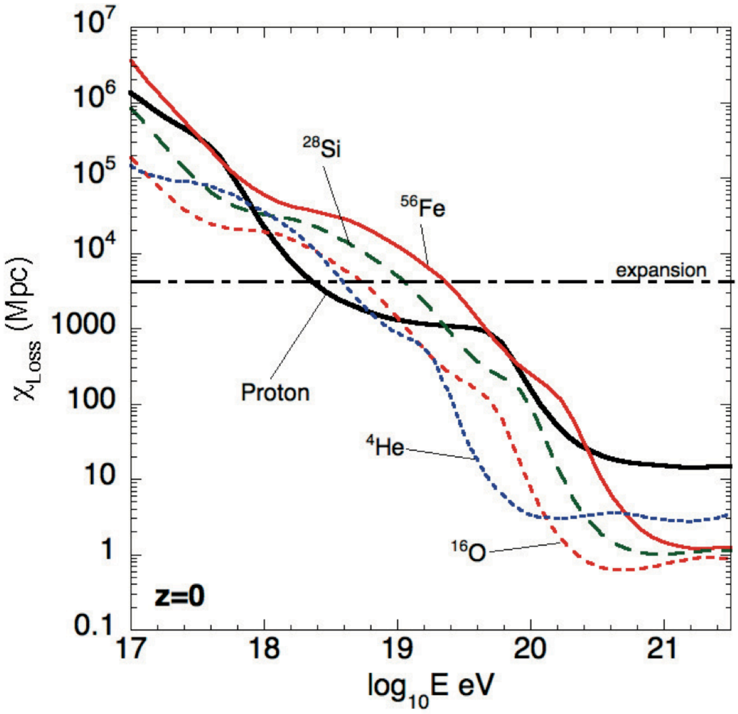

Figure 2.5: Energy loss lengths for different nuclei [18].

extragalactic is favored. The strength of the extragalactic magnetic field is measured by the Faraday rotation techniques, but there are large uncertainties the measurements, and the order of magnitude is believe to be 1 nG. Figure 2.6 shows simulated trajectories of UHE protons in the 1 nG magnetic field. Trajectories of 10^{20} eV is almost straight, and they can be traced back to origins of cosmic rays.

2.2.2 Origins of UHECRs

Origins of UHECRs have not been resolved yet, and there are many theoretical models for UHECR origins. They are divided two types of models. One is the "Bottom-up" models, and the other is the "Top-down" models.

Bottom-up scenarios

The bottom-up models predict that UHECRs are generated through the accelerations of low energy cosmic rays. In this model, the acceleration of lower energy particles is believe to be basically performed with the Fermi mechanism by shock waves, thus cadidates of UHECR origins are limited to a certain type of astronomical objects. For UHECR origins, their magnetic field strength and the size of the objects are required to be large enough to accelerate particles up to 10^{20} eV. The relation between the maximum energy $E_{\max}$ of an accelerated particle and parameters of an acceleration site is given by

$$E_{\max} \propto ZeBL\beta, \tag{2.2.20}$$

where Ze is the charge of the particle, B is the strength of the magnetic field at the acceleration site, L is the size of the acceleration site, and βc is the velocity of the shock wave at the site. Figure 2.7 shows the relationship between the magnetic field strength and the typical size of the acceleration region of astronomical objects. This figure shows candidates of UHECR origins which can accelerate cosmic rays up to 10^{20} eV. If the size of the acceleration site is small, then the magnetic field strength has to be large enough to accelerate particles to ultra high energies, because the Larmor radius must be smaller than the acceleration region size in order to efficiently confine UHE particles in the region. Furthermore, these candidates have to be found within the distance of 100 Mpc because UHE particles lose their energies by the GZK effect or the photo-disintegration process.

Top-down scenarios

In contrast with the bottom-up models, top-down scenarios predict that UHECRs are generated through the decay or the interaction of energetic particles, for example, the interaction of the topological defects [22, 23], the decay or annihilation of super heavy dark matters [25], Z-burst model, which is caused by the resonant production of Z boson by the interaction between relic neutrinos and UHE cosmic neutrinos [24]. Most of the top-down scenarios predict relatively large abundance of the UHE photons and UHE neutrinos.

Therefore, it can be proved when we measure significant fraction of photons in UHECRs and a large flux of UHE neutrinos.

In addition, there are other possibilities to verify these models. One of the ways is that probing the anisotropy of cosmic ray arrival directions. If UHECRs are produced by some sort of dark matter, we expect an excess of the UHECR flux from the galactic center region.

2.2.3 Extensive air showers

When primary cosmic rays with sufficient energy enter the atmosphere, they interact with molecules of the atmosphere and produce fluxes of secondary particles. All these particles together create cascades known as extensive air showers (EASs). This phenomena is discussed in detail here. Since the flux of UHECRs is quite small, it is difficult to obtain sufficient statistics of events by direct observations with ballon- or satellite-borne detectors, because it is not realistic to construct such a huge detector which can obtain sufficient statistics of UHECR events at the top of the atmosphere. Therefore, the indirect measurement for EAS is the main method for observations of UHECRs.

In the early stage of the EAS development, the number of secondary particles increases exponentially. The number of secondary particles in this cascade finally reaches its maximum, and then the number of secondary particles decreases. The EAS cascade consists of three major components; the electromagnetic cascade, the hadronic component and the muonic component. Figure 2.8 shows a schematic diagram of these basic processes.

For the dominant component of UHECR primaries, the initial interaction between primaries and the atmosphere is the hadronic interaction, and mostly produces mesons, where the most abundant secondary is pion. Pions with three different charge, *i.e.*, π^+, π^0, and π^-, are produced equal probability. The charged pion, which has relatively long life time, continues producing more hadronic collisions, or it decays into muon and neutrino, as $\pi^\pm \rightarrow \mu^\pm + \nu$. The neutral pion which has relatively short life time decays into two photons, as $\pi^0 \rightarrow 2\gamma$, and they originate electromagnetic cascades.

Electromagnetic cascade

Electromagnetic cascades are induced by interactions of high energy photons, electrons, and positrons with atmospheric molecules. One high energy photon generates a pair of electron and positron with the pair production, $\gamma + \mathrm{N} \rightarrow \mathrm{e}^+ + \mathrm{e}^- + \mathrm{N}$, where N is a nucleus. And a high energy electron and positron emits photons via bremsstrahlung, $\mathrm{e}^\pm + \mathrm{N} \rightarrow \mathrm{e}^\pm + \mathrm{N} + \gamma$. As a result, the number of particles increases as long as energy of particles are sufficiently for continuing the cascading process. Figure 2.9 gives the idea which is proposed by Heitler [26] how the bremsstrahlung and the pair production processes work in the electromagnetic cascade. It should be noted that the radiation length for bremsstrahlung of electrons and positrons is $36.5\mathrm{g/cm}^2$ in the air, and it is approximately equal to the attenuation length of high energy photons with the pair production. As the air shower which particles have sufficiently high energy travels one radiation length, the number of particles is doubled through these two processes, and the average energy per particle is halved.

The critical energy is determined from the balance of the two energy loss processes of electrons and positrons, *i.e.*, bremsstrahlung, which drives the growth of the number of particles, and ionization. The probabilities of these two processes become equivalent at energy of 84 MeV in the air, and that is called the critical energy E_c. Along with the growth of the number of secondary particles by cascading processes as the shower development, the primary energy is divided up into the secondary particles, and finally the averaged energy per secondary particle reaches the critical energy. At this point, the number of the secondary particles in the cascade reaches a maximum, called N_{max}, and the slant depth of the point along with the shower axis is called the depth of shower maximum, X_{max}. As mentioned in Section 2.1.2, X_{max} is one of the most important quantities sensitive to the atomic mass number of primary cosmic rays. In addition, N_{max} is a quantity which sensitive to the energy of primary cosmic rays because it linearly depends on the energies of the primaries. After the shower maximum, the number of secondary particles decreases along with the shower development.

Hadronic component

The energy of the hadronic component in EAS is constantly converted into the electromagnetic cascade via the decay of π^0 which are produced in the hadronic interactions. $\pi^{\pm}$ and π^0 are produced with an equal probability of $\pi^{\pm}$ and π^0 in each hadronic collision. Because of this energy transfer process, the electromagnetic portion for the number of secondary particles becomes dominant after only a few generations of collisions. The hadronic component constitute about 1% of the total number of secondary particles in one EAS.

Muonic component

Most of low energy charged pions from hadronic collisions at the later stage of the air shower development decay into muons and neutrinos ($\pi^{\pm} \to \mu^{\pm} + \nu$). The mean lifetime of the charged pions is relatively long (2.6×10^{-8} s) because the decay is via the weak interaction. Most of the muonic component in the shower is generated through these decays. Higher energy muons are generated in the upper atmosphere, where the atmospheric density is sufficiently low such that the charged pions have more of a chance to decay before colliding, and lower energy muons are generated in the lower atmosphere. Secondary muons and neutrinos undergo hard collisions only very rarely in the atmosphere. Thus, most of the muons in EASs deeply penetrate the atmosphere, and muons which are not collide with the atmospheric molecules can arrive at the ground.

Longitudinal development

As mentioned above, secondary particles in EAS are dominated by the electromagnetic component. In this section, let us consider a very simple toy model of the longitudinal development of a purely electromagnetic cascade caused by a photon with very high energy of E_0. In this model, a sufficiently high energy photon produces an electron-positron pair having the half of the photon energy after the photon has traveled a distance of λ, which is the radiation length for the pair production process in the air. Moreover, a sufficiently high energy electrons or positrons emit one photon by bremsstrahlung with giving a half of their kinetic energy on average to the photon after traveling a distance of λ. With these two processes, the primary photon creates an electron and a positron in the first step, and in the second step, the number of particles increases to four, *i.e.*, two photons, an electron and a positron. Each particle has the energy of $E_0/4$. It can be denoted that after i steps the number of particles is $N_i = 2^i$, and each particle has the energy of $E_i = E_0/2^i$. Using the grammage distance, x, instead of i, N and E are written in the form

$$N(x) = 2^{x/\lambda}, \tag{2.2.21}$$

and,

$$E(x) = \frac{E_0}{2^{x/\lambda}}. \tag{2.2.22}$$

This process continues until the average energy per particle reaches the critical energy, E_c. At the $X_{\max}$, the number of particles reaches the maximum and $N(X_{\max})$ can be written as

$$N(X_{\max}) = N_{\max} = E_0/E_c. \tag{2.2.23}$$

Using the relation (2.2.21) we obtain $X_{\max}$ as,

$$X_{\max} = \lambda \frac{\ln(E_0/E_c)}{\ln 2}. \tag{2.2.24}$$

Therefore, $X_{\max}$ has the logarithmic dependence on E_0, and $\mathrm{d}X_{\max}/\mathrm{d}(\ln E_0)$ is called called the elongation rate.

We discussed about the longitudinal development of air showers induced by primary photons. Now, let us revisit the longitudinal development for primary protons and heavy nuclei. Primary protons initially create the hadronic component of showers, and most of their energies are transported to the electromagnetic component. For primary nuclei, it can be seen as a superposition of low energy nucleons, each of which has the average energy of E_0/A, where E_0 is the energy and A is the mass number of the primary nucleus. Thus, the air shower induced by the nucleus of A is considered to consist of A subshowers with the primary energy of E_0/A. Therefore, in the toy model of the longitudinal development described above the primary energy is E_0/A, except E_0, for the nucleus A. Then, the mass number dependence for $X_{\max}$ is expressed as,

$$X_{\max} \propto \ln \frac{E_0}{A}. \tag{2.2.25}$$

Thus, $X_{\max}$ can be used for determining the composition of primary cosmic rays.

In addition, the shape of the distribution of $X_{\max}$ also depends on the composition of primary cosmic rays. As described above, the EAS induced by nuclei of A is considered to consist of A subshowers. The bunch of these subshowers results in an averaging effect on the single EAS. Therefore, EASs which is induced by heavy nuclei have smaller fluctuations than the EASs induced by protons.

Though Heitler model gives the $X_{\max}$ dependency for the chemical composition of primary cosmic rays, there is another treatment of longitudinal development. The Gaisser-Hillas function is generally used for fitting the development of charged particles in EAS [11, 27],

$$N(x) = N_{\max} \left(\frac{x - X_0}{X_{\max} - X_0} \right)^{(X_{\max}-X_0)/\lambda} \exp\left(\frac{X_{\max} - x}{\lambda} \right), \tag{2.2.26}$$

where, X_0 is the first interaction point of primary particles, and λ is the attenuation length, typically $\lambda = 70$ g/cm^2. The variable x used above is the grammage distance that an EAS has traveled through the atmosphere. That is called *slant depth* which unit is [g/cm^2].

Lateral distribution

Particles in an EAS have a lateral spread. Lateral distributions of electromagnetic cascades are parametrized by Nishimura, Kamata and Greisen called NKG function [28],

$$\rho(r, s) = \frac{N_{\mathrm{e}} f(r, s)}{r_{\mathrm{M}}^2}, \tag{2.2.27}$$

$$f(r, s) = C(s) \left(\frac{r}{r_{\mathrm{M}}} \right)^{s-2} \left(\frac{r}{r_{\mathrm{M}}} + 1 \right)^{s-4.5}, \tag{2.2.28}$$

where r is the distance from the shower axis of EAS, r_{M} is the Moliére unit, s is the shower age, $C(s)$ is a normalization factor, and N_{e} is the number of particles at any point in the shower.

In order to represent lateral distributions for hadron-induced EASs, the TA experiment uses the empirical function established by the AGASA experiment [29]:

$$\rho = A \left(\frac{r}{r_{\mathrm{M}}} \right)^{-1.2} \left(1 + \frac{r}{r_{\mathrm{M}}} \right)^{-(\eta(\theta)-1.2)} \left[1 + \left(\frac{r}{1000\ \mathrm{m}} \right)^2 \right]^{-0.6}, \tag{2.2.29}$$

$$\eta(\theta) = 3.97 - 1.79 \left[\sec(\theta) - 1 \right], \tag{2.2.30}$$

where A is a normalization factor, and θ is the zenith angle of the shower axis. This empirical equation includes the zenith angle dependency.

2.2.4 Detection techniques

As mentioned above, in order to study the nature of UHECRs we detect the EAS particles initiated by incident primaries instead of direct observations of the primaries. In this section, the techniques for detecting EASs are briefly reviewed.

Particle detection techniques on the ground

The most commonly-used method for the EAS detections is based on the coincident detections of the remnants of EAS particles with a particle detector array at the ground level. In general, this type of detectors are called surface detector (SD) arrays. Each SD records the number of particles and the arrival timings at the ground level. Then, the number of particle distribution as a function of the distance from the EAS core and the arrival timing distribution are used to reconstruct the energy and the arrival direction of EASs. Since the typical size of lateral spread of EAS particles at the ground level is about a few kilometers in ultra high energies, SDs should be deployed with about one kilometer spacing.

Energies of primary particles are estimated from the comparison between the measured and the simulated particle distributions. In the simulation we need to assume the chemical composition of primaries. However, the composition is not known exactly in the indirect measurement energy range. Moreover, hadronic interaction models used in the simulations are extrapolations of experimentally proved results with accelerator experiments, because the interaction energies at current particle colliders are significantly lower than that of air–UHECR interactions. Thus, the primary energy estimation with the SD array detections has systematic uncertainty by these ambiguity and extrapolations. However, SD arrays are generally stable observational equipments and are able to achieve large exposure.

Fluorescence detection techniques

In the fluorescence method, we uses the nitrogen fluorescence emission to measure the longitudinal development of EASs as they move through the atmosphere. In other words, the atmosphere plays a role as a huge scintillator. Since the number of secondary particles in a EAS induced by UHECRs is very large, fluorescence photons can be detected by ordinary photodetectors, such as using PMTs and mirrors. This is one of the detection techniques for UHECRs measurement used as fluorescence detectors (FDs) by TA, PAO and other experiments.

Charged particles with sufficient energy excite atmospheric molecules, such as nitrogens or oxygens, and these excited molecules emit fluorescence photons, in ultra-violet and optical wavelength band, mainly from 300 nm to 400 nm by nitrogens. Fluorescence emissions are isotropic, and so the emitted photons can be measured from the side of the EAS axis, and, in particular, showers can be detected from a long distance when the shower size is sufficiently large. There is no need for EASs to point toward the detector or even to strike it directly as it is required for SD arrays.

Fluorescence yield is the measurement, which provides the number of fluorescence photons per energy deposit in the atmosphere. The fluorescence yield depends mostly on energy deposit, but has a weak dependence on air pressure, temperature and humidity. The fluorescence yield spectrum was measured by multiple experiments. In this thesis, the FLASH spectrum [31] and the Kakimoto absolute fluorescence yield [30] are used for simulations and reconstructions of EAS profiles. The measured yield spectrum is shown in Figure 2.10.

2.2.5 Review of the recent results

UHECRs have been observed by various observatories, firstly it was reported in 1963 [32]. After this report various experiments, such as Haverah Park [33], Yakutsk [34], Fly's Eye [35], AGASA [36], HiRes [37, 38], TA, and PAO have also observed UHECRs until now. Recently, progress of UHECR studies is remarkable, however, the nature of UHECR origins is not revealed yet. In this subsection, a brief review of these recent progress focused on TA and PAO results related to three topics, the energy spectrum, primary mass composition, and anisotropies, are described.

Energy spectrum

Figure 2.11 shows the energy spectra measured by several experiments. Although the absolute values of the energy spectra are different within the systematic uncertainties of each experiment, these spectra show similar shape without the highest energy edge of the AGASA spectrum.

According to the recent results of TA and PAO it is established that the existence of a dip and a cutoff in the energy spectrum around the energy of $10^{18.7}$, $10^{19.5}$ eV, respectively. The energy spectra of these two experiments are consistent within their systematic uncertainties, however, there is a systematic difference in energy scales between these two experiments. In order to reveal the nature of UHECRs accurate determination of absolute energies at the spectral bending points is necessary. Therefore, TA and PAO have started the collaborative work to understand the difference of their energy scales [39]

Mass composition

In the study of mass composition for UHECRs $X_{\max}$ is used widely, because of the sensitivity in the mass number. Figure 2.12 shows results of mass composition analysis using $X_{\max}$. TA and PAO have different statement about the interpretation of UHECR composition. TA has reported the primary mass composition is dominated by protons above the energy of $10^{18.2}$ eV. In contrast, PAO has mentioned that the dominant composition is changing to heavier component along with increasing energy above the energy of $10^{18.3}$ eV. The discrepancy makes it difficult to understand the nature of UHECRs. There are two possible explanation, one is that the discrepancy arise from errors of one experiment or both experiments, the other possibility is that the discrepancy arise from the difference of UHECR sources which can be observed in the norther or the southern hemisphere. This has not been concluded yet, and now these two experiments are working to resolve this problem.

Anisotropies

In the energy of E $>$ 57 EeV, PAO found correlations of the cosmic ray directions within a 3.1° radius circle centered at nearby AGNs (within 75 Mpc) in the southern sky (Figure 2.13) [42]. The correlation becomes weak thereafter in the updated measurement [43]. For the TA experiment, this type of correlation analysis is searched, and TA does not find significant correlation between UHECR arrival directions observed by the TA SD with energies above 40 EeV and positions of astronomical object listed in six different catalogs [44].

On the other hand, TA recently reported the intermediate scale anisotropy, *hotspot*, by oversampling using 20° radius circles in the norther hemisphere [45]. Figure 2.14 shows the result of the intermediate scale anisotropy. This hotspot can be a key to reveal UHECR origins.

In the anisotropy study, there is also collaborative work between TA and PAO. Then, now we can search the whole sky anisotropies of UHECR arrival directions [46].

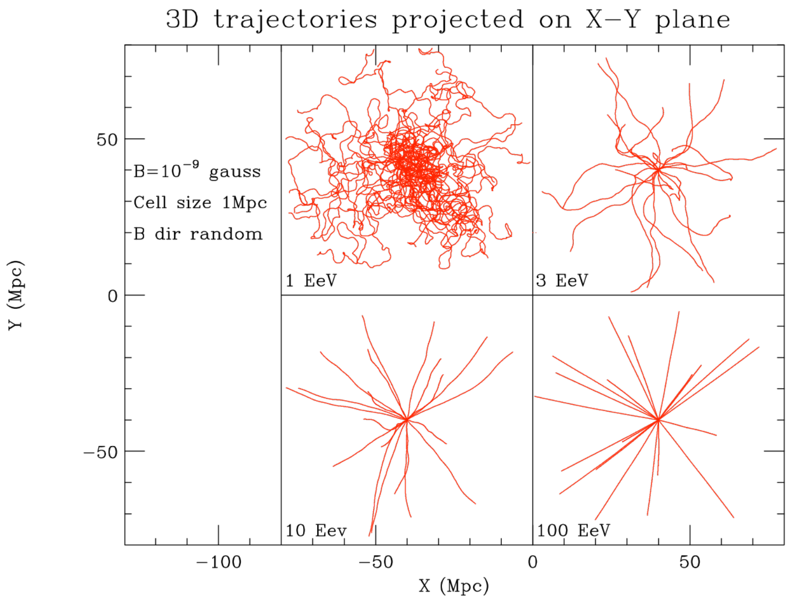

Figure 2.6: Projected view of 20 trajectories of proton primaries injecting from a point source for several energies. The trajectories are plotted until they reach the physical distance from the source of 40Mpc [19].

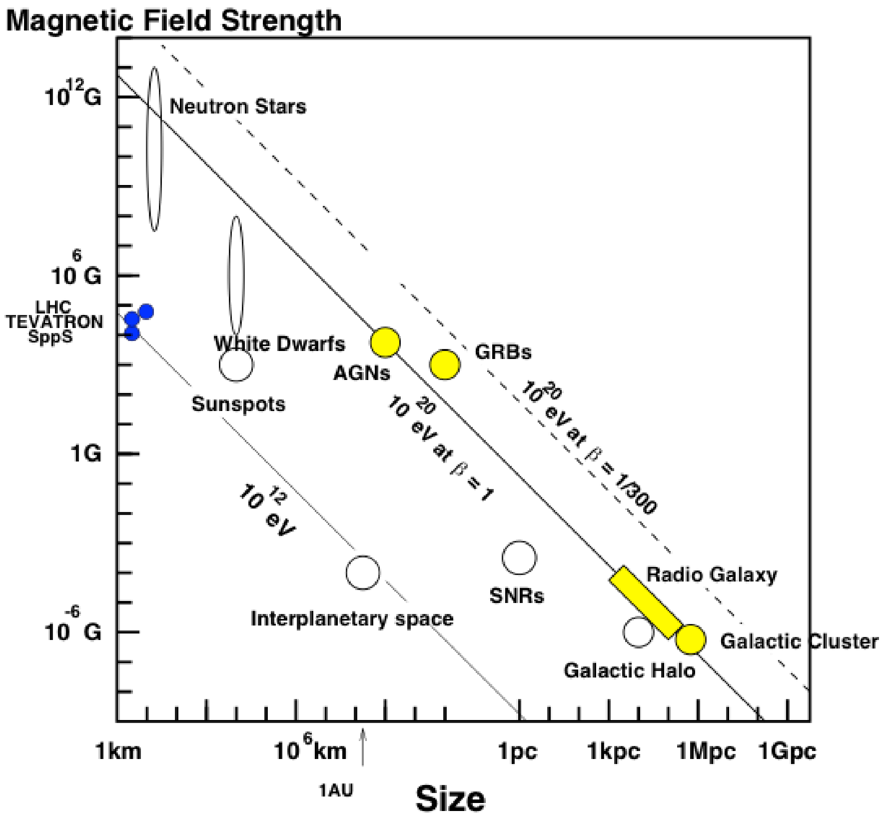

Figure 2.7: The Hillas plot, which shows the relation between the magnetic field strength and the typical size of astronomical objects [21]. Thick line and dashed line indicate the lower limits which can accelerate particles up to 10^{20} eV with each shock condition β (written in the figure), *i.e.*, objects drawn in upper side of the line is feasible as candidates of UHECR origins.

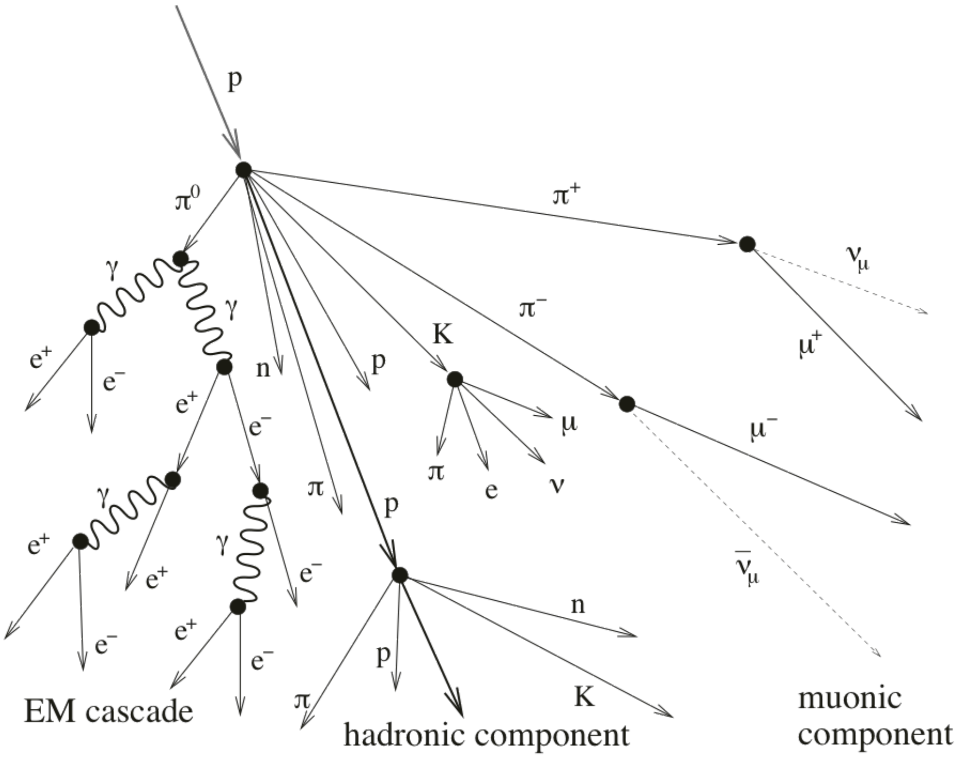

Figure 2.8: An schematic diagram of the basic processes in an EAS. It consists of three major components; the electromagnetic cascade, the hadronic component, and the muonic component

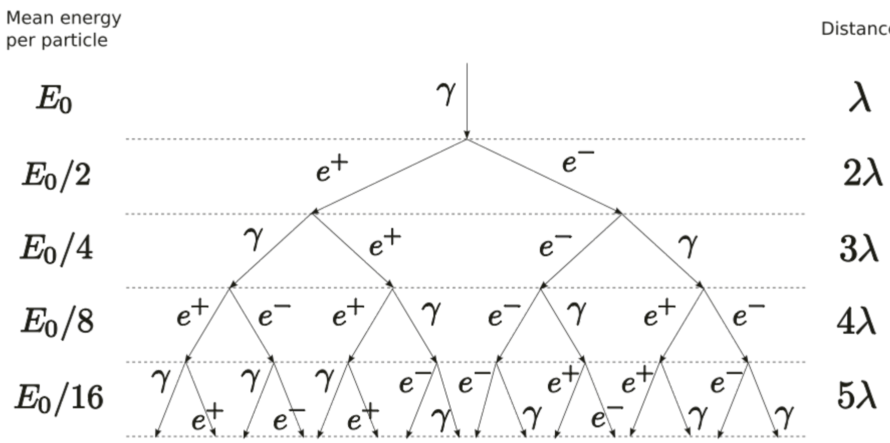

Figure 2.9: The Heitler model for the cascading of the electromagnetic component EAS. Every steps after the propagation of radiation length, λ, the number of particles in the electromagnetic cascade doubles, and the amount of energy per particle decreases in half.

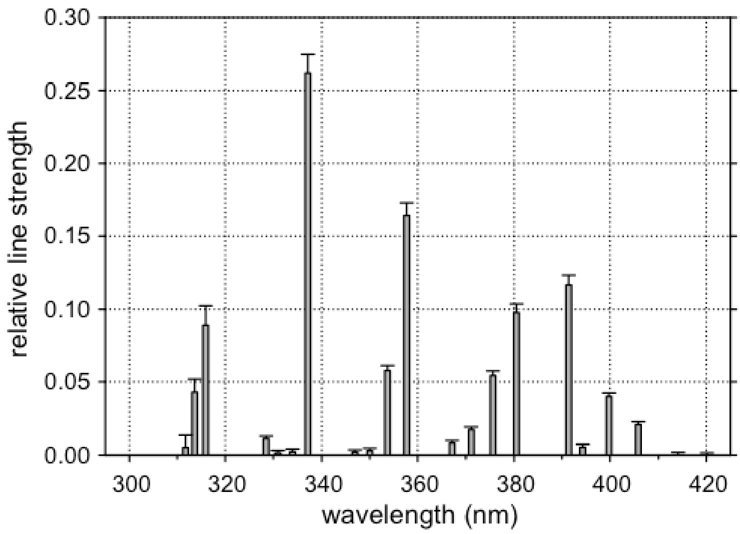

Figure 2.10: The relative fluorescence spectrum measured by the FLASH experiment [31].

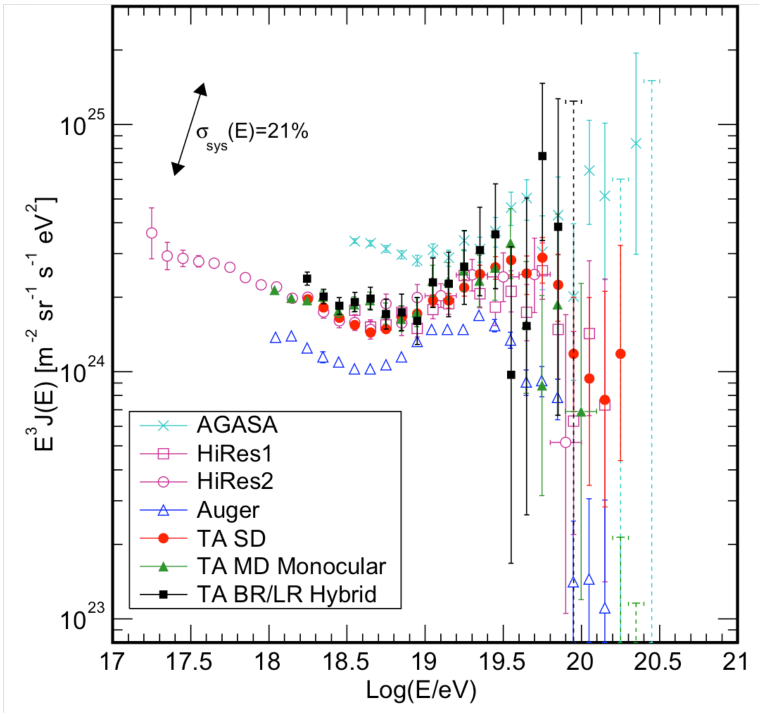

Figure 2.11: The energy spectra obtained by AGASA (blue crosses), HiRes-1/HiRes-2 (open pink squares and pink circles), Auger (open blue triangles), TA SD (filled red circles), TA MD monocular (filled green triangles), and TA BR/LR hybrid (filled black squares) [71]. These spectra multiplied by E^3. The systematic uncertainty of the flux scaled by E^3 due to the uncertainty of the energy of 21% is indicated by arrow

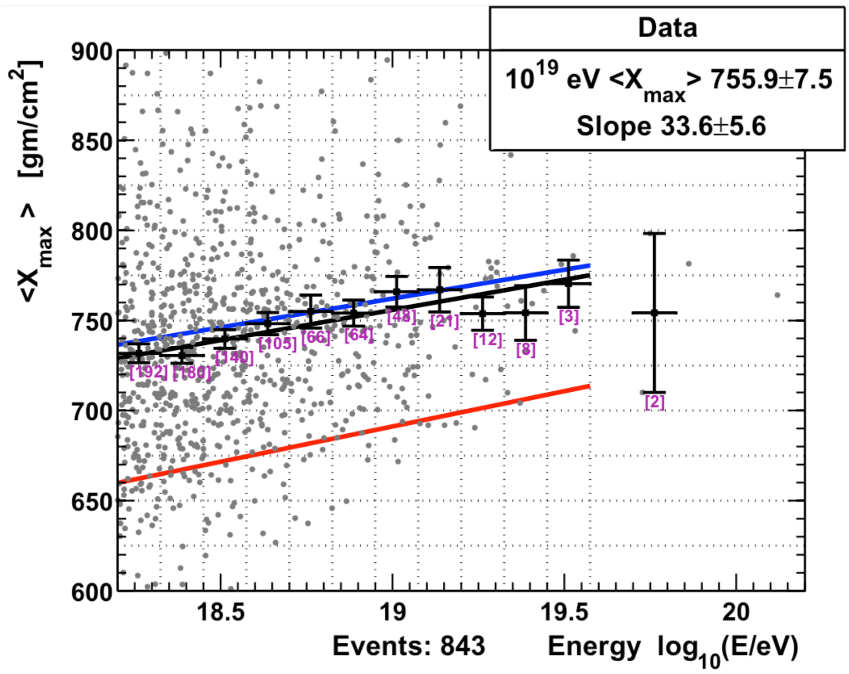

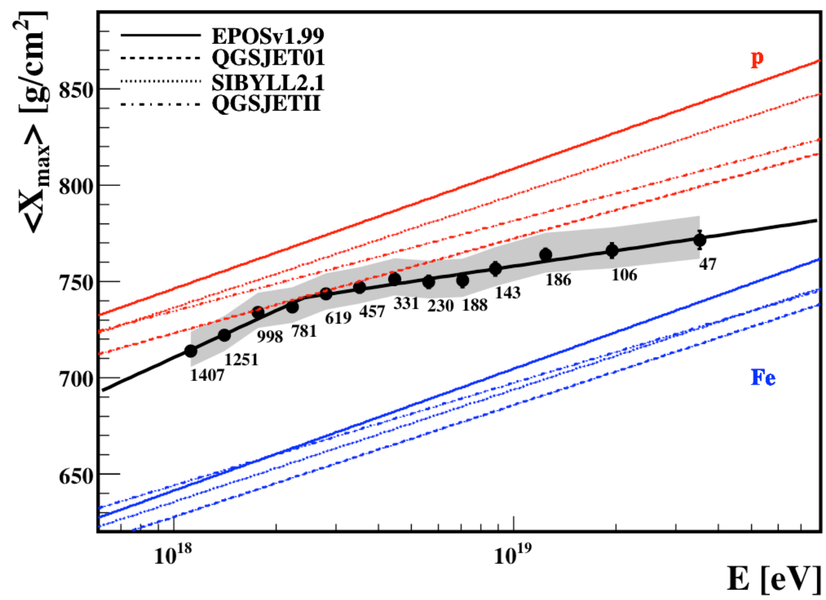

Figure 2.12: Upper figure shows the averaged $X_{\max}$ observed by the TA MD hybrid measurement [40], and lower figure shows that of the PAO hybrid measurement [41].

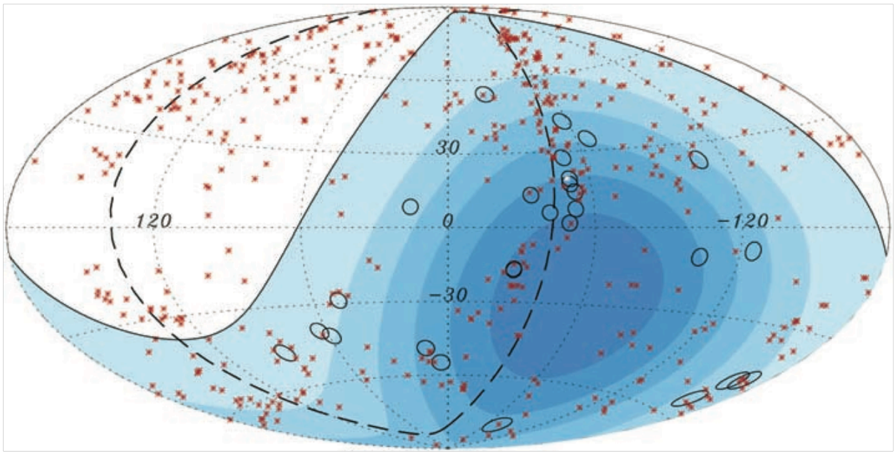

Figure 2.13: The correlation between UHECR arrival directions observed by PAO and the astronomical objects [42], and this figure is in the galactic coordinate. The circles are arrival directions of UHECRs with energies above 57 EeV, and the red points indicate positions of astronomical objects included in the Veron-Cetty and Veron catalogue. Blue contour shows the exposure of the PAO surface detectors, and dashed line shows the super galactic plane.

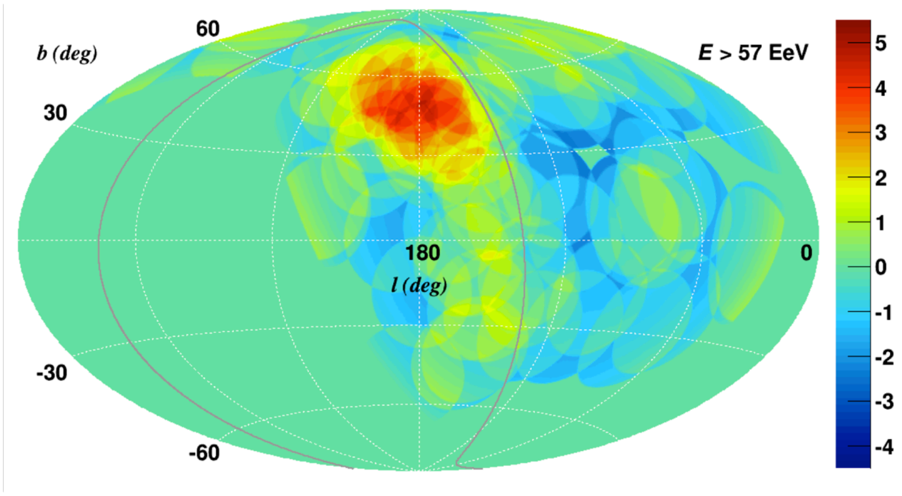

Figure 2.14: The significance of the intermediate scale anisotropy observed by the TA SD [45] in the galactic coordinate. Arrival directions of UHECRs observed by the TA SD with energies above 57 EeV are oversampled within 20° circle, and then the significances of the deviation from isotropic distribution are calculated and plotted. The solid gray line is the super galactic plane.

Chapter 3

Ultra high energy photons

Although many features of UHECRs have been found as discussed above, the origins of UHECRs are still unknown.

Most of UHECRs are believed to be charged particles, so that they are deflected by the magnetic field. In order to discover sources of UHECRs in this situation, quite large statistics of UHECR events are necessary. For neutral particles, however, the situation is different. Neutral particles are not deflected by the magnetic field, and they travel in a straight line from the origin to the Earth. Thus, the arrival directions point to their originated points. In particular for UHE photons, the mean free path suppressed by the interaction with CMBR photons as discussed in the later section. It is much larger than the size of our galaxy, but it is less than the cosmological distance scale. The number of source candidates of UHE photons is not so large because of their short mean free path, and also we can obtain position and timing information of the source candidates from optical and radio observation results. If UHE photons are generated by transient astronomical phenomena, such as GRBs and SNe, simultaneous detection with these observations are possibly expected, and it can be a evidence of their sources. Furthermore, the detailed study of the UHE photon flux is an important key to reveal the origin and the propagation of UHECRs. In particular, top-down scenarios predict higher photon fluxes than that of bottom-up scenarios.

In this chapter, physics connected to UHE photons are reviewed.

3.1 Production mechanisms

There are many models that predict UHE photon production.

In top-down scenarios, photons are produced from decay or annihilation of exotic particles such as topological defects (TD) [22, 23] and super heavy dark matter (SHDM) [25] models, and also the Z-burst model [24] predicts UHE photon generation. The TD, such as cosmic strings, produces extremely heavy particles, and they typically decay into quarks and leptons. The quarks become hadrons and some leptons are decay. As a result of the interactions, a large amount of photons, neutrinos, leptons, and also nucleons are generated. In the SHDM model, SHDM particles, such as named as *cryptons*, *wimpzillas*, and so on, may decay or annihilate, and then UHE photons are created. The Z-burst model is based on the annihilation of neutrinos with Z resonance, which occur between UHE neutrinos and relic background neutrinos. Then, the Z boson decay into protons, neutrinos, and photons. These top-down scenarios predict the relatively higher domination of photon component than bottom-up scenarios in the energy region of UHE. Therefore, the measurement of the UHE photon flux can be a crucial test for these models.

On the other hand, in bottom-up scenarios, UHE photons are mainly produced by the decay of neutral pions which are generated by GZK mechanism in the propagation of UHECRs, called *GZK-photons*. The flux of UHE photons predicted by bottom-up models is not so large as the top-down scenarios, but the amount of the flux depend on the energy spectra and environment, such as strength of the magnetic fields, of their sources. Thus, the GZK-photon flux can be a complementary clue to understand the acceleration mechanism at UHECR sources.

3.2 Propagations

UHE photons lose their energies through the interaction with background photons as is the case with UHECRs. In this interaction, UHE photons induce electromagnetic cascades. There is significant uncertainty for the background radiation spectrum in the universe, thus the energy loss length of UHE photons has the large uncertainty. Figure 3.1 shows the calculated energy loss length of photons [47]. Typical energy loss length is the order of 10 Mpc at the energy of 10^{19} eV. Therefore, UHE photons can arrive at the Earth from our galaxy or relatively nearby our galaxy.

It is important that photons are neutral particles, and they are not deflected by the magnetic fields in the universe. Thus, their arrival directions can be directly traced back to their origins. Because of the no deflection, their arrival timing would be correlated with other optical observations. If UHE photons are emitted by transient sources, such as gamma ray bursts and super novae, with other wavelength photons, origins of UHE photons are possibly identified with consideration for other wavelength observations.

In the case of SHDM models, SHDM particles may be concentrated at the galactic center region, and UHE photons as decay or annihilation products from SHDM particles would be observed as anisotropically from the galactic center region. Other top-down parents which are distributed relatively far from the Earth, thus the arrival directions of observed photons would have the relatively isotropic distribution. In the case of bottom-up scenarios, photons are mainly generated by GZK mechanism. Thus, their arrival directions may not point directly to origins of UHECRs but the distribution of the directions could show up the informations of sources.

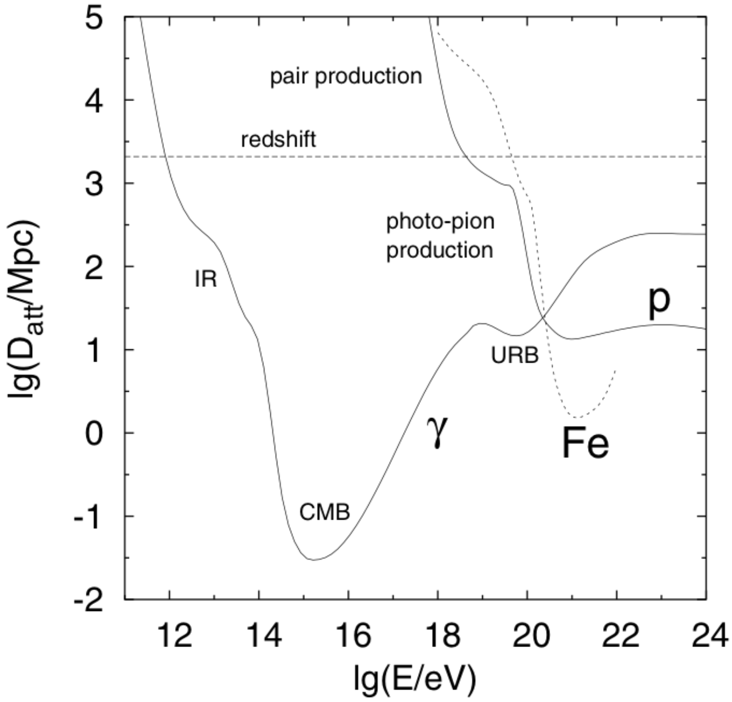

Figure 3.1: Typical energy loss lengths of UHE photons, protons, and iron nuclei in the universe [47]. There are three lines indicating the typical energy loss lengths for each primary, the primary of each line is indicated beside the each line. Interactions with infrared (IR), cosmic microwave background radiation (CMBR), and universal radio background (URB) photons are considered in this calculation. The dashed horizontal line indicates the energy loss length via adiabatic energy losses with redshift.

3.3 Flux predictions

In order to estimate expected photon flux at the Earth, we need to include the energy loss process in the propagation of UHE photons. For these calculations we need to assume the energy spectrum of background photons, and this uncertainty causes a systematic error on the predicted photon flux. Moreover, we also need to assume source information for flux estimations. For example, in the estimation based on a top-down model, the density and the lifetime of parent SHDM particles are assumed. On the other hand, in the calculation based on the bottom-up model the source distribution, the UHECR spectrum, and the composition are assumed. These uncertainties can be reduced by assuming and fitting observed cosmic ray energy spectra.

In the paper by Gelmini *et al.* [48, 49], various scenarios were used to fit the observed UHECR energy spectra from AGASA and HiRes. Figure 3.2 shows the predicted photon fractions for top-down models and GZK-photons. In this calculation, the energy spectra reported by AGASA and HiRes are used to fit the the simulated energy spectra of UHECRs. There are large difference between the photon fractions with using AGASA and HiRes energy spectra. This difference is caused by the difference between AGASA and HiRes energy spectra.

In order to fit the spectra 10^{19} eV, low energy component from galactic cosmic rays are also assumed.

In order to fit these energy spectra, different parameters are assumed in the study, the source spectrum, the maximum energy of UHECRs, and the minimal source distance, and also low energy components from galactic cosmic rays are assumed to fit the spectra below 10^{19} eV. These assumed parameters make the major difference of photon fraction. In addition, the abundance of radio background and the strength of the extragalactic magnetic field, which are alter the probability of the GZK interaction and mean free path of the UHE photons, are assumed to calculate GZK-photon fluxes, and it represent the band width of predictions of GZK-photon fraction.

In the case of top-down scenarios, these parameters are also assumed to fit the AGASA and HiRes energy spectra, but the lines showed in the figure are indicate minimal case of photon fraction with in the assumed parameter spaces in the study.

3.4 Photon-induced air showers

Photons which have sufficient energies initiate an almost purely electromagnetic cascade in the atmosphere. In addition to the ordinary cascading processes, it is necessary to consider additional processes for UHE photons, such as the pre-shower effect [50] and Landau-Pomeranchuk-Migdal (LPM) effect [51]. These processes are reviewed in this section. Furthermore, some specific and observable features of photon-induced EAS are discussed later in this section.

3.4.1 Pre-shower effect

In general, high energy photons interact with a magnetic field, and then they produce an electron and a positron through the pair production process. Erber showed single parameter, Γ, which is used for the determination of the threshold condition of this process [50],

$$\Gamma \equiv \left(\frac{E}{m_{\mathrm{e}}c^2}\right)\left(\frac{H_\perp}{H_{\mathrm{crit}}}\right), \quad H_{\mathrm{crit}} \equiv \frac{m_{\mathrm{e}}^2 c^3}{e\hbar} \simeq 4.414 \times 10^{13}\ [\mathrm{G}] \tag{3.4.1}$$

where E is the energy of the projectile electron, $H_\perp$ is the strength of the magnetic field perpendicular to the momentum direction of the primary photon, $m_{\mathrm{e}}c^2$ is the rest mass energy of electrons, and H_{crit} is called *critical field strength*.

This interaction can be occur even in weak magnetic fields, when the energy of primary photons is sufficiently high, such as UHE photons. The probability of this interaction become non-negligible at $\Gamma > 0.5$, and it corresponds to the primary photon energy of $\sim 10^{19}$ eV. Thus, a significant proportion of photons with energies above 10^{19} eV converts to electron-positron pairs in the geomagnetic field, and projectile electron components emit synchrotron radiation photons. Then, the averaged first interaction point of air showers reaches far high above the atmosphere, $\sim$ 1000 km above sea level for the primary energy of 10^{20} eV, as comparing with the mean free path of 100 g/cm^2 for the proton–air inelastic hadronic collations. This phenomenon is called *pre-shower effect*. Since the Erber's parameter Γ depends on $H_\perp$, the probability of the pre-shower effect depends strongly on the trajectories of primary photons in the geomagnetic filed and observation sites.

The typical height of pre-shower interaction is about 1000 km above sea level, and then subsequent electrons, positrons, and photons are induced in the atmosphere, and each of them create sub-showers in the atmosphere. The primary energy is divided into these sub-showers, and each sub-shower develops as lower energy shower than the primary photon. This bundle of sub-showers is observed as a single shower, because the lateral spread of the pre-shower particles and the difference of arrival timings are sufficiently small for the current UHECR detectors. As a result, X_{max} of the showers, which undergo the pre-shower effect, become small.

3.4.2 Landau-Pomeranchuk-Migdal effect

In a medium, the cross-section of the pair production process is suppressed due to a quantum mechanical interference in very high energies [51–53]. This is called *LPM effect*. The reduced cross-section σ_{LPM} is approximately derived as

$$\begin{aligned} \sigma_{\mathrm{LPM}} &= \sigma_{\mathrm{BH}}\sqrt{\frac{E_\gamma E_{\mathrm{LPM}}}{E_{\mathrm{e}}(E_\gamma - E_{\mathrm{e}})}}, \\ E_{\mathrm{LPM}} &\approx (7.7\ [\mathrm{TeV/cm}]) \times X_0, \end{aligned} \tag{3.4.2}$$

where $\sigma_{\rm BH}$ is Bethe-Heitler cross-section (≈ 0.51 b in air), E_γ is primary photon energy, $E_{\rm e}$ and $(E_\gamma - E_{\rm e})$ are electron and positron energies emitted by the pair production, X_0 and ρ are the radiation length and the density of media, respectively. For example, in the reference [52], $E_{\rm LPM} \sim 2.8 \times 10^{17}$ eV at 300 m a.s.l. and $E_{\rm LPM} \sim 10^{19}$ eV at the upper atmosphere.

It causes delay in the shower development at the initial phase of electromagnetic cascades initiated by UHE photons, because primary photons can penetrate deeper into the atmosphere than if the cross-section is not reduced by the effect. It should be noticed that the fluctuation of the shower development becomes large, since $\sigma_{\rm LPM}$ decreases with increasing the atmospheric depth.

3.4.3 Features of photon-induce EASs

In contrast to nucleus-induced EASs, photon-induced EASs suffer the additional effects as reviewed above in this section. Therefore, photon-induced EASs show different developments from nucleus-induced EASs. The difference on the shower developments can be seen in the difference on $X_{\rm max}$. Figure 3.3 shows averaged $X_{\rm max}$ values for different primaries [47]. Photons have a large slope of the averaged $X_{\rm max}$, called *elongation rate* ($\mathrm{d}X_{\rm max}/\mathrm{d}\ln E$), and thus their averaged $X_{\rm max}$ are significantly larger than that of nucleus primaries at energies above 10^{16} eV. At energies around 10^{19} eV the elongation rate gradually increases due to the LPM effect, and also the $X_{\rm max}$ rail of photons has a sharp cutoff at 10^{20} eV due to the pre-shower effect. The energy threshold of the pre-shower depend on the trajectories of EASs as discussed above. Figure 3.4 shows average $X_{\rm max}$ dependency on shower geometries at the TA site [54]. If photon-induced EASs come from the north direction, the pre-shower effect begins lower energy than that of the south direction.

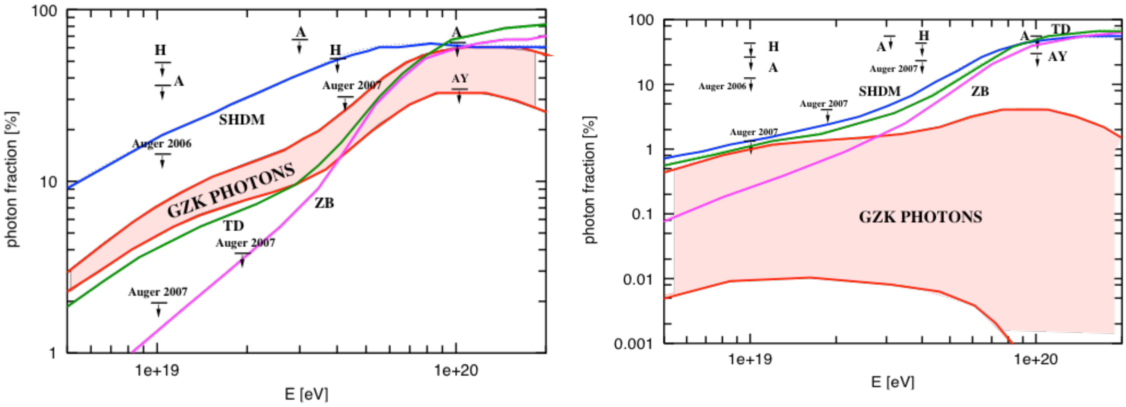

Figure 3.2: Predicted ratios of photons to integrated all particle flux above each energy as a function of primary energy for AGASA (*left*) and HiRes (*right*) [48] energy spectra in percentage, and upper limits from AGASA (A), AGASA and Yakutsk collaboration (AY), Haverah Park (H), and PAO. The shaded regions show the range of GZK-photon fractions. The upper bands and lower bands are the minimum and maximum fraction derived from different assumptions, respectively. The lines indicate minimal photon fractions calculated by top-down scenarios, SHDM (blue), Z-burst (ZB, pink), and TD (green) models.

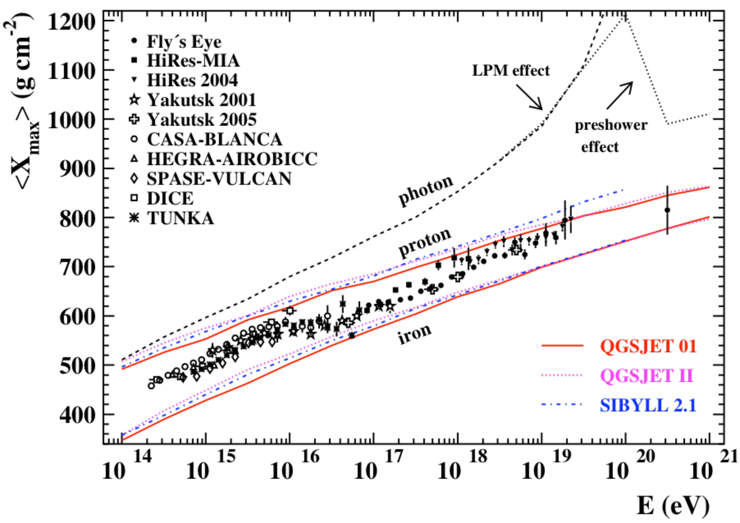

Figure 3.3: Averaged X_{max} obtained from simulations for different primaries and from experimental data [47]. The lines show predicted averaged X_{max} with different high energy hadronic interaction models. The elongation rate for the photon primaries changes at around 10^{19} eV due to the LPM effect. The splitting of photon line shows different trajectories of primary photons, because interactions related UHE photons depend on specific trajectories through the geomagnetic field.

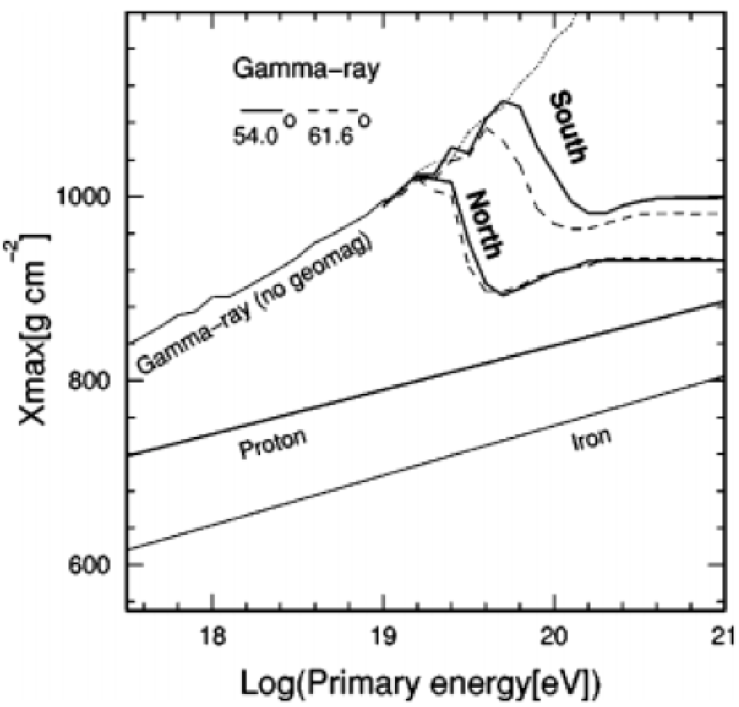

Figure 3.4: Average of $X_{\max}$ for photons, protons, and irons induced EASs [54]. Low and high energy interaction models used in this calculation are AIRES and QGSJET. There are five lines for photons, the dots curve indicates the case of no geomagnetic field. The thick solid lines and dashed lines are calculated zenith angle of 54.0° and 61.6°, respectively

Chapter 4

The Telescope Array experiment

The Telescope Array (TA) experiment is the largest observatory for UHECR in the northern hemisphere and it is located at 39.3° N, 112.9° W, and about 1400 m above sea level, Utah, USA. The experiment is operated by the international collaboration of Japan, USA, Korea, Russia, and Belgium, since 2003. TA consists of three fluorescence detectors (FDs) [55] and an array of 507 surface detectors (SDs) [56]. Figure 4.1 shows a map of the TA experiment. The area covered by the SD array is about 680 km^2, and the FDs are located at around the SD array viewing over the SD array. The FDs and SDs sample cosmic ray air showers by different methods, and each sampled data are used complementary to reconstruct the air showers.

4.1 Surface detectors

4.1.1 Detector

The air shower array consists of 507 surface detectors (SDs) deployed on a 1.2 km spacing square grid. The SD for the array is autonomic detector, and each SD consists of two layers of 3 m^2 plastic scintillation counters, a data acquisition and control electronics, a GPS receiver, a wireless LAN interface. Each SD is powered by one solar panel and one deep cycle buttery. The charging power of the solar panel is 125 W, and the buttery capacity is 100 Ah. Figure 4.2 shows a schematic view of inside of the scintillation counter. Thickness of the plastic scintillator is 1.2 cm, and a stainless plate is inserted between the two layers to avoid cross-talk photons. Scintillation photons induced by passages of charged particles are sampled by wavelength shifting fibers laid on the surface of the scintillator and are led into a photo multiplier tube (PMT) for each layer. Output of each PMT are successively digitized by a 12 bit FADC with sampling time of 20 ns.

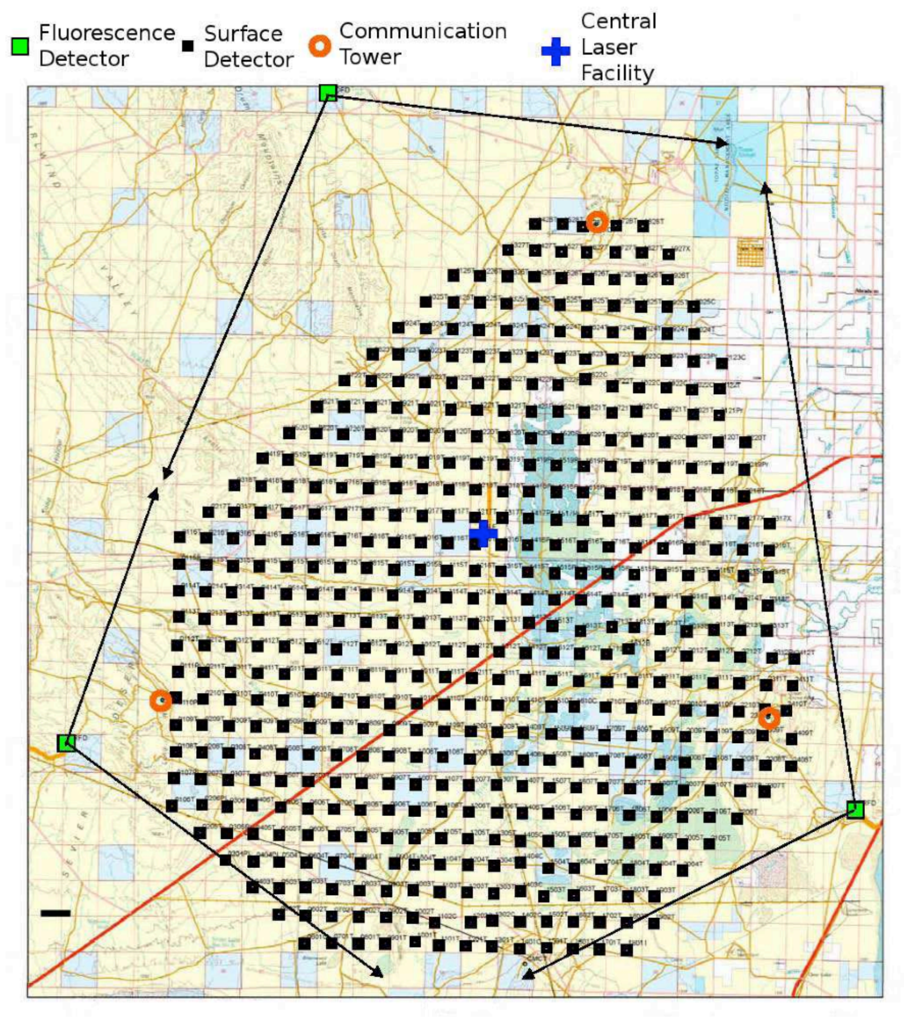

Figure 4.1: A map of the TA experiment showing the location of the FD station and SDs indicated by the green squares and the black squares, respectively. The blue cross shows the location of the Central Laser Facility, and the orange circles are that of the communication towers. The arrows show azimuthal extent of the field of view of each FD station.

4.1.2 Trigger and data acquisition system

There are three communication towers at the edges of the SD array, that provide wireless communication to each SD. This network is used to triggering the SDs and to store the data. The SD trigger routine consists of two parts. The first part is the local trigger on each detector, and it makes for an SD electronics to store waveforms to its buffer memory. The second is the array trigger, and it makes for all SDs to send the buffered waveforms the communication towers.

The local trigger has two levels labeled *level-0* and *level-1* trigger. The level-0 trigger is generated when the pulse height signals reaches the height equivalent to 0.3 minimum ionizing particle (MIP) passage, and the level-0 triggered SD stores the waveform including the triggered signal with 2.56 μs span into the buffer memory. The FADC counts equivalent to the 1 MIP is monitored with this waveform by integrating the bins between -4 bins from trigger timing and $+8$ bins after trigger timing. Figure 4.3 shows an example of 1 MIP histogram. This histogram is collected every 10 minutes for monitoring 1 MIP variation.

When the signals from the upper and the lower layers coincidently exceed three MIPs height within 160 ns, the level-1 trigger is generated, and the trigger timing information is stored. Timings of level-1 triggers are accumulated for one second interval, and the set of the information, which is called *trigger table*, is sent to the host electronics at the communication tower in the following interval.

The accumulated trigger tables are checked by the trigger-decision logic on the host electronics. An event trigger, called *level-2* trigger, is generated by the host electronics when three or more adjacent SDs have recorded level-1 triggers within the timing difference of 8 μs. Figure 4.4 shows possible hit patterns to generate a level-2 trigger. Then, the host electronics distributes the event trigger information to all the SDs. Each SD electronic searches for the coincident waveform with the level-2 trigger in the buffer memory. If it is found, the SD electronics send it to the host electronics together with its timing information.

The average trigger rates are about 750 Hz and 30 Hz for level-0 and level-1 trigger, respectively. Level-2 trigger rate is about 0.01 Hz, and corresponding trigger efficiency of the the SD array is about 50% at the energy of $10^{18.5}$ eV.

In addition to the level-1 trigger information, SDs send monitor data to the host electronics every second. The monitor data include the information about the gains of PMTs, environmental conditions, GPS reception conditions, power generation and consumption status, etc. Details of the monitor data can be found in the reference [56].

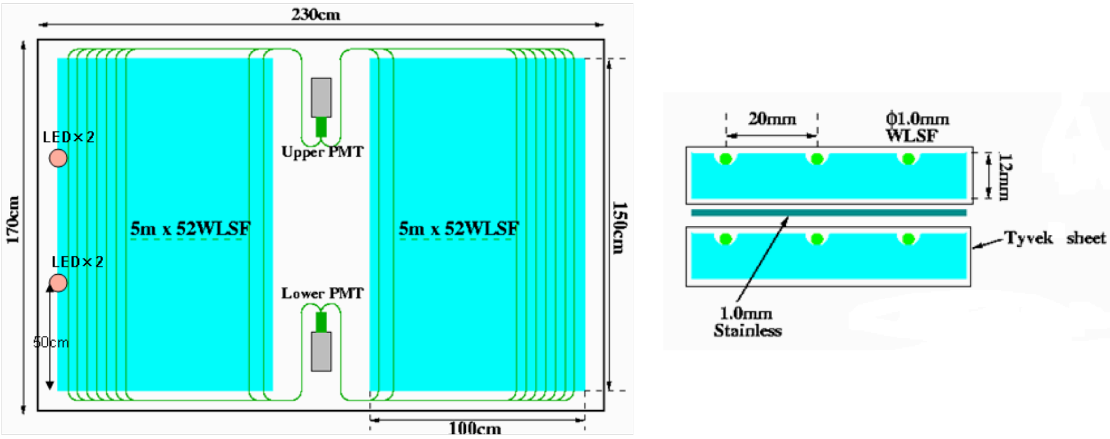

Figure 4.2: (*Left*) the schematic view of inside of the scintillation counter. (*Right*) the side view of the two layers plastic scintillators.

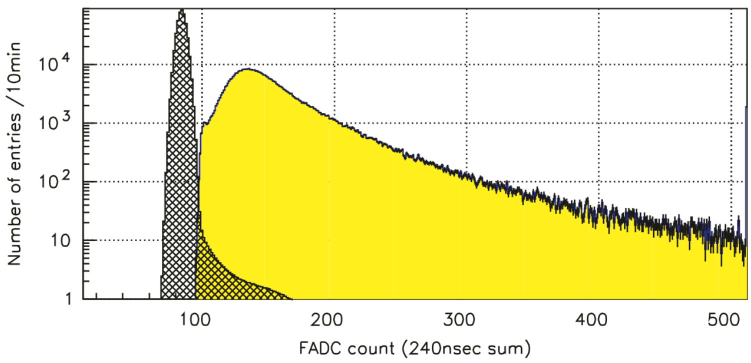

Figure 4.3: Example of FADC count distribution of a SD calculated from level-0 triggered waveform. The hatched histogram is a pedestal distribution. This distribution is collected for every PMT every 10 minutes.

4.2 Fluorescence detectors

4.2.1 Detector

The TA experiment has three fluorescence detectors (FDs). One of them consists of refurbished HiRes-I mirrors, PMTs, and re-engineered electronics. This FD is located in the northern part of the TA site which called Middle Drum (MD), station named after the neighboring mountain (see Figure 4.1). The others are newly designed and produced detectors. These two FDs are located in the south-east and south-west of the TA site, and they are called Black Rock Mesa (BR) and Long Ridge (LR) stations, respectively. Data obtained with BR and LR stations are used for the analyses in this thesis, thus details of these two FDs are mainly described in the followings in this section.

BR and LR stations have almost the same detector configuration. Each station has twelve telescopes, and they are grouped into two groups, called *ring*, such as *the lower viewing ring* and *the upper viewing ring*. Each station covers the field of view (FOV) of 3° to 33° in elevation angle and 108° in azimuthal angle. The field of view covers the whole area of the SD array. Figure 4.5 shows the appearances of the BR station buildings and telescopes in the station.

Each telescope consists of a large spherical mirror, which consists of 18 segments. The diameter of the mirror is 3.3 m and the curvature is 6.067 m. The imaging camera is installed on the prime focus of each mirror, and It consists of 256 PMTs. The front window of the camera box is made of UV transparent acrylic plate, paraglas UV00 by Kuraray co., ltd., and a UV transparent bandpass optical filter, BG3 by Schott, is attached on every photo cathode window. The night sky background photons are reduced by the filter, and the typical background level is $\sim$ 30 photoelectrons in 100 ns. The transmittance spectrum of the filter has a necessary and appropriate width to transmit air fluorescence photons. Figure 4.6 shows the typical transmittance of the UV00 and BG3. The PMTs are manufactured by Hamamatsu Photonics K.K., and R9508 based on R6234-01 with a printed circuit board include a bleeder and a preamplifier, which are used for the PMTs at BR and LR FD stations. The PMT has a hexagonal bialkali photo-cathode and borosilicate glass window, and the size of the window is a distance of 60 mm between the parallel sides. A printed circuit board which includes a bleeder and a preamplifier is installed on the bottom of each PMT. The PMT has eight dynodes, and the gain is $\sim 8 \times 10^4$ with 800 V. The FOV of each PMT is approximately 1°. The PMT gains are relatively monitored and adjusted to absolutely calibrated *standard* PMTs [57]. The gains of standard PMTs are monitored by small light pulser of YAP ($YAlO_3$:Ce-Am light pulser) [58], which is mounted on the photo cathode surface of each standard PMT. The gains of other PMTs are monitored relative to the standard PMTs with a Xe flasher installed at the center of each mirror [59].

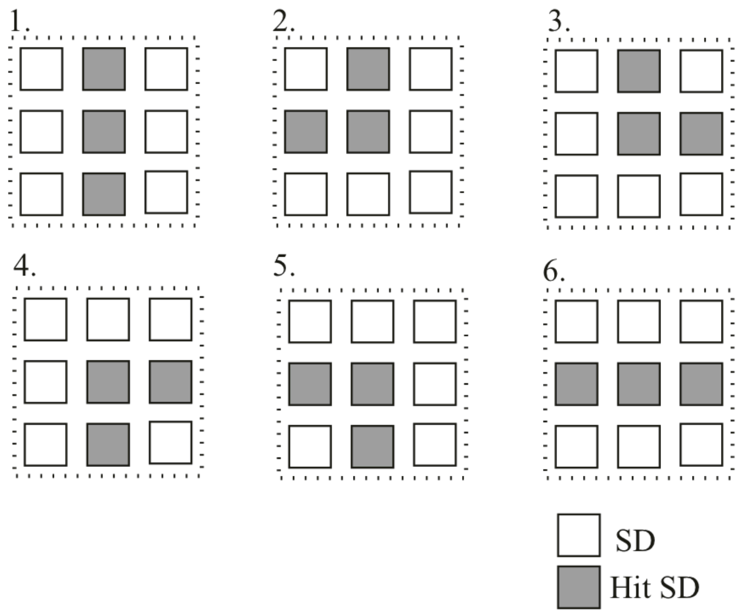

Figure 4.4: The possible hit patterns to generate a level-2 trigger.

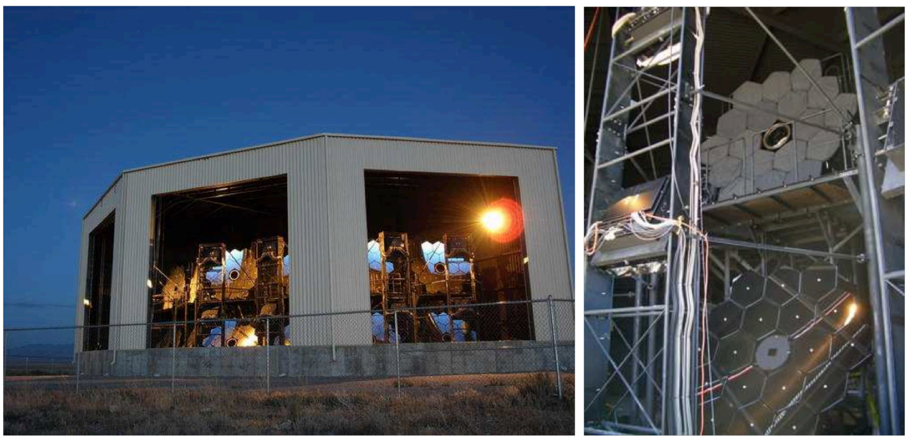

Figure 4.5: (*Left*) an appearance photograph of the Black Rock Mesa FD station building. (*Right*) the photograph of one of the pair of upper and lower ring telescopes.

4.2.2 Trigger and data acquisition system

FDs have three types of VME electronics modules, signal digitizer/finder (SDF), track finder (TF), and central trigger distributor (CTD). Figure 4.7 shows a block diagram of these modules. Output signals from each PMT pass through a DC-coupled pre-amplifier, and it is digitized by a FADC on SDF with 12 bit 40 MHz sampling rate. Then, four consecutive bins are combined to one bin in the SDF, *i.e.*, it works as 14 bit and 10 MHz sampling rate digitizer. One SDF module processes 16 input channels and 16 SDF modules are installed for each camera. The output from 16 SDFs are processed on the TF module to find a track in the signals recorded in the camera. The TF module is installed for each camera, and output from 12 TF modules are processed on CTD to trigger the all cameras.

The triggering logic of the FDs consists of three levels [60]. The *level-1* trigger on individual PMTs is generated in the SDFs. The SDF slices the data into 25.6 μs frames containing 256 bins of FADC data samples, which has an overlap of 12.8 μs between adjacent frames. The SDF calculates moving averages for four time windows (1.6, 3.2, 6.4 and 12.8 μs) and compares them with the background level. The background average and standard deviation is calculated from past 1.6 ms, and they are updated every 0.4 ms. When the SDF finds an excess greater than 6 sigma above the background level, it sends an level-1 trigger to the TF module of the camera. The average trigger rate is about 3 Hz with 6 sigma threshold level for the level-1 trigger. The *level-2* triggers are generated by the TF that performs pattern recognition for level-1 trigger maps of each camera.

There are two modes to search for air shower tracks on hit maps by TF. One is searching for well-contained tracks in the camera's FOV. TF scans over hit maps of cameras with a 5×5 pixel subarray window (Figure 4.8). When a hit pattern of the subarray matches one of the patterns on the look-up table, TF generates a level-2 trigger and sends it with tagging *complete track* code to CTD.

The other mode is searching for shower tracks across the edges of cameras. In this mode, TF scans hit maps of cameras along the camera edges with 4×4 pixel subarray window (Figure 4.9). When a hit pattern matches the look-up table for this mode, TF send the level-2 trigger with the *partial track* code to CTD.

CTD judges a final trigger decision as a *level-3* trigger. CTD generates a level-3 trigger, when CTD receives at least one level-2 trigger with the complete track code, or when it receives more than two level-2 triggers with the partial track code from adjacent cameras. Then, CTD provides a level-3 trigger to all the cameras in a station. The level-3 trigger makes all the PCs which control individual cameras to start storing waveforms from all the PMTs in each camera. This trigger rate is about $1 \sim 3$ Hz in a stable observation night.

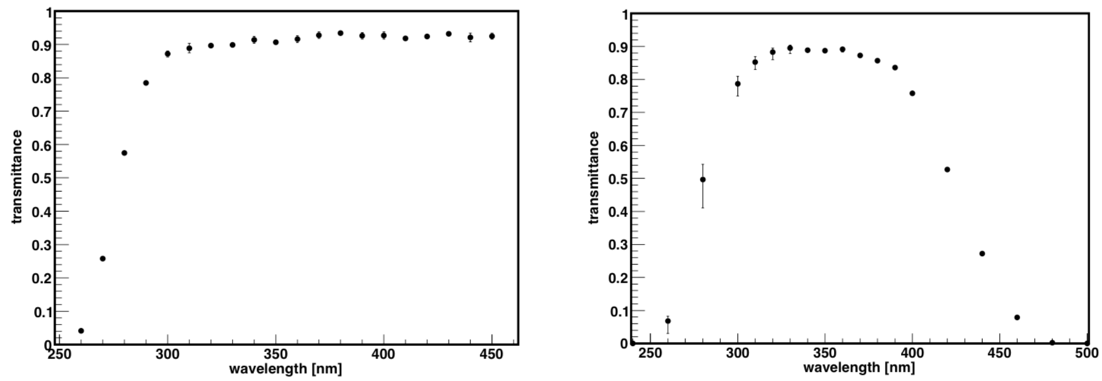

Figure 4.6: (*Left*) the typical transmittance of the acrylic plate, UV00, the data points are the median value for three samples, and errors indicate the differences between the median and the otter two samples. (*Right*) the typical transmittance of the UV filter, BG3 filter, and the data points are the medians for all sampled filters with the bars corresponding to one standard deviation.

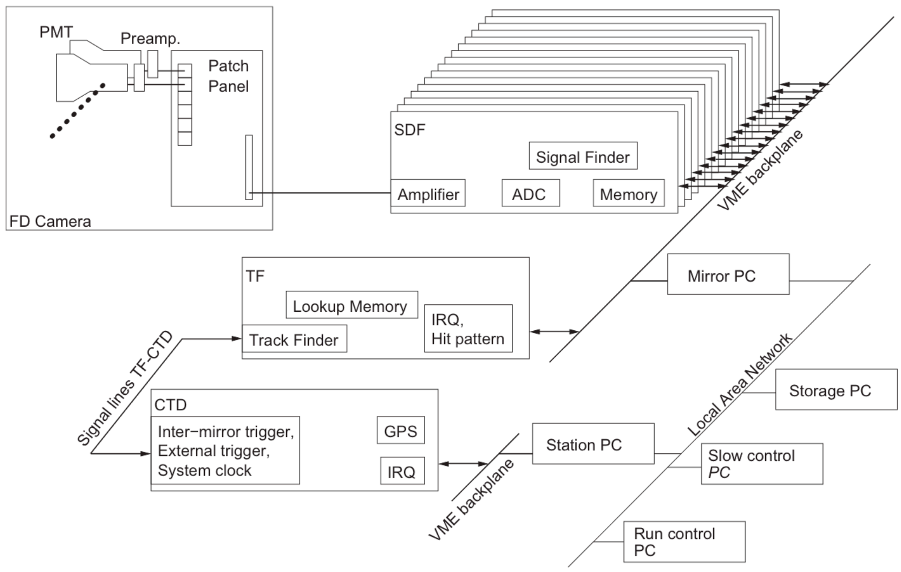

Figure 4.7: A block diagram of the triggering electronics and data acquisition system of FD [60].

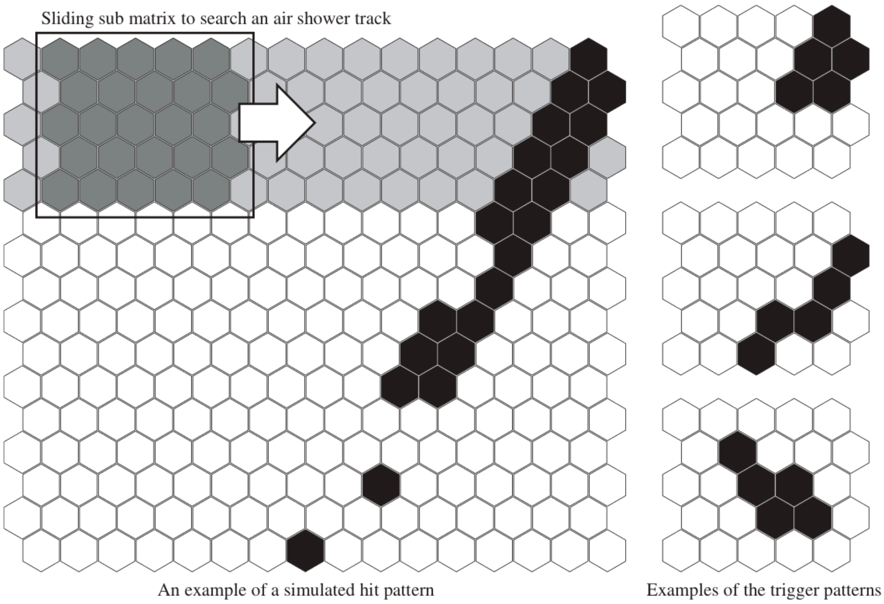

Figure 4.8: A schematic diagram of the complete track finding process [60].

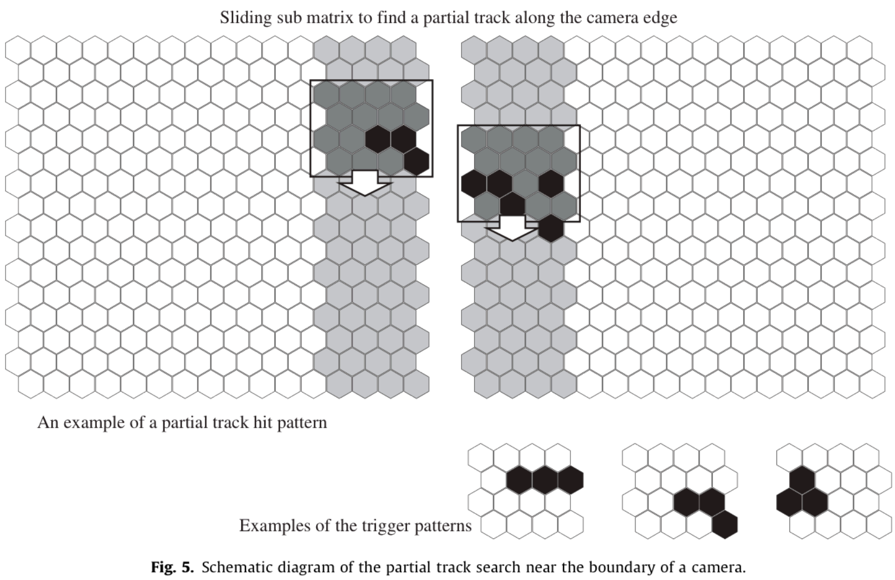

Figure 4.9: A schematic diagram of the complete track finding process to find a partial track pattern across boundaries of adjoining two cameras [60].

4.2.3 Atmospheric monitoring

In order to reduce systematic errors and to keep the high event reconstruction accuracy the TA experiment has various monitoring systems for the atmospheric condition.

Central laser facility

The central laser facility (CLF) is located in the center of the TA site, 20 km away from all three FDs. CLF has a 355 nm Nd:YAG laser, Ultra CFR by Quantel. In usual air shower observations with FDs, CLF shoots the laser into the FOV of FDs for 300 times every half hour with 10 Hz repetition rate, which are observed by all the FDs, and FDs observe side scattered photons of the laser. The total amount of side scattered photons induced by a 5mJ laser shot is equivalent to the total fluorescence photons induced by the air shower with primary energy of 10^{20} eV.

CLF is an important tool for understanding the atmosphere at the TA site. The atmospheric transmittance and the vertical aerosol optical depth (VAOD) can be estimated by comparing observed CLF events to that of simulations.

LIDAR

Light detection and ranging (LIDAR) is widely used technology for monitoring aerosols. In the TA experiment, the LIDAR system was installed at 100 m apart from the BR station. The LIDAR system consists of 355 nm Nd:YAG laser and telescope. The LIDAR system observe backscattered laser light by atmospheric molecules via Rayleigh scattering and by aerosols via Mie scattering. The time profile of backscattered light relates to the density profiles of atmospheric molecules and aerosols along with the laser beam. Therefore, the atmospheric parameters, such as VAOD, can be estimated by LIDAR observation [61]. The typical attenuation length of Mie scattering on the ground and scale hight of aerosol distribution are 29.4 km and 1.0 km, respectively, that corresponds the VAOD at the 3.5 km is 0.033. These values are determined by this LIDAR measurements, and they are used in the analysis of this thesis.

4.2.4 Cloud monitoring

The existence of clouds in the FOV causes unexpected photon scattering, and then it causes the systematic errors on EAS reconstructions. Thus, we need to continue to monitor clouds during every FD observation night. The TA experiment has two methods to monitor to evaluate the cloudiness.

IR camera

The TA experiment has an infrared (IR) camera to take IR pictures, which correspond to temperature measurement of the sky, of the FOV of the BR station. If it is cloudy, the temperature in the cloud region is relatively higher than the clear sky region. In the usual FD operations, the IR camera take twelve pictures which correspond to the telescopes' FOV every 30 minutes. Figure 4.10 shows the appearance of the IR camera and photographs taken by the camera. In the analysis of the IR camera pictures, each picture is divided into four separated regions in the horizontal direction. Then, the existence of cloud is determined by the temperature in each region [62]. However, the IR camera is not operated all the observation night, there is another cloud monitoring method in our experiment.

WEAT code

In the MD station, an operator watches the existence of clouds every hour by own eyes. The result for each time is recorded as a numerical code called *WEAT code*. The code indicates the existence of clouds in the north, east, south, west, and zenith directions. Additionally, the code includes the cloud coverage parameter in the whole sky and the transparency of the horizontal direction. Since WEAT code is recorded in all of observation nights when MD FD is operated, the code can be used all of the observation terms. The consistency between the WEAT code and the IR score is confirmed [62].

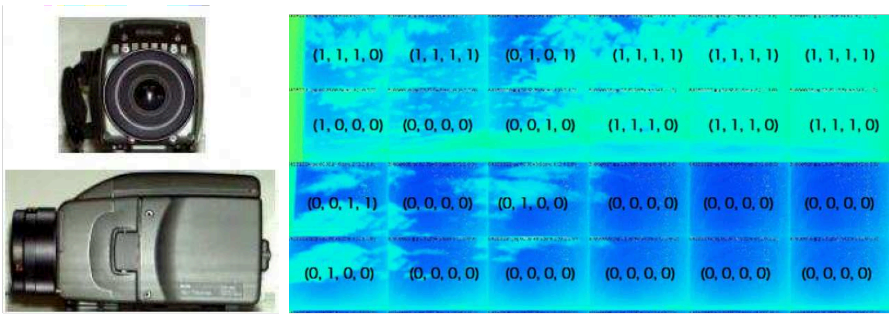

Figure 4.10: The appearance of the IR camera (left) and the twelve pictures taken by the IR camera at two different times (right). The numbers shown in each picture indicate the existence of clouds or not by 1/0 for in four separated regions in each picture.

Chapter 5

Monte Carlo simulation and shower reconstruction procedures of the hybrid analysis

In order to evaluate reconstruction accuracies and systematic errors for observed results with a complex detector we use Monte Carlo (MC) simulations. In this chapter, the shower reconstruction and the simulation methods of hybrid technique are presented.

5.1 Monte Carlo simulations

For the hybrid event analysis in the TA experiment, there are three steps for EAS event simulation. First, EASs are simulated with de facto standard MC simulation package called *CORSIKA*, which is described in Section 5.1.1. Second, detector responses of SDs are calculated using *GEANT-4*, which is a standard simulation package developed by CERN, and it is discussed in Section 5.1.2. Third, detector responses of FDs are calculated using the software which is developed by the TA collaboration, and the detailed descriptions are presented in Section 5.1.3.

5.1.1 Extensive air shower simulations

In the study described in this thesis, EASs are simulated with the Cosmic Ray Simulations for KASCADE (CORSIKA) package [63]. This package was firstly developed for the KASCADE experiment, and now, is generally used as a de facto standard in the field of cosmic ray physics. CORSIKA allows us to simulate EASs with various primary particle types and primary energies. Moreover, we can set various parameters to control EAS simulations. Table 5.1 shows a list of the most important parameters, options and set values which are used in this work. E_{cut} in the table gives the lower energy limit of particles. When the particle's energy reaches this limit, CORSIKA stops tracking the

Table 5.1: A list of most important parameters used for the CORSIKA simulations in this work.

E_{cut} (hadrons)	50 MeV
E_{cut} ($\mu^{\pm}$)	50 MeV
E_{cut} ($\mathrm{e}^{\pm}, \gamma$)	250 keV
Thinning factor	10^{-6}
High energy interaction models	QGSJET-II-03 & EPOS-LHC
Primary particles	Proton & Photon
Energy range	from $10^{18.0}$ to $10^{20.5}$

particle and deposit its all remaining energy to the atmosphere.

For primary cosmic rays above 10^{18} eV, the number of secondary particles becomes too large to trace all of the particles. Therefore, for high energy simulations with CORSIKA, we use the *thinning* option to reduce the number of secondary particles to trace, and it can be set a weight to a particle. The weighted particle represents many particles of the same species with the weight to ensure that the energy and the momentum are conserved. When the thinning option is applied to CORSIKA, secondary particles are combined at any stage in the EAS development when their energies reach lower than the energy of,

$$E_{\mathrm{particle}} < \epsilon_{\mathrm{th}} E_0, \tag{5.1.1}$$

where E_0 is the energy of the primary cosmic ray, and ϵ_{th} is the thinning factor. The weighted particle is chosen randomly from all of the low energy particles. The thinning factor of 10^{-6} is used in this work.

The thinning causes large fluctuation in the lateral distribution of the particle density. The fluctuation in the lateral particle distribution does not affect the production of fluorescence photons, and therefore, thinned showers work well for FD simulations, because production of fluorescence photons depends on the overall deposited energy in each step of the shower development. On the other hand, the fluctuations in the lateral density distribution at the ground level cause systematic effects on SD simulations. Then, thinned air showers can not be used directly for practical SD simulations. In order to respond this situation, a method has been developed by the TA collaboration to recover the information lost by thinning and to successfully use thinned showers for practical simulations. This process is called *dethinning*, and the overview of this process is described in the followings in this subsection.

Dethinning CORSIKA air showers

The overview of the dethinning process is described in this subsection, and the details of the dethinning process is described in the reference [64]. In the dethinning process, weighted particles are spread out before the ground to restore the realistic information, which is lost by the particle thinning in CORSIKA simulations [64]. In the dethinning process, first, the vertex point of the weighted particle is chosen in the trajectory of the weighted particle with requirement that no particle can have an arrival times that precedes the arrival timing of the shower front. An early arrival timing occurs when the total time-of-flight from the first interaction point, $\mathbf{x_0}$, to the vertex point and then to the position on the ground of the dethinned particle is less than the time-of-flight directory from $\mathbf{x_0}$ to the arrival position of the dethinned particle. In fact, there is a maximum distance between the vertex point and the arrival position of the weighted particle. When the time and position of first interaction are t_0, and $\mathbf{x_0}$, and the arrival time and position of weighted particle on the ground are t_i and $\mathbf{x_i}$, respectively. The maximum distance, D_{max}, along the unit vector of the weighted particle trajectory, $\hat{\mathbf{p_i}}$, is calculated as

$$D_{\mathrm{max}} = \frac{c^2(t_i - t_0)^2 - |\mathbf{x_i} - \mathbf{x_0}|^2}{2\left\{c(t_i - t_0) - (\mathbf{x_i} - \mathbf{x_0}) \cdot \hat{\mathbf{p_i}}\right\}}, \tag{5.1.2}$$

where c is a speed of light. The D_{max} is the maximum distance, and any shorter distance can be chosen for the vertex point.

Second, trajectories of the dethinned particles are chosen by a two-dimensional Gaussian with the σ of a few degrees. The σ is set to βd, where d is the lateral distance from the shower core to the weighted particle and $\beta = 3^\circ/\mathrm{km}$ for electromagnetic particles and $\beta = 1^\circ/\mathrm{km}$ for muons and hadrons. These values for β is empirically determined by comparison between unthinned showers and dethinned showers.

Third, crossing points between the chosen trajectories and the ground level are calculated as arrival points of the dethinned particles, and arrival timings and energies are assigned to the dethinned particles. In fact, the timing is calculated by the trajectory of each particle, and the energy is determined by the Gaussian distribution centered on the energy of the weighted particle with $\pm 10\%$ energy of sigma. Figure 5.1 shows an example of a geometry determination for a dethinned particle.

To validate the dethinning process, approximately 100 unthinned air showers with primary energies greater than 10^{18} eV were generated and compared with the air shower data produced by the dethinning process. As a result, the lateral distributions produced by the dethinning procedure agree with the unthinned lateral distributions [65]. Figure 5.2 shows the comparison of secondary electron spectra with and without dethinning [64]. For each histogram, good agreement is observed between thinned and dethinned simulations, and dethinned spectra are smoothed by the dethinning procedure.

5.1.2 Detector simulations for surface detectors

The dethinned CORSIKA simulations are used for the SD simulations. Each CORSIKA shower is used repeatedly with random different core positions to reduce the calculation time. For SD simulations with proton primaries, each proton shower is also used repeatedly with random different azimuthal angle. In contrast, for photon primaries, the shower

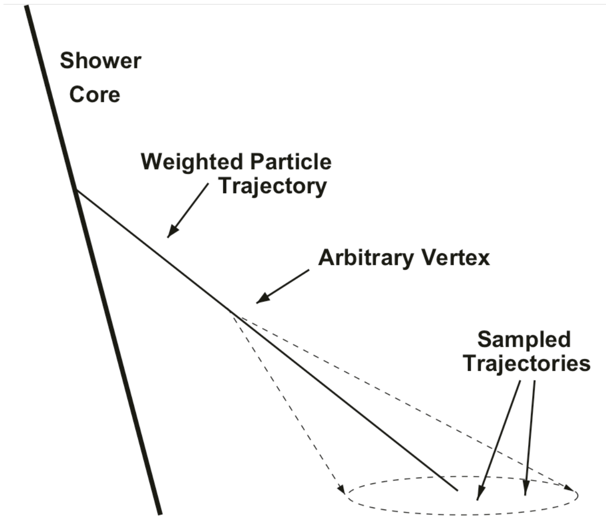

Figure 5.1: Schematic view for geometry of a dethinned particle [64]. Vertex position is chosen on the trajectory of the weighted particle as described in text.

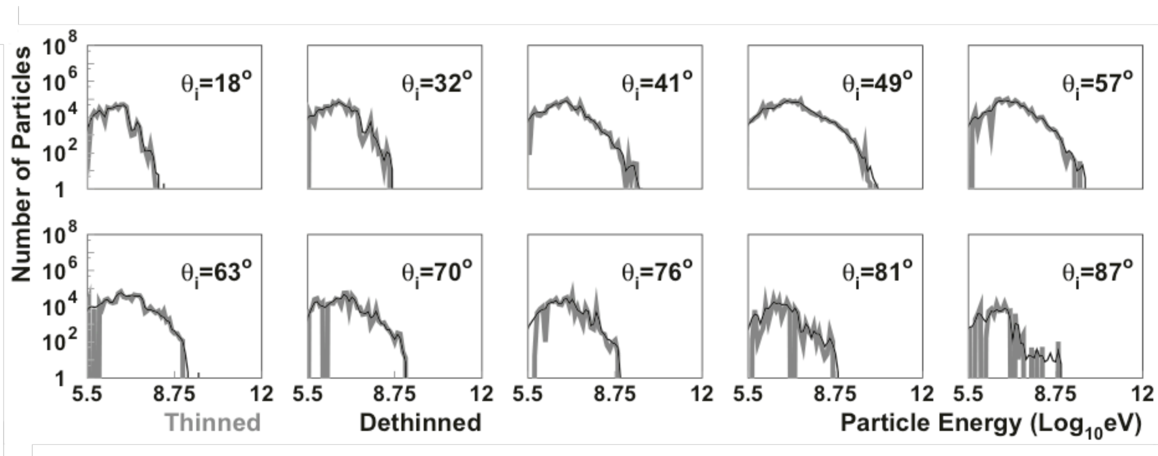

Figure 5.2: Comparison of secondary electron spectra with and without dethinning for a thinned simulation of a proton-induced EAS with primary energy $E = 10^{19.0}$ eV and primary zenith angle $\theta = 45°$ [64]. Horizontal axis is the kinetic energy, and vertical axis is the number of particles. Spectra for thinned simulation are showed by gray, and dethinned spectra are showed by black. The secondary electrons within a region from $-30°$ to $30°$ in azimuthal angles with respect to the azimuthal angle of the primary particle direction, and within a region from lateral distances from 500 m to 1000 m are tabulated in these figures. The angle showed in each figure is incident angle with respect to the ground.

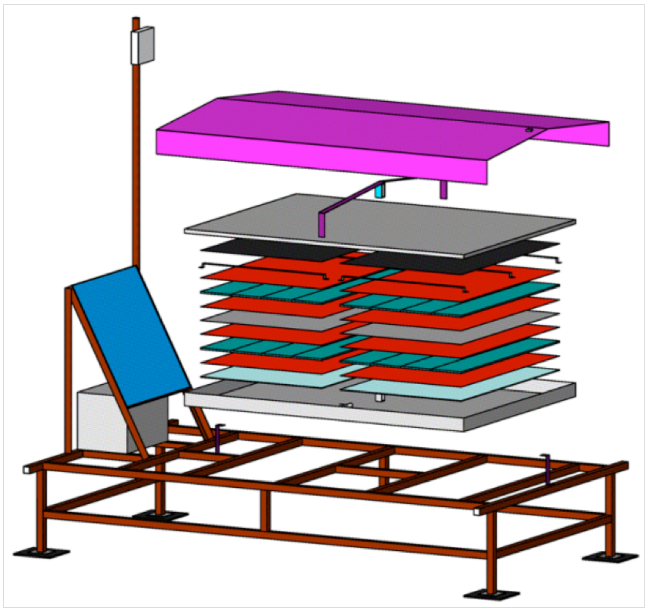

Figure 5.3: Overview of the simulated SD configuration in the GEANT4 simulation. It includes many of the components for realistic simulation, such as scintillators, mounting parts, a stainless-steel box, a battery, a solar panel, wireless antenna, and so on.

development depends on their azimuthal angles because of preshower effect as discussed in Section 3.4.1.

The energy deposit processes on each SD are simulated by GEANT4 simulation package. The SD construction is simulated accurately in the GEANT4 simulation. The TA SD is accurately constructed as a digital model using GEANT4 library as shown in Figure 5.3. Deposited energies for passing particles with various different incident angles, momenta, and species are calculated.

To save conputing time of the SD simulations, energy depositions in the scintillators have been simulated thousands of times and the results are combined to a look-up table. The table is read out with the index made from the parameters of injected particles, which are outputs of dethinned CORSIKA simulations.

Then, energies deposited in the scintillators and time dependent SD calibration information are combined for simulation of digital output waveforms by the SD electronics. The triggering process described in Section 4.1.2 is also included in the simulation calculations.

Background signals induced by secondary cosmic rays are also simulated to make realistic simulation data. The simulated background signals are generated from COSMOS simulated secondary cosmic rays based on the energy spectra of primary cosmic rays for all the primary species measured by AMS [66, 67]. Figure 5.4 shows the energy spectra of

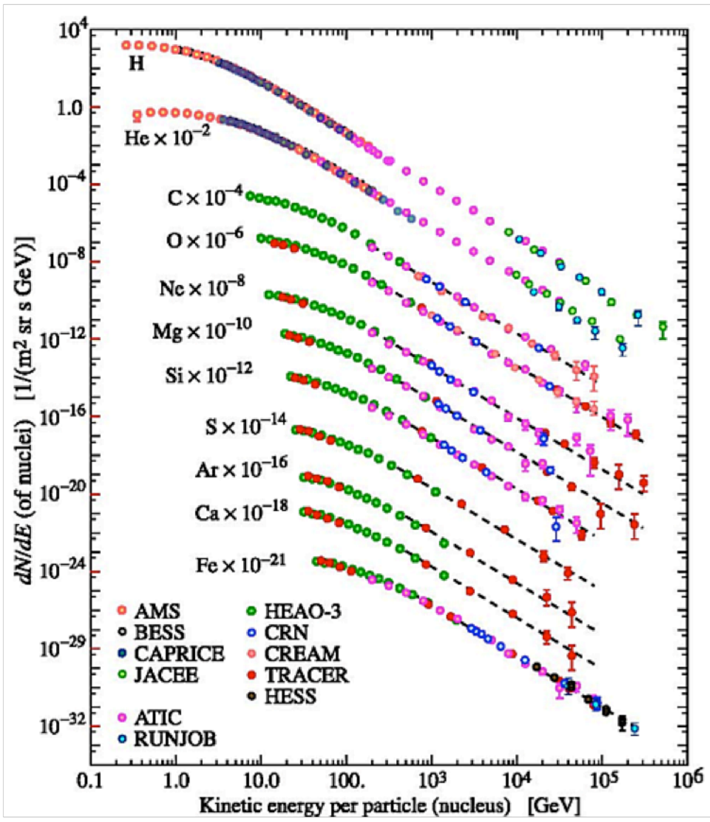

Figure 5.4: The cosmic ray energy spectra for some primary species measured by AMS [66, 67].

the considered primary cosmic rays. The simulated background signals agree well with the measured background signals. Details of this analysis were described in the references [68] and [69]

Finally, the waveforms are packaged in the same format as the real data.

5.1.3 Detector simulations for fluorescence detectors

Simulation tools for FDs has been developed in Java with the TA collaboration. The longitudinal development of energy depositions simulated with CORSIKA are used in the FD simulations, because productions of fluorescence photons are induced by energies deposited in the atmosphere. To simulate EASs as hybrid events, it is necessary to use the same EASs in both the SD and the FD simulations. Thus, the shower development of simulated showers are packed in a look-up shower library, and it also enable to reduce computing time.

Energy depositions are converted to fluorescence photons taking into account the wavelength spectrum described in Section 2.2.4, and parameterized atmospheric conditions.

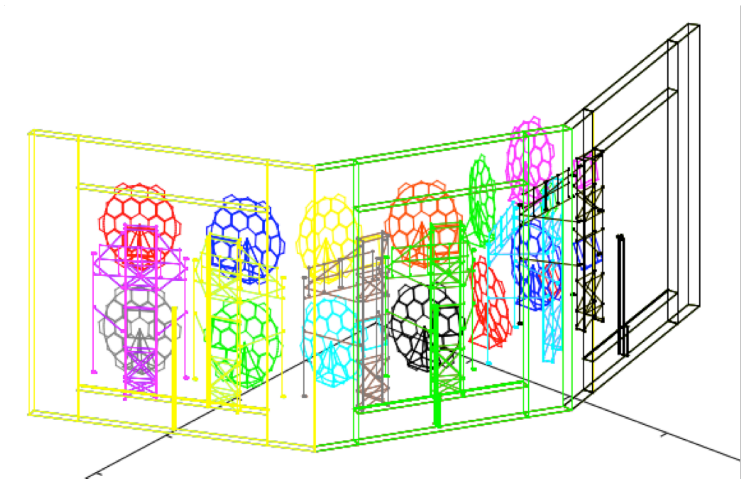

Figure 5.5: A digital model of a FD station building in the FD detector simulation.

The atmospheric condition parameters are obtained from results of the LIDAR operations and radiosonde data. The radiosonde data are allowed universal access to all in at the web site [70]. We take into account not only fluorescence photons, but also Cherenkov photons. After photon production processes, the number of photons is reduced with suffering atmospheric attenuations and the solid angle of FDs.

Remaining photons trace to PMTs with considering the obscurations by the structures of the FD station. Figure 5.5 shows a digital model of a FD station building in the FD detector simulation. The photons which hit a mirror are reflected with additionally including a random fluctuation following the Rayleigh distribution with approximately $\sigma = 0.06$ degrees (different measured values are used for each mirror). The parameter, σ, corresponds to the averaged adjustment accuracy of segment mirrors. The optical parameters and the arrangement of FDs are checked with starlight calibrations with following two methods. One is a way to use the time variation of pedestals of PMT outputs caused by moments of stars in the FOV. Starlight can be observed as high pedestal value with DC-coupling electronics of our FDs. Since positions of stars are well known, the pointing direction of the optical axis of the PMTs and the curvatures of composite mirrors can be calibrated by comparing measured and expected pedestal variations.

The other is a way to use photographs of star images on the focus plane, *i.e.*, the camera surface. The method is that taking pictures of star images on a fluorescent screen on a camera surface from the center of a mirror. Then, the pointing directions of the cameras and curvature of the mirrors are calibrated by comparing the photographs with simulated images on the camera surface. The results from these two methods are in good agreement. Therefore, we use the averaged geometry of these two methods, and the systematic uncertainty is less than 0.2 degrees.

The number of injected photons are reduced taking into account the transmissivities of the camera window and the UV filter in front of PMTs and converted to photo-electrons taking into account the quantum efficiency, the correction efficiency, and the uniformity of PMTs. Then, signals measured at FDs are finally reproduced.

In addition, background light is important for FD simulations, especially for evaluating the detection efficiency. The background light is caused by night sky background, stars and artificial light. The mean and fluctuation of the background are recorded in every 10 minutes, which corresponds to the typical passing time of a star through the field of view of a PMT.

5.2 Event reconstructions

This section explains an overview of the hybrid event reconstruction procedures [71, 72] used in this study. The hybrid reconstruction consists of four steps: PMT selection, shower geometry reconstruction, longitudinal shower profile reconstruction, and quality cuts.

In the hybrid analysis, both FD and SD data are used. The timing information in SD data is used for geometrical reconstructions. It allows significant improvement in the accuracy of the determination of shower geometries comparing with the FD monocular analysis. After the geometrical reconstruction, the longitudinal profile of the EAS is reconstructed using the FD data with precise geometry.

5.2.1 PMT selections

Before the reconstruction process, PMTs which truly detect shower signals must be identified and noise only pixels must be discarded. There are four steps of this PMT selection.

The first step of the PMT selection is done based on the strength of PMT signals. When the signal of PMTs in a triggered camera is greater than 3σ above the background level, the PMTs are selected.

Then, the PMTs selected with the first level PMT selection are used to draw a shower track on the cameras. The PMTs' positions and signal timing are spatially and temporally compared with the track, and PMTs isolated from the track are discarded with the second and third level PMT selection. At this step, the shower detector plane (SDP) is defined, which is the plane include the shower axis and the FD.

Only high significant signal PMTs are selected before this selection, however in the fourth level selection, PMTs which have lower significance of signal are also considered. Signal timings of PMTs are fitted and distances between each PMT and the SDP are calculated. Then, isolated PMTs are discarded, and PMTs which are well fitted and close to the SDP are added to the selected PMT list.

5.2.2 Geometrical reconstruction

The energy threshold of the analysis in this thesis is lower than the analysis which uses only SD data. For such low energy EASs, the number of triggered SDs is too small to

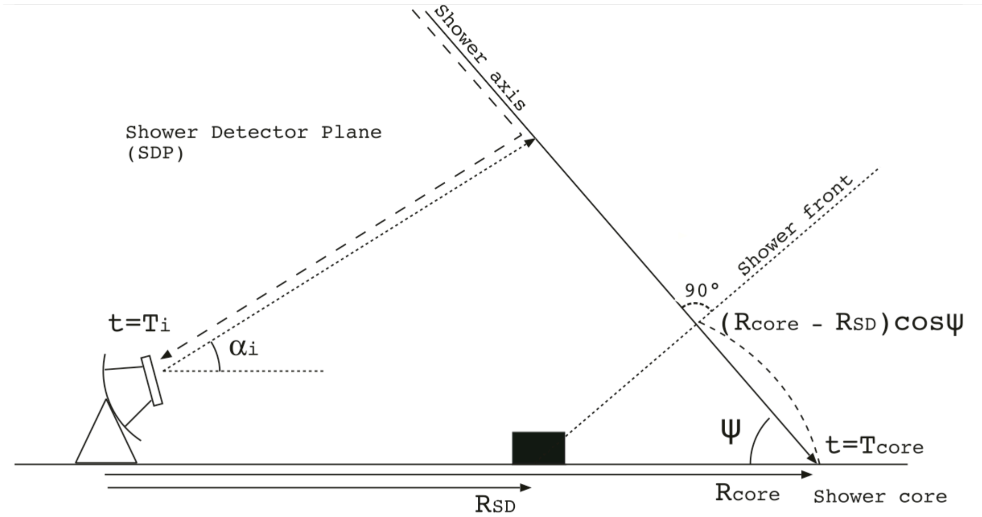

Figure 5.6: Schematic view of the parameters related to the geometrical reconstruction [71].

estimate the core position of the EAS by using only SD information. Therefore, in this hybrid analysis, the timing information of one triggered SD and FD information are used to reconstruct the shower geometry.

In the geometrical reconstruction of the monocular FD analysis, the geometry is determined taking into account both the pointing direction and the timing of hit PMTs fit to the following equation,

$$T_{\mathrm{exp},i} = T_{\mathrm{core}} + \frac{\sin\psi - \sin\alpha_i}{c\sin(\psi + \alpha_i)} R_{\mathrm{core}}, \tag{5.2.3}$$

where $T_{\mathrm{exp},i}$ and α_{i} are the expected timing and the elevation angle on the SDP for the i-th PMT, ψ is the angle between shower axis and the ground, and T_{core} is the timing when the shower hit the ground, and R_{core} is the distance between the core position of the EAS and the FD (see also Figure 5.6).

T_{core} can be expressed with the information of the SD which is the nearest to the EAS core as follows,

$$\begin{aligned} T_{\mathrm{core}} &= T'_{\mathrm{SD}} + \frac{1}{c}(R_{\mathrm{core}} - R_{\mathrm{SD}})\cos\psi, \\ T'_{\mathrm{SD}} &= T_{\mathrm{SD}} - \frac{1}{c}\{(\vec{P'}_{\mathrm{SD}} - \vec{P}_{\mathrm{SD}}) \cdot \vec{P}\}, \end{aligned} \tag{5.2.4}$$

where $\vec{P}_{\mathrm{SD}}$ is the position of the SD, $\vec{P'}_{\mathrm{SD}}$ is the projected SD position on the SDP, $\vec{P}$ is the direction of the shower axis, T_{SD} is the timing of the SD signal, T'_{SD} is the corrected timing at the projected SD position, and R_{SD} is the distance between the FD and $\vec{P'}_{\mathrm{SD}}$. Then, to determine the shower geometry, signal timings are fitted to minimize the following χ^2,

$$\chi^2 = \sum_i \frac{(T_{\mathrm{exp},i} - T_i)^2}{\sigma_{T,i}^2}, \tag{5.2.5}$$

where $\sigma_{T,i}$ is the fluctuation of the signal timing.

SDs which are used in the geometrical reconstruction are selected from the SDs within closer than 1.5 km from the core position, which is determined by weighted average point of SD signal distribution in the first calculation, and closer than 1.2 km from the line of intersection of the SDP and the ground to reduce the fake triggered SDs, which are triggered with chance incident particles. When the core position is determined by the procedures described above, then these procedures are iterated by using the calculated core position as initial value of it to get the minimum χ^2.

5.2.3 Longitudinal profile reconstruction

For the longitudinal profile reconstruction we use only FD data. Since the shower axis for each event is already known as the result of the geometrical reconstruction, the development of the EAS along the the shower axis is evaluated with the profile reconstruction process. For the profile reconstruction, the amount of fluorescence photons is important, but there are contamination from Cherenkov photons in detected signals. There are four types of photon components in detected signals, that is fluorescence photons, direct Cherenkov photons, scattered photons by atmospheric molecules and aerosols. On order to reconstruct the longitudinal profile analyzing those various photon components we use a method called *inverse Monte Carlo* (IMC) technique.

The idea of the IMC technique is that searching the best fit EAS profile for observed air showers through comparisons between the observed data and MC simulations. By using the IMC technique, processes which can not be reproduced from observed signals, such as non-uniformity of the the PMT sensitivity, can be realistically considered in the reconstruction process.

For the shower longitudinal profile calculations in the IMC we use numerical calculations based on Gaisser-Hillas function [27] instead of using full MC simulations, such as CORSIKA. In the numerical calculations the first interaction point, X_0, and the interaction length, λ, is fixed at 0 g/cm^2 and 70 g/cm^2, respectively, because these parameters are less sensitive for the energy determination. Then, the adjustable parameters in the IMC are X_{max} and N_{max}.

At the first step of the IMC process, the N_{max} is fixed to 1.0, and the X_{max} is the adjustable parameter to be optimized. With altering values substituted into X_{max} we simulate the expected number of photo-electrons for all the PMTs taking into account the detector response as the same routine described in Section 5.1.3. The optimized value for

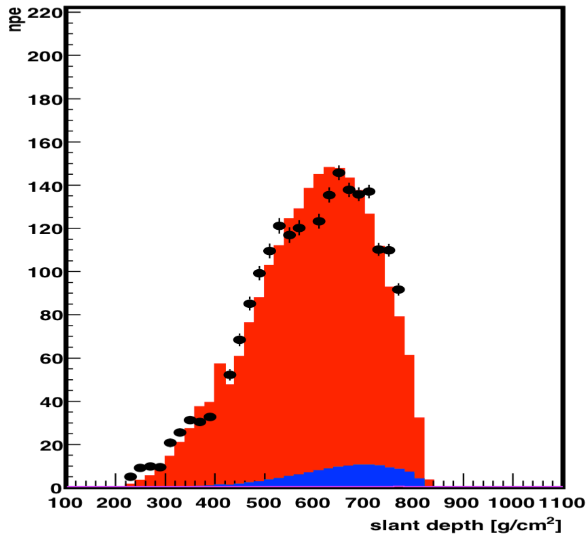

Figure 5.7: An example of the result of the longitudinal profile reconstruction with the IMC technique [71]. The horizontal axis is the slant depth along the shower axis, and the vertical axis is the number of photo-electrons observed by the FD. The black points show the observed data and the red and the blue histograms indicate the fluorescence and the scattered photon components optimally estimated by the IMC. Shower parameters of this event are estimated as follows: zenith angle is 4.0 degrees, azimuthal angle is 313.1 degrees, impact parameter (distance from the station to the shower axis) is 17.7 km, primary energy is 8.1×10^{19} eV, and the $X_{\max}$ is 756.4 g/cm^2.

$X_{\max}$ is determined by maximizing the following likelihood, L, which is calculated by

$$\begin{aligned} L &= \sum_{i}^{\mathrm{PMTs}} n_i^{\mathrm{obs}} \log \frac{n_i^{\mathrm{exp}}}{n^{\mathrm{exp,sum}}}, \\ n^{\mathrm{exp,sum}} &= \sum_{i}^{\mathrm{PMTs}} n_i^{\mathrm{exp}}, \end{aligned} \tag{5.2.6}$$

where n_i^{obs} and n_i^{exp} is the observed number of photo-electrons with i-th PMT.

After the optimized $X_{\max}$ is determined, the optimized value for $N_{\max}$ is calculated as follows,

$$N_{\max} = \frac{\sum_i^{\mathrm{PMTs}} n_i^{\mathrm{obs}}}{\sum_i^{\mathrm{PMTs}} n_i^{\mathrm{exp}}}. \tag{5.2.7}$$

Figure 5.7 shows an example of the result of the longitudinal profile reconstruction with the IMC technique.

The primary energy of the EAS is calculated by integrating the Gaisser-Hillas function with optimized parameters as a result of the profile reconstruction.

5.2.4 Quality cuts

There are contaminations of inaccurately reconstructed events even if reconstruction process are successfully finished. For example, for the event of which true $X_{\max}$ is outside of the FOV of FDs the accurate estimation for $X_{\max}$ is difficult. Therefore, we need to discard these inaccurately reconstructed events from analyzed event data set in order to avoid using these inaccurate events for further analyses. Requirements for selected events to pass this quality cut are as follows:

- The number of selected PMTs > 20
- The estimated $X_{\max}$ is inside of the field of view of the FD
- The estimated incident zenith angle < 55 degrees
- The estimated core position is inside of the SD array
- The minimum viewing angle (see text) > 20 degrees

The minimum viewing angle is the minimum angle between the shower axis and the viewing angle from the FD to the each point of shower axis within the inside of the FOV. This cut reduces events which have photon component dominated by the Cherenkov photons, because for such events, it is difficult to reconstruct the longitudinal profile of fluorescence photons with accurately.

5.3 Monte Carlo study

5.3.1 Monte Carlo data set

I prepared hybrid MC data sets for primary protons and primary photons with the procedures as described in Section 5.1. The parameters for making the MC data set are listed in Table 5.2.

Table 5.2: Parameters for making the MC data set.

Zenith angle	$0° < \theta < 60°$, uniform
Azimuthal angle	$0° < \phi < 360°$, random
Core position	within 30 km from CLF, random

It is difficult to obtain enough MC event statistics in the whole energy range, $10^{18,0} \sim 10^{20.5}$ eV, by throwing simulations with energy spectrum of E^{-3}. To overcome this situation, I made MC data with spectral index of -3.34 in the energy range from $10^{18.0}$ eV to $10^{18.5}$ eV, and with induex of -1.0 in the range above $10^{18.5}$ eV. Then, each simulated event are weighted to fit the energy spectrum to the observed energy spectrum by the SD measurement [6].

Statistics of the MC data set with each step of the quality cuts are listed in the Table 5.3.

Table 5.3: The statistics of the MC data for protons and photons. The parent CORSIKA showers are repeatedly used for the simulations (see Section 5.1.2).

The number of survived events at each step	Protons	Photons
The number of parent CORSIKA showers	6500	7280
The number of thrown MC events	$\sim 3.5 \times 10^6$	$\sim 1.4 \times 10^6$
The number of reconstructed events	119351	35634
The number of selected PMTs > 20	113907	31992
The estimated $X_{\rm max}$ is inside of the FOV	103360	20770
The estimated incident zenith angle < 55 degrees	93873	17801
The estimated core position is inside of the SD array	81752	15999
The minimum viewing angle (see text) > 20 degrees	73765	14051

5.3.2 Resolutions

The resolutions of reconstructed geometry and shower profile for the hybrid reconstruction technique are obtained from comparisons between simulated and reconstructed parameters. In order to evaluate the resolutions, the MC data set which passed the quality cuts written in Section 5.2.4 is used.

The difference of core position between simulated and reconstructed values is shown in Figure 5.8, and the resolution of the core position is 111 m. That of the open angle is shown in Figure 5.9, the resolution is 0.7°.

The resolution and energy dependence of energy estimation is shown in Figure 5.10. The energy resolution is about 9.5% with +2% systematic shift, and it has small energy dependency. The $X_{\rm max}$ resolution and energy dependency are shown in Figure 5.11. The $X_{\rm max}$ resolution is about 29 g/cm^2, and systematic shift is -14 g/cm^2. The energy dependence of the $X_{\rm max}$ reconstruction is small, and that is negligible with in the resolution. The systematic bias of $X_{\rm max}$ may be come from reconstruction procedure, thus it also affect reconstruction results of real data.

5.4 Data and Monte Carlo comparisons

We use MC simulations not only for the event reconstruction procedures, but also getting the physics results. Therefore, it is important to ensure that our MC simulations accu-

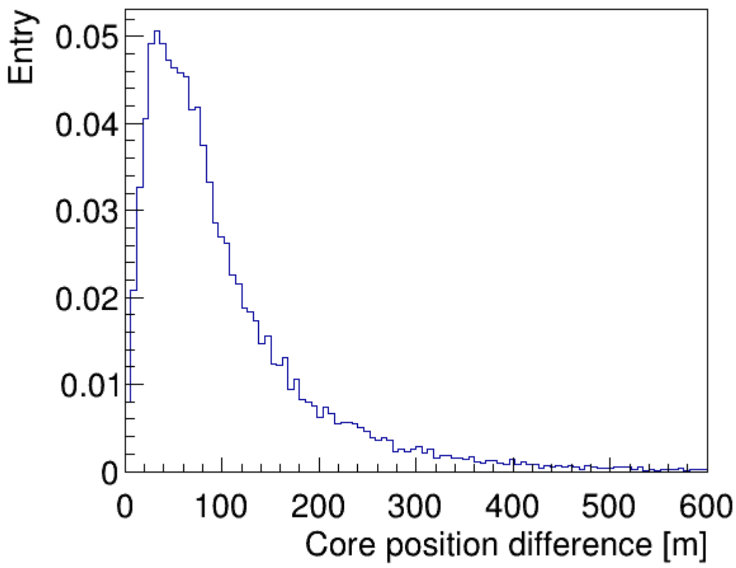

Figure 5.8: The histogram of difference between simulated and reconstructed core position. The horizontal axis is the difference, and the vertical axis is normalized entry. The resolution is calculated with region of 68%, and it is 111 m.

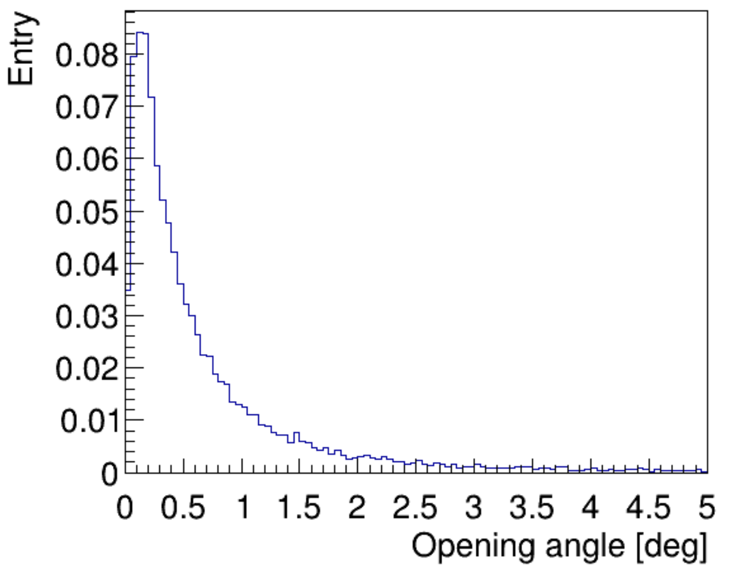

Figure 5.9: The histogram of difference between simulated and reconstructed open angle of arrival direction. The horizontal axis is the difference, and the vertical axis is normalized entry. The resolution is calculated with region of 68%, and it is 0.7°.

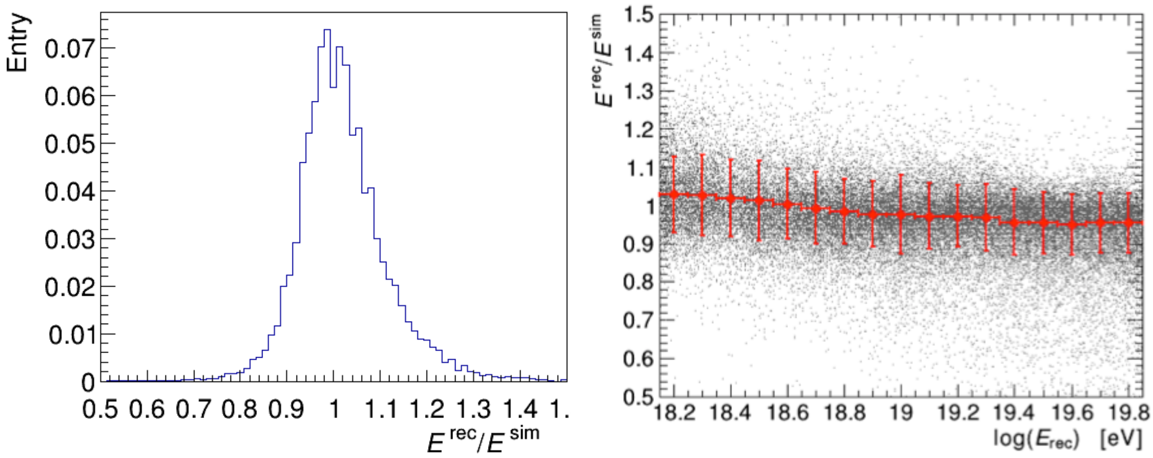

Figure 5.10: (*Left*) the histogram of energy ratio of simulated and reconstructed energy. The systematic shift of reconstructed energy is about +2% and the resolution is about 9.5%. (*Right*) the energy dependence of the energy ratio. Reconstructed energies have small energy dependence.

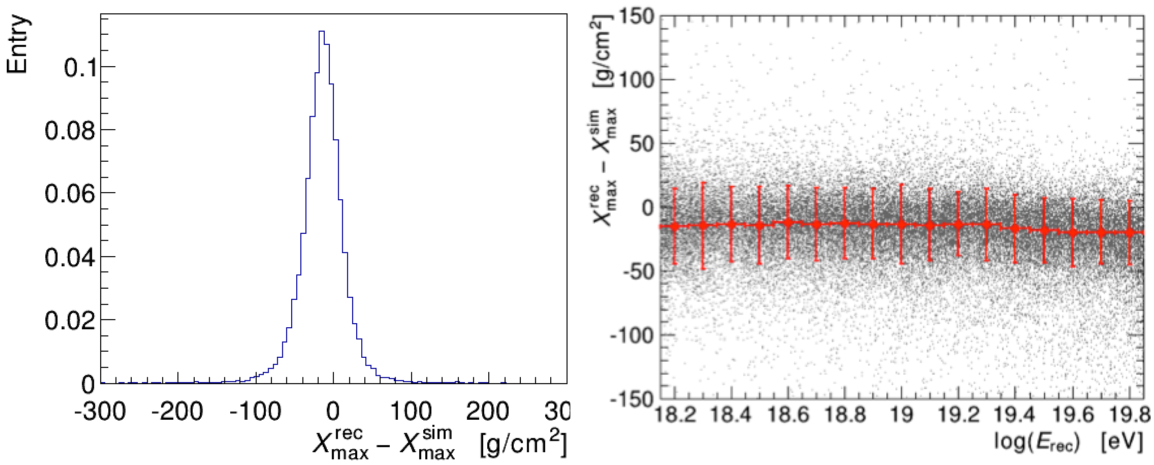

Figure 5.11: (*Left*) the histogram of difference between simulated and reconstructed $X_{\max}$. The systematic shift of reconstructed $X_{\max}$ is about -14 g/cm^2 and the resolution is about 29 g/cm^2. (*Right*) the energy dependence of the $X_{\max}$. Almost no energy dependence can be found in $X_{\max}$ reconstruction.

rately reproduce real observed data. For this purpose, in this section we compare various observable values obtained from the analysis for MC simulated and real observed data.

5.4.1 Observed data set

The TA hybrid measurement has been continued since March 2008. The period of the observed data set is from May 2008 to July 2013 to avoid unstable operation term at the early term of the hybrid measurement. In this thesis, I used the data obtained by two FD stations, BR and LR stations, and the SD array. The number of events which have energies grater than 1 EeV is 2970 after the quality cut.

5.4.2 Comparisons of observable parameters

In order to check the consistency between the observed data and MC data, comparison plots for many observable parameters are made as shown in Figure 5.12-5.19. In these figures, the black crosses show measured values of the data, and the red and the blue histograms indicate MC predicted values calculated with primary protons and primary photons, respectively. The upper figures are histograms of each parameter, and lower figures are the ratios of real data to MC data in each bin. For all the data in these figures, the quality cuts described above have been applied. The distributions of observables for proton MC are in almost good agreement with that of the observed real data.

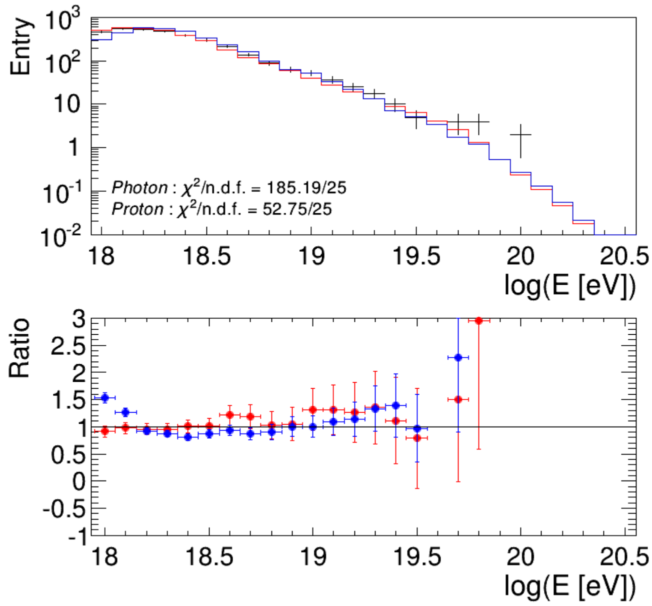

Figure 5.12: The Distributions of the number of event. Each MC events are weighted to fit the energy spectrum to the obtained energy spectrum from the SD analysis [6]. The proton spectrum is in good agreement with that of real data without energy of 10^{20} eV bin. The discrepancy is come from the choice of the bin size.

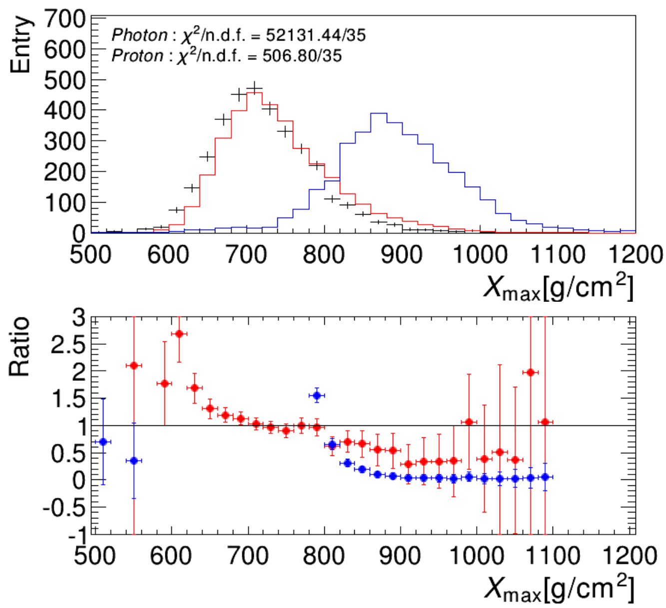

Figure 5.13: The Distributions of reconstructed $X_{\max}$. There is systematic shift between proton MC and real data distribution. The amount of shift is about 20 g/cm^2.

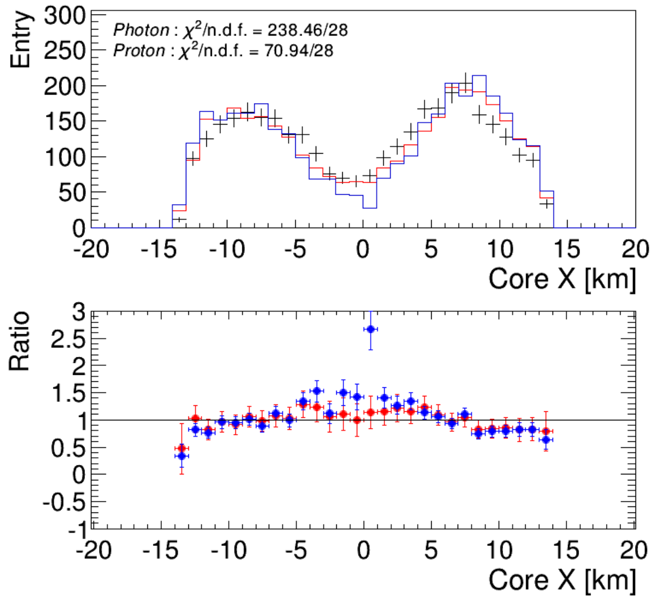

Figure 5.14: The distributions of core positions along with the x-axis from west to east direction centered at the CLF position. The MC data set distribution is in good agreement with that of the real data set.

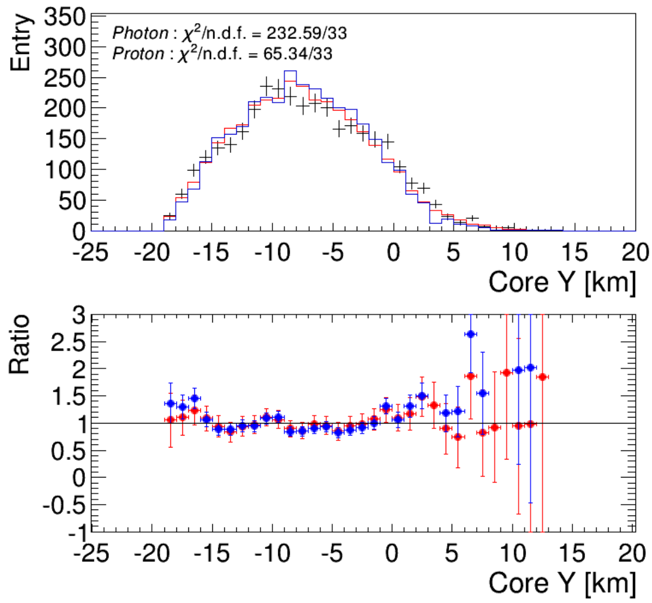

Figure 5.15: The distributions of core positions along with the y-axis from south to north direction centered at the CLF position. The MC data set distribution is in good agreement with that of the real data set.

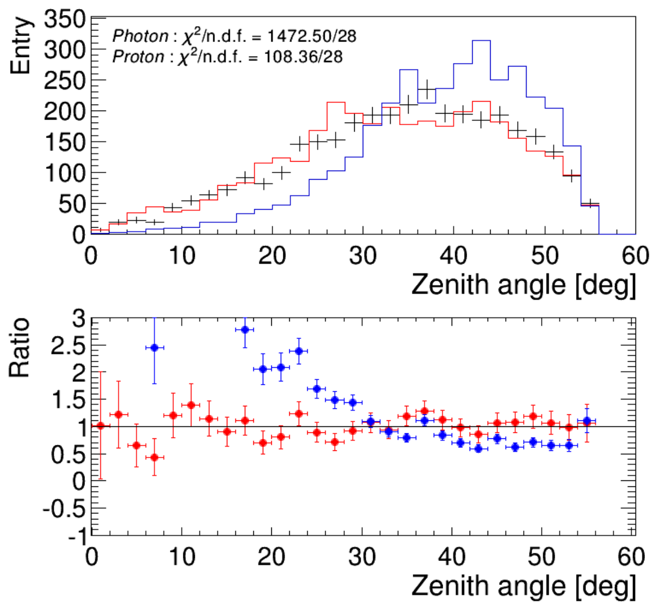

Figure 5.16: The distributions of the zenith angle of EASs. The MC data set distribution is in good agreement with that of the real data set with in statistical errors.

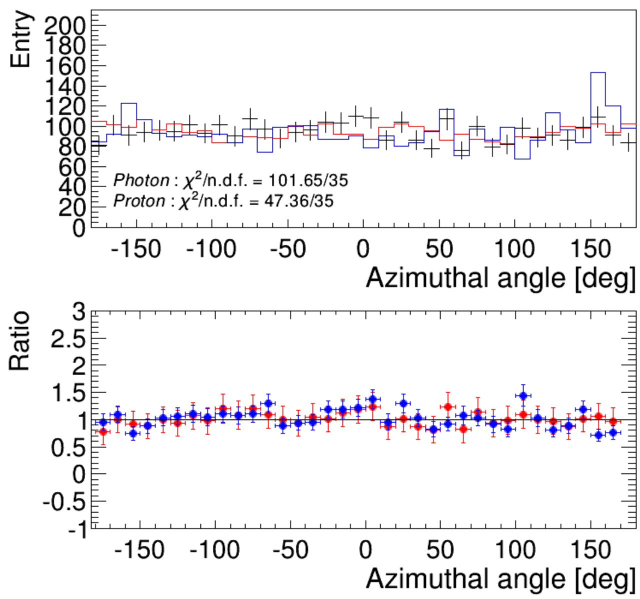

Figure 5.17: The distributions of the azimuthal angle of EASs. The MC data set distribution is in good agreement with that of the real data set.

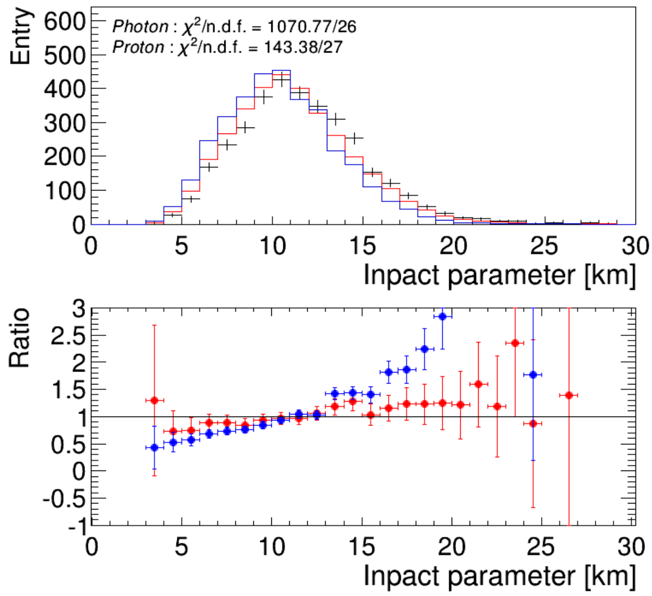

Figure 5.18: The distributions of the impact parameter of EASs. The MC data set distribution is in good agreement with that of the real data set.

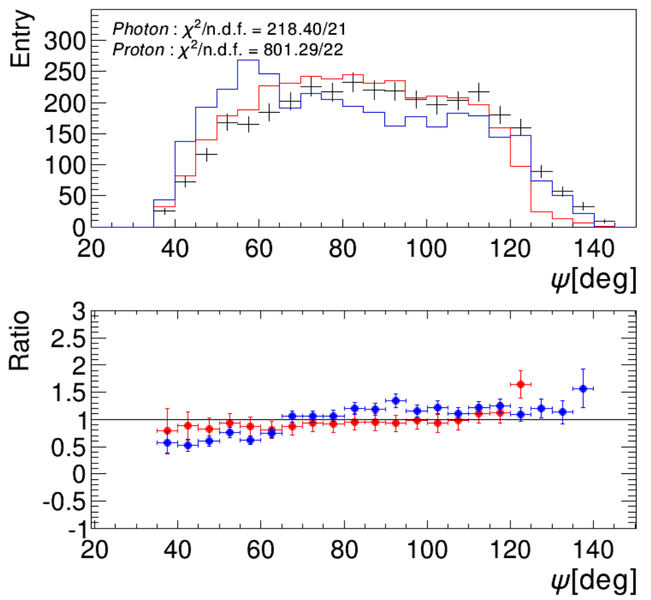

Figure 5.19: The distributions of the ψ angle, which is the angle between the shower axis and the direction from the FD station to the shower core position on the SDP (see Figure 5.6). The MC data set distribution is in good agreement with that of the real data set below 120°. Above 120°, there is systematic difference between the real data set and MC data set.

Chapter 6

Search for ultra high energy photons

In this chapter the results of the UHE photon search based on observed X_{max} are presented. First, I will describe the acceptance bias for detecting EASs induced by primary photons and a data reduction method to reduce the acceptance bias. Second, a criterion for selecting UHE photon-like events is discussed. Then, as a result I obtained photon fraction upper limits, and I discuss the results based on comparison with theoretical predictions and other experiments results.

6.1 Acceptance bias and data reduction

The averaged X_{max} of photon induced showers are larger than nucleus induced showers as discussed in Chapter 3. As discussed in Section 5.2.4 the quality cut based on the reconstructed parameters are applied in order to keep high reconstruction accuracies. One of selection rules in the quality cut requires the reconstructed X_{max} to be inside the FOV of FDs, thus deeply penetrated EASs are discarded by this criterion because X_{max} of such EASs are below the FOV of FDs. Since most of EASs of primary photons have significantly deeper X_{max} than that of primary protons at energies greater than 1 EeV, photon induced EASs are more likely to be discarded with this criterion. This effect is relatively low for inclined showers, because inclined showers pass through more atmosphere before entering the field of view of the FD. Thus, events with large X_{max} are more likely to be remained after the quality cut in inclined showers comparing with that of vertical showers.

Therefore, I applied an additional cut criterion discarding the events which have smaller reconstructed zenith angle than 20° (*photon enhance cut*), to suppress the detection efficiency for protons, and comparatively to enhance the detection efficiency for photons.

The acceptance bias is calculated comparing the survival fraction, R, for photon primaries with that for proton primaries. The fraction R is defined as the ratio of the number of remained events after reconstructions and quality cut to the number of thrown

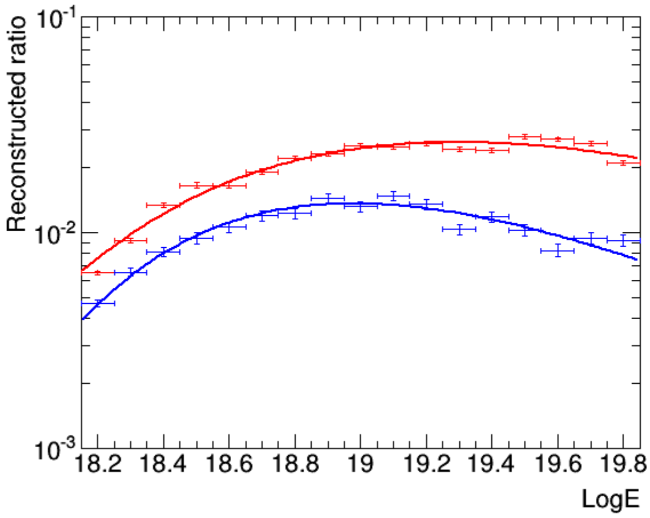

Figure 6.1: The survival fraction R. Red and blue points indicate R for protons and that for photons, respectively. The lines show the fit results with an empirical equation.

MC events, *i.e.*,

$$R = \frac{N_{\mathrm{reconstructed}}}{N_{\mathrm{thrown}}}. \tag{6.1.1}$$

Figure 6.1 shows R for proton and photon primaries.

As a result, we get the acceptance bias as the ratio of R for photons to that for protons, at several energy ranges as 0.512, 0.502, 0.482, and 0.445 at energy grater than 2, 3, 5, and 10 EeV, respectively.

6.2 Selection criterion for photon primary events

As discussed above, EASs induced by primary photons have larger X_{max} than that of protons on average. Thus, I use observed X_{max} as a key to select photon primary events. The selection criterion is determined from the MC simulations for photon primaries. I calculated the average of reconstructed X_{max} for photon MC, and adopted it for the photon selection criterion. Figure 6.2 shows the averaged X_{max} of the photon primary EASs. The fitting result of the averaged X_{max} for the photon primaries are the photon selection criterion in this work. When the reconstructed X_{max} of an event is larger than the selection criterion at the energy of the event, the event is tagged as *photon-like* event. The survival efficiencies for primary photons of this selection criterion are 0.498, 0.497, 0.532, and 0.515 at energies greater than 2, 3, 5, and 10 EeV.

The longitudinal development of simulated EASs of primary nuclei depend on high energy hadronic interaction models. On the other hand, the interaction model are less

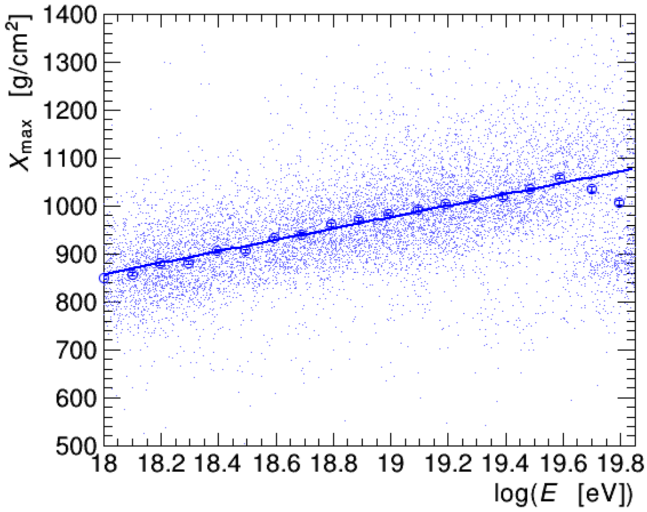

Figure 6.2: The blue dots are X_{max} of each photon-induced EAS. The blue open circles show the averaged X_{max} at each energy bin, the size of each bin is 0.1 in logarithm of energy. The lines show the fitting results of photon averaged X_{max}. There is a bend at $10^{19.6}$ eV for averaged X_{max} of photons due to the preshower effect.

effective on EASs , of primary photons, because EASs induced by photons are almost purely electromagnetic cascades. In order to confirm this model dependence, averaged X_{max} for photons with QGSJETII–03, EPOS–LHC are simulated and compared each other. Figure 6.3 shows the averaged X_{max} with QGSJETII–03 and with EPOS–LHC. The maximum discrepancy of the averaged X_{max} between these two models are less than 10 g/cm^2. The maximum discrepancy is smaller than the X_{max} resolution of the hybrid analysis, thus, the model dependency is negligible for setting the photon selection criterion.

In Figure 6.4, the selection criterion and reconstructed X_{max} of proton primary EASs are plotted. In order to estimate the proton contamination with this photon selection criterion, the photon selection is applied to the proton MC data set. Then, 3.3%, 2.7%, 1.8%, and 0.9% protons are tagged as photon-like events. Figure 6.5 shows distributions of reconstructed X_{max} of protons and photons at several energy ranges.

6.3 Data analysis

The observation period for data used in this analysis is the same as shown in Section 5.4. The observed and the MC data are reconstructed and applied the quality cut described in Section 5.2.4, and the photon enhance cut described in Section 6.1.

Figure 6.6 shows X_{max} of observed events and the photon-like event selection criterion. The events which have larger X_{max} are selected as photon-like events. The numbers of the

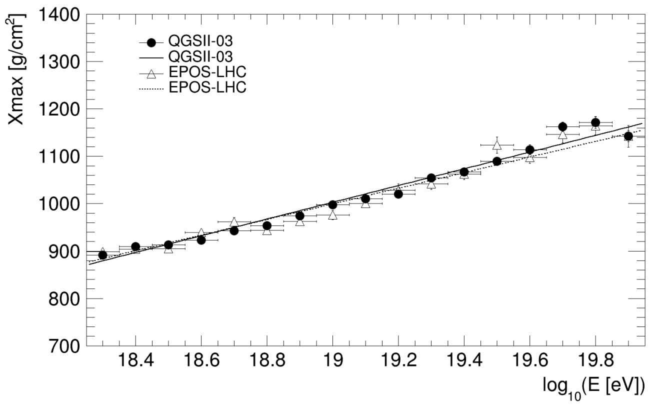

Figure 6.3: The interaction model dependence for $X_{\max}$ of primary photon showers. The filled circles indicates the averaged $X_{\max}$ for each energy range with QGSJETII–03, and the solid line is fitted to the filled circles. The open circles and dashed line are calculated with EPOS–LHC. These values are calculated with CORSIKA.

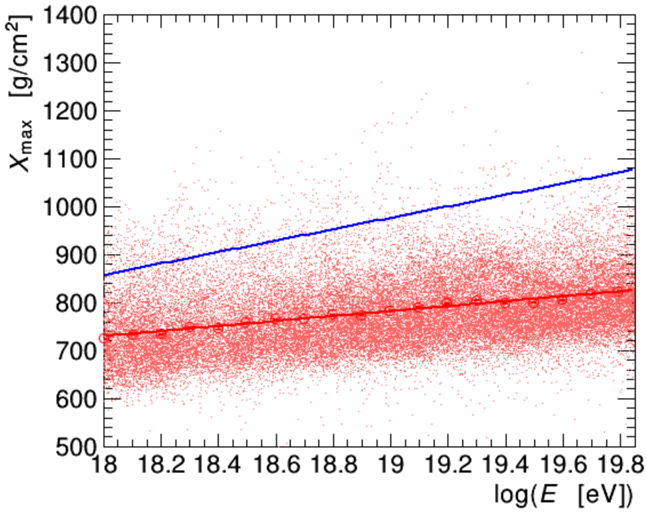

Figure 6.4: The red dots are reconstructed $X_{\max}$ for MC simulated events of primary protons, and blue line is the selection criterion determined by Figure 6.2. Open circles show the averaged $X_{\max}$ of protons at each energy bin, the size of each bin is 0.1 in logarithm of energy. We can find the contamination from protons to the photon selection criterion.

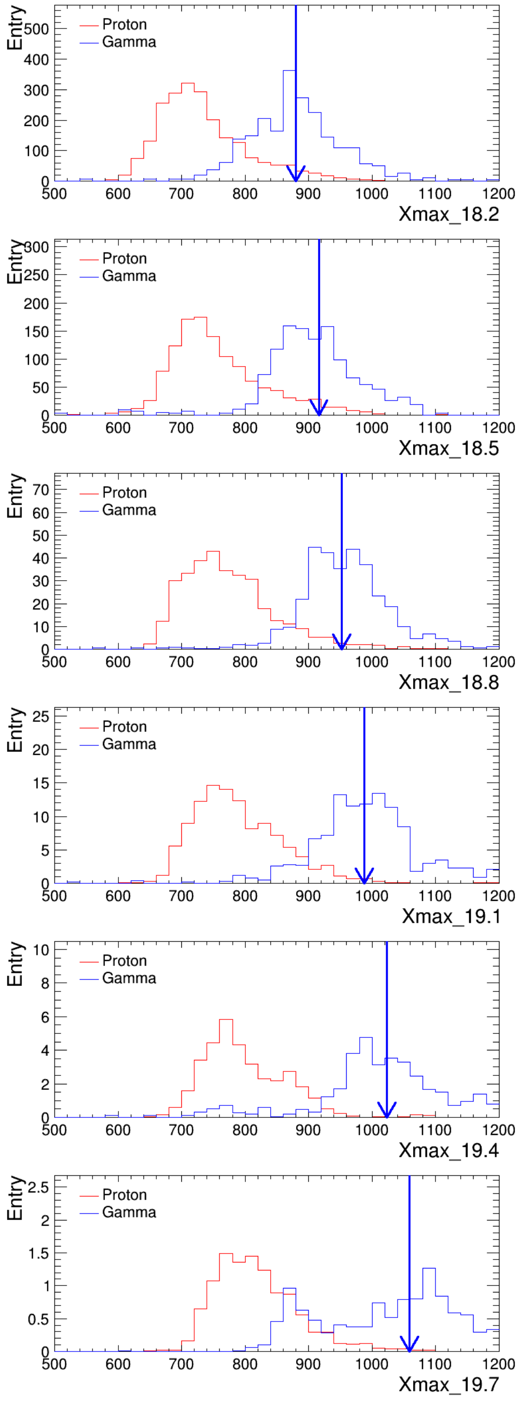

Figure 6.5: X_{max} histograms for several energy ranges in $10^{18.2}$ eV, $10^{18.5}$ eV, $10^{18.8}$ eV, $10^{19.1}$ eV, $10^{19.4}$ eV, and $10^{19.7}$ eV from upper to lower figures, respectively. The red histograms and the blue histograms indicate protons and photons, respectively. The blue arrow in each figure shows the photon selection criterion at each energy range.

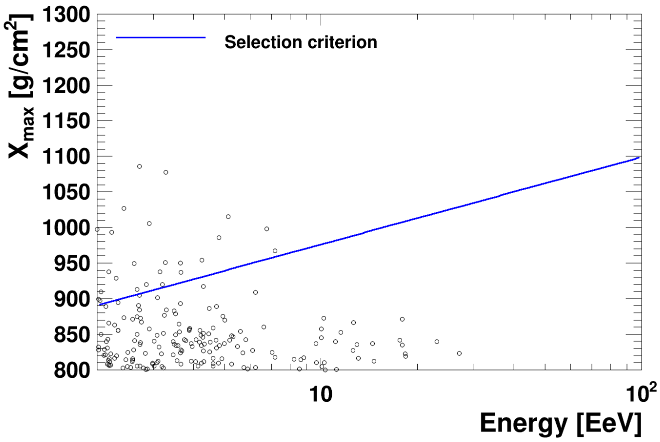

Figure 6.6: Reconstructed X_{max} of observed events and the selection criterion. The circles show data points and the line is the selection criterion described in Section 6.2. The observed data are passed through the quality cut and the photon enhance cut.

photon-like events are 24, 11, 3, and 0 in the energy ranges with energies greater than 2, 3, 5, and 10 EeV, respectively. The numbers of all events are 1396, 773, 229, and 121 in the same energy ranges.

Each of the photon-like event selected as above can not be distinguished whether real photon or not, because of the proton contamination. It is expected that some protons are able to have deeper X_{max} than the selection criterion due to large fluctuation of a longitudinal development. Thus, we compared the number of photon-like events with expected number of photon-like event from deeply penetrated proton EASs. In order to estimate the proton contamination, the same selection is applied to proton MC. As a result, the number of photon-like events with proton MC are 46, 21, 6, and 1 with energy ranges grater than 2, 3, 5, and 10 EeV, respectively. Therefore, the result from real data analysis is not exceed the expectation from proton contamination, even though the shift of X_{max} between real data and proton MC (see Figure 5.13) is considered.

6.4 Upper limits of the photon fraction

We can not exclude all of the protons from the photon-like events, the upper limit of the photon fraction which is the fraction of photon flux to all particle flux is calculated from observed data. In order to obtain a conservative upper limit, the photon-like events are assumed to be truly induced by primary photons. This is because the X_{max} distribution of protons highly depend on which the high energy hadronic interaction model is used, thus we can not estimate realistic contamination from protons without systematic uncertainty.

The upper limit of the number of photon-like events using the Poisson distribution is calculated with assuming no background, *i.e.*, all the photon-like events are true photons. Poisson upper limit of the number of photon-like events with 95% confidence level is obtained as 33.8, 18.2, 7.8, and 3.0 in the range with energies above 2, 3, 5, and 10 EeV. As discussed above the photon selection of this analysis discard not only nuclei but also photons, thus the selection efficiency should be taken into account for calculating the upper limit. As a results we obtained 95% confidence level upper limit of the number of photon-like events, $n_\gamma|_{95\%}$, as 67.8, 36.6, 14.6, and 5.8 in the range with energies above 2, 3, 5, and 10 EeV.

Finally, we obtained the upper limit of photon fraction with 95% confidence level, $F_\gamma|_{95\%}$, from following relation,

$$F_\gamma|_{95\%} = \frac{I_\gamma|_{95\%}}{I_\gamma|_{95\%} + I_\mathrm{p}} = \frac{n_\gamma|_{95\%}}{n_\gamma|_{95\%} + (n_\mathrm{obs} - n_\gamma|_{95\%})A_\gamma/A_\mathrm{p}}, \tag{6.4.2}$$

where I_γ and I_p are the fluxes of photons and protons, n_obs indicates the number of observed events, n_γ is the number of the photon-like events, A_γ and A_p are the apertures of the experiment for primary photons and protons, respectively, and the notation of "95%" means 95% upper limit. The ratio of the apertures, A_γ/A_p, is substituted from the acceptance ratio derived in Section 6.1. Then, the upper limit of the photon fraction with 95% confidence level are obtained as 9.1%, 9.0%, 8.5%, and 10.2% in energies above 2, 3, 5, and 10 EeV, respectively. The results of the calculations are shown on Table 6.1. Figure 6.7 is the photon fraction upper limit comparing with other experimental results and predictions from several models. In this figure, the result from the same processes of analysis as this work with monocular data set, which are reconstructed with monocular method [73], is also showed.

6.5 Systematic error from energy uncertainty

There are systematic uncertainties on energy determination with the hybrid analysis. Table 6.2 shows a list of sources of the systematic uncertainties [71]. It consists of uncertainties of the detector calibration, the atmospheric attenuation, the fluorescence yield, and the reconstruction error. The total systematic uncertainty on energy determination is calculated with the quadratic sum of these uncertainties, and that is 21%.

In order to estimate the systematic uncertainty on the photon fraction upper limits, the upper limits are recalculated with shifting the energy scales with −42%, −21%, +21%, and +42%. Table 6.3 shows the results of the photon fraction upper limits calculated with shifting energy scales. Thus, I adopted the worst upper limits in each energy range 9.4%, 9.0%, 9.8%, and 26.6% in energies above 2, 3, 5, and 10 EeV.

Figure 6.8 shows the results of the photon fraction after the evaluation of the systematic uncertainty.

Table 6.1: The results of the photon fraction upper limits with 95% confidence level. See text for details.

	> 2 EeV	> 3 EeV	> 5 EeV	> 10 EeV
The number of photon-like events, n_γ	24	11	3	0
Poisson fluctuation with 95% c.l.	33.8	18.2	7.8	3.0
Photon selection efficiency	0.498	0.497	0.532	0.515
Upper limit of the number of photon-like events with 95% c.l. $n_\gamma\|_{95\%}$	67.8	36.6	14.6	5.8
Acceptance ratio, A_γ/A_p	0.512	0.502	0.482	0.445
The number of all data, n_obs	1396	773	339	121
The upper limit of the photon fraction with 95% c.l., $F_\gamma\|_{95\%}$ (%)	9.1	9.0	8.5	10.2

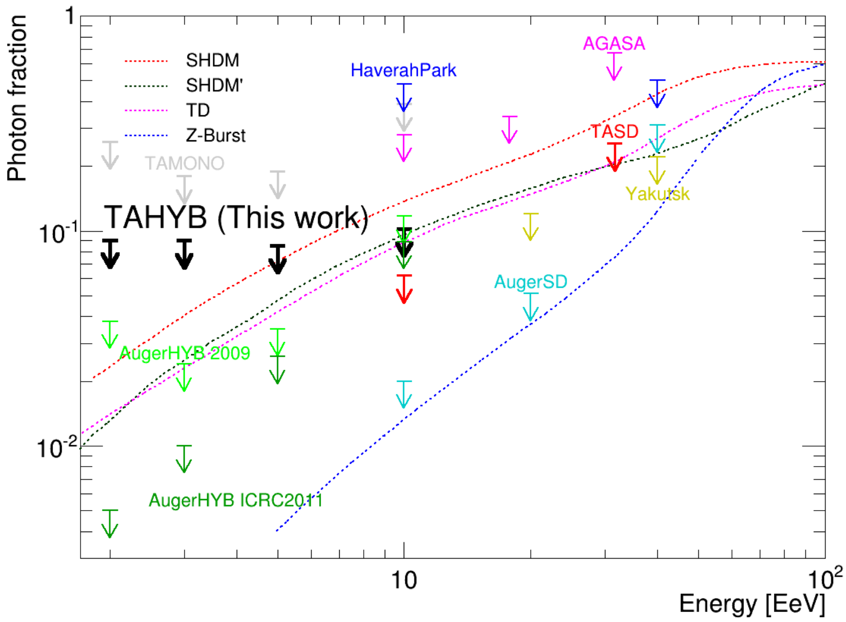

Figure 6.7: The photon fraction upper limits. Black arrows show the results of upper limits from this work. The other arrows show other experimental results: gray is the TA mono analysis result, red is the TA SD analysis result [74], light green is the Auger hybrid result presented in 2009 [75], green is the Auger hybrid result presented in 2011 [76], light blue is the Auger SD result [77], blue is the Haverah Park [78, 79], yellow is the Yakutsk [80, 81], and pink is the AGASA result [82, 83]. The lines show the predictions from top-down models (see [84–86])

Table 6.2: The systematic uncertainties on energy determination [71].

Item	Uncertainty (%)	Contributions
Detector sensitivity	10	PMT(8%), mirror (4%), aging (3%), filter (1%)
Atmospheric collection	11	aerosol (10%), Rayleigh (5%)
Fluorescence yield	11	model (10%), humidity (4%), atmosphere (3%)
Reconstruction	10	model (9%), missing energy (5%)
Total	21	

Table 6.3: The photon fraction upper limits calculated with shifting energy scales.

		> 2 EeV	> 3 EeV	> 5 EeV	> 10 EeV
−42%	# of photon-like events	8	2	0	0
	# of data	620	315	157	42
	95% u.l. (%)	8.7	7.7	7.2	26.6
−21%	# of photon-like events	17	5	2	0
	# of data	1015	535	237	79
	95% u.l. (%)	9.4	7.6	9.8	15.2
Original	# of photon-like events	24	11	3	0
	# of data	1396	773	339	121
	95% u.l. (%)	9.1	9.0	8.5	10.2
+21%	# of photon-like events	23	12	4	0
	# of data	1758	1041	464	165
	95% u.l. (%)	7.0	7.2	7.4	7.6
+42%	# of photon-like events	26	15	5	0
	# of data	2073	1300	600	200
	95% u.l. (%)	6.6	6.9	6.6	6.3

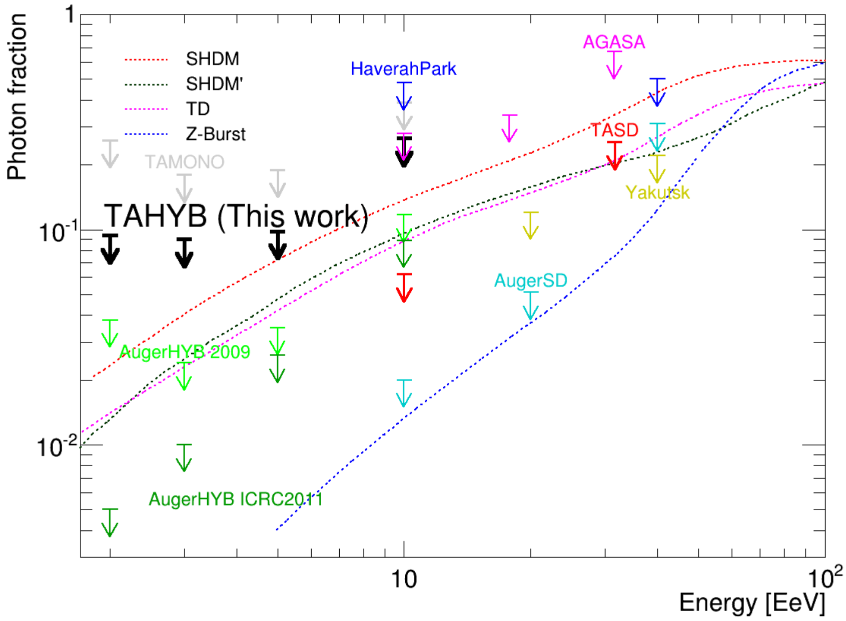

Figure 6.8: The photon fraction upper limits derived from the worst case of upper limits with shifting energy scale calculations. Notation in this figure is the same as Figure 6.7.

Chapter 7

Discussion

The studies for the nature of extensive air showers induced by primary photons and the observational results of searching for UHE photons using X_{max} with hybrid reconstruction technique are presented in this thesis. This is the first result which measured by the hybrid detection technique in the northern hemisphere.

This analysis is insensitive to the hadronic interaction models, because the photon primary EASs consist of almost purely electromagnetic cascade, and the effect on X_{max} by the hadronic interaction model used in the analysis is suppressed.

As a result of the photon fraction upper limits without systematic uncertainty of energy, one of the SHDM models is constrained at energy range above 10 EeV. When including the energy systematic uncertainty, the predicted photon fractions with top-down scenarios are not constrained. However, in consideration of combination with the TA surface detector result, super heavy dark matter models and topological defect model of the UHECR generation are constrained with 95% confidence level, and Z-burst model are survived with these upper limits in the norther hemisphere. It is important that independent search of UHE photons in the northern and the southern hemisphere, because UHE photons can be expected to be anisotropically observed since sources or generation points of UHE photons are limited to near from the Earth due to their mean free path, and also they are not deflected by the magnetic fields in the universe. Thus, the result complements other results in the southern hemisphere, such as PAO results. In addition, the uncertainties on other analyses caused by contamination of photon primary EASs, such as composition analysis using average of the X_{max}, are limited by this result.

If we get enough statistics of UHECR events (10 times) and there is no photon in the data set, we would be able to achieve a few percent upper limit at energy range above 10 EeV (Figure 7.1), and almost all top-down scenarios, except Z-burst model, would be excluded. In order to constrain the predicted photon fraction with GZK photons, however, it is necessary that improving the analysis method.

In future analysis, we will use information of secondary particles at the ground, which are derived as SD observable, and then it is expected that the discrimination power of photons from nuclei is improved, and a photon likeness of each event can be estimated.

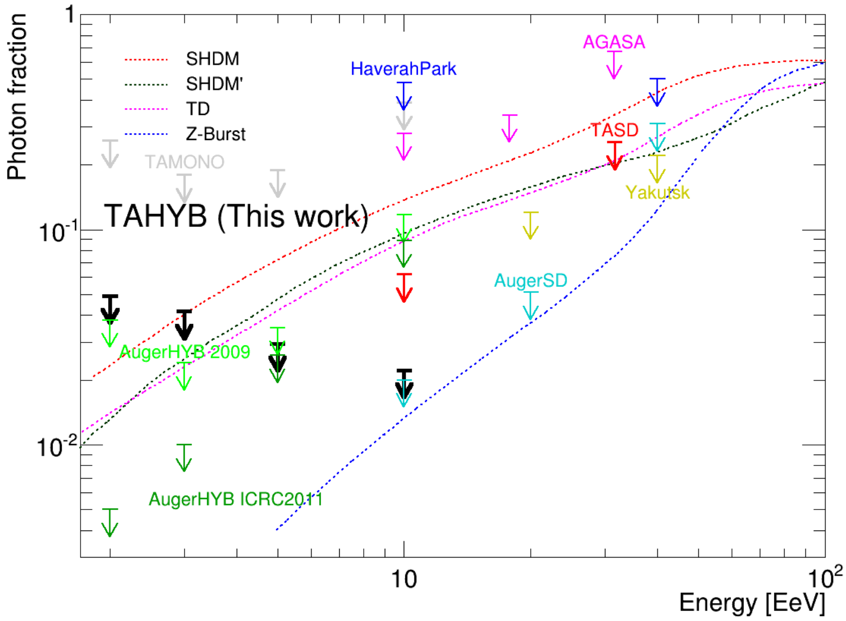

Figure 7.1: The photon fraction upper limits with enough (10 times) statistics. Notation in this figure is the same as Figure 6.7. Fraction upper limits at lower energies are higher than that of 10 EeV, because separation of average X_{max} between protons and photons is worse at lower energy ranges.

We are now constructing the muon sensitive and countable detectors in the TA experiment, using segmented plastic scintillators, and lead as an absorber for electromagnetic component. The information of muonic component in EASs are important to measure the chemical composition of UHECRs, especially in the photon search because primary photon EASs are include less muonic component. Then, the correlation analysis using photon candidates will be available in future analysis, such as correlation between arrival timings of photon candidates and timings of high energy phenomena in the universe. If UHECRs are generated by transient phenomena, such as GRB, UHE photons and neutrinos can be simultaneously detected with other optical experiment. The simultaneous detection can be a strong clue to discover sources and to reveal the nature of UHECRs.

In order to detect UHE photons, composition sensitive measurement is very important, such as using the fluorescence detection technique, and also the statistics are important to achieve more significant results.

Chapter 8

Summary and conclusion

The work in this thesis is focused on studying ultra high energy photons based on the observations with the hybrid air shower detector, to reveal the nature of ultra high energy cosmic ray origins.

An overview of recent progress in cosmic ray studies, especially focused on UHECR physics, is given in Chapter 2. There are a lot of progress in the studies of UHECR physics, however, the origins of UHECRs are still unknown. Since, the flux of cosmic rays has steep power law index, it is difficult to observe sufficient number of events at UHECR regions to reveal the origins of UHECRs. Furthermore, the magnetic deflection also makes it difficult because almost all the UHECRs are charged particles. Therefore we need to attempt to other approaches for discovering UHECR origins.

Many of models of UHECR sources and propagation mechanisms predict the existence of UHE photons. I reviewed these models in Chapter 3. In the top-down scenarios of UHECR origins, relatively higher fraction of UHE photons to charged hadrons is expected than that of the bottom-up scenarios. Thus, we can test these scenarios with measuring photon fraction in observed UHECRs.

In order to distinguish UHE photons from UHECRs, the maximum point of the longitudinal development of EASs, $X_{\max}$, is a powerful discriminator and one of the composition sensitive parameter. The averaged $X_{\max}$ for primary photons is significantly larger than that of nuclei as it is shown in Figure 3.3.

TA is the largest hybrid detector in the northern hemisphere, which consists of 507 surface detectors with approximately 680 km^2 area, and the three fluorescence detectors, which viewing over the SD array. The TA experiment continues to the full operation since May 2008, The TA hybrid detector observes the longitudinal development of EASs with fluorescence detectors and detects EAS particles at the ground with the surface detectors. By using both of the data obtained from the SDs and from the FDs the geometry and the primary energy of EASs are precisely estimated with the hybrid analysis, and also the $X_{\max}$ is precisely determined from the longitudinal development. Since $X_{\max}$ is the composition sensitive parameter, the TA hybrid detector is suitable for searching UHE photons from observed UHECRs. The hybrid data set simultaneously observed with the

700 km^2 surface detector array and with BR and LR fluorescence detector stations are used in this study searching UHE primary photons.

The data period is include the period from March 2008 to July 2013, and the quality cut and photon enhance cut requirements (see Section 5.2.4 and 6.1) are applied to the data.

The selection criterion to distinguish primary photons from primary nuclei used in this study is determined through MC simulation study of air shower development and detector response. We use de facto standard simulation package called *CORSIKA* to simulate the longitudinal development of EASs, and *GEANT4* package is used to simulate the surface detector response. The response of the fluorescence detectors are simulated with the software package developed by the TA collaboration. Finally, the average values of reconstructed X_{max} for MC simulated primary photon showers are adopted as the photon selection criteria in this study.

The result of the photon selection we obtain 24, 11, 3, and 0 events as the *photon-like* events in the energy ranges with energies greater than 2, 3, 5, and 10 EeV, respectively. Each of the photon-like event can not be distinguished whether real photon or not, because of the proton contamination. It is expected that X_{max} of proton primaries can be larger than the selection criterion due to large fluctuation of a longitudinal development. We can not exclude all of the protons by using only X_{max} information, thus the upper limits of the photon fractions are derived from the numbers of photon-like events.

The upper limits are obtained from the data with taking into account the detection biases for EASs by protons and by photons, and the selection efficiencies for the photon selection. The systematic uncertainty on the photon fraction upper limits arising from the uncertainty of energy determination are also considered. Finally, the upper limits of photon fractions with 95% confidence level are obtained as 9.4%, 9.0%, 9.8%, and 26.6% for the range of energies greater than 2, 3, 5, and 10 EeV, respectively. These upper limits are the first result, which are measured with hybrid detectors technique in the northern hemisphere, and these upper limits also ensure that the uncertainties in other analyses due to photon contamination, such as primary composition analysis, are reasonably small.

In conclusion, as a result of the upper limits the predicted photon fraction with top-down models which considered in this thesis are not constrained, but in consideration of combination with the TA surface detector result, super heavy dark matter models and topological defect model of the UHECR generation are constrained with 95% confidence level, and Z-Burst model are survived with these upper limits in the norther hemisphere.

In near future, we will update the analysis method by adding the information of secondary particles at the ground, which are derived as SD observable, then a photon likeness of each event will be available. In addition, the directions and arrival timings of photon candidates are used in future analysis.

References

[1] S. P. Swordy, *Space Science Reviews*, **99**, pp. 85–94, 2001.

[2] J. Blümer, R. Engel, and J. R. Hörandel, *Progress in Particle and Nuclear Physics*, **63**, pp. 293–338, 2009.

[3] T. Antoni *et al.*, *Astroparticle Physics*, **24**, pp. 1–25, 2005.

[4] K. Greisen, *Physical Review Letters*, **16**, pp. 748–750, 1966.

[5] G. T. Zatsepin and V. A. Kuz'min, *JETP Letters*, **4**, pp. 70–80, 1966.

[6] T. Abu-Zayyad *et al.*, *The Astrophysical Journal Letters*, **768**, L1, 2013.

[7] J. Abraham *et al.*, *Physical Review Letters*, **101**, 061101, 2008.

[8] J. A. Simpson, *Annual Review of Nuclear and Particle Science*, **33**, pp. 323–381, 1983.

[9] E. Fermi, *Physical Review*, **75**, 8, pp. 1169–1174, 1949.

[10] E. Fermi, *The Astrophysical Journal*, **119**, 1, 1954.

[11] T. K. Gaisser, *Cosmic Rays and Particle Physics*, Cambridge University Press, 1990.

[12] L. Drury, *Reports on Progress in Physics*, **46**, pp. 973–1027, 1983.

[13] P. O. Lagage and C. J. Cesarsky, *Astronomy and Astrophysics*, **118**, pp. 223–228, 1983.

[14] T. Stanev, *High Energy Cosmic Rays*, Praxis Publishing Ltd., 2004.

[15] S. Yoshida and M. Teshima, *Progress of Theoretical Physics*, **89**, 4, pp. 833–845, 1993.

[16] J. L. Puget *et al.*, *The Astrophysical Journal*, **205**, pp. 638–654, 1976.

[17] T. Yamamoto *et al.*, *Astroparticle Physics*, **20**, pp. 405–412, 2004.

[18] D. Kuempel, *arXiv*:1409.3129.

[19] J. W. Cronin *et al.*, *Nuclear Physics B (Proceedings Supplements)*, **138**, pp. 465–491, 2005.

[20] E. Waxman and J. Miralda-Escudé, *The Astrophysical Journal Letters*, **472**, pp. L89–L92, 1996.

[21] A. M. Hillas, *Annual Review of Astronomy and Astrophysics*, **22**, pp. 425–444, 1984.

[22] M. B. Hindmarsh and T. W. B. Kibble, *Reports on Progress in Physics*, **58**, p. 477, 1984.

[23] C. T. Hill, *Nuclear Physics B*, **224**, pp. 469–490, 1983.

[24] T. J. Weiler, *Astroparticle Physics*, **11**, pp. 303–316, 1999.

[25] M. Birkel and S. Sarkar, *Astroparticle Physics*, **9**, pp. 297–309, 1998.

[26] W. Heitler, *The quantum theory of radiation*, 3rd edition, Clarendon Press, 1954.

[27] T. K. Gaisser and A. M. Hillas, *Proceedings of 15th International Cosmic Ray Conference*, **8**, pp. 353–357, 1977.

[28] K. Kamata and J. Nishimura, *Progress of Theoretical Physics Supplements*, **6**, pp. 93–151, 1958.

[29] S. Yoshida *et al.*, *Journal of Physics G: Nuclear and Particle Physics*, **20**, pp. 651–664, 1994.

[30] F. Kakimoto *et al.*, *Nuclear Instruments and Methods in Physics Research A*, **372**, pp. 527–533, 1996.

[31] R. Abbasi *et al.*, *Astroparticle Physics*, **29**, pp. 77–86, 2008.

[32] J. Linsley, *Physical Review Letters*, **10**, pp. 146–148,1963.

[33] M. Lawrence *et al.*, *Journal of Physics G*, **17**, pp.733–757, 1991.

[34] V. Egorova *et al.*, *Nuclear Physics B*, **136**, pp. 3–11, 2004.

[35] D. Bird *et al.*, *The Astrophysical Journal*, **240**, pp. 410–428, 1985.

[36] M. Takeda *et al.*, *Physical Review Letters*, **81**, pp. 1163–1166, 1998.

[37] R. Abbasi *et al.*, *Astroparticle Physics*, **32**, pp. 53–60, 2009.

[38] R. Abbasi *et al.*, *Physical Review Letters*, **100**, 101101, 2008.

[39] The Telescope Array collaboration and the Pierre Auger collaboration *et al.*, *arXiv*:1310.0647

[40] R. Abbasi *et al.*, *Astroparticle Physics*, **64**, pp. 49–62, 2015.

[41] J. Abreu *et al.*, *Proceedings of 32nd International Cosmic Ray Conference*, 2011. *arXiv*:1107.4804v1

[42] The Pierre Auger Collaboration, *Science*, **318**, pp. 938–943, 2007.

[43] C. Macolino *et al.*, *Journal of Physics: Conference Series*, **375**, 052002, 2012.

[44] T. Abu-Zayyad *et al.*, *The Astrophysical Journal*, **777**, 88, 2013.

[45] R. Abbasi *et al.*, *The Astrophysical Journal Letters*, **790**, L21, 2014.

[46] A. Aab *et al.*, *The Astrophysical Journal*, **794**, 172, 2014.

[47] M. Risse and P. Homola, *Modern Physics Letters A*, **22**, pp. 749–766, 2007.

[48] G. B. Gelmini, O. E. Kalashev, and D. V. Semikoz, arXiv:astro-ph/0506128.

[49] G. B. Gelmini, O. E. Kalashev, and D. V. Semikoz, *Journal of Experimental and Theoretical Physics*, **106**, pp. 1061–1082, 2008.

[50] T. Erber, *Review of Modern Physics*, **38**, pp. 626–659, 1966.

[51] L. D. Landau and I. Y. Pomeranchuk, *The Collected Papers of L. D. Landau*, Pergamon, 1965.

[52] A. N. Cillis *et al.*, *Physical Review D*, **59**, 113012, 1999.

[53] S. R. Klein *, Radiation Physics and Chemistory*, **75**, pp. 696–711, 2006.

[54] H. P. Vankov *et al.*, *Physical Review D*, **67**, 043002, 2003.

[55] T. Abu-Zayyad *et al.*, *Nuclear Instruments and Methods in Physics Research A*, **676**, pp. 54–65, 2012.

[56] T. Abu-Zayyad *et al.*, *Nuclear Instruments and Methods in Physics Research A*, **689**, pp. 87–97, 2012.

[57] S. Kawana *et al.*, *Nuclear Instruments and Methods in Physics Research A*, **681**, pp. 68–77, 2012.

[58] Masaaki Kobayashi, Takao Shinkawa, Takahiro Sato, *Nuclear Instruments and Methods in Physics Research A*, **337**, pp. 355–361, 1994.

[59] H. Tokuno *et al.*, *Nuclear Instruments and Methods in Physics Research A*, **601**, pp. 364–371, 2009.

[60] Y. Tameda *et al.*, *Nuclear Instruments and Methods in Physics Research A*, **609**, pp. 227–234, 2009.

[61] T. Tomida *et al.*, *Nuclear Instruments and Methods in Physics Research A*, **654**, pp. 653–660, 2011.

[62] M. Chikawa *et al.*, "Cloud Monitoring with an Infra-Red Camera for the Telescope Array Experiment", *Proceedings of 31st International Cosmic Ray Conference*, 2009.

[63] D. Heck *et al.*, *CORSIKA: A Monte Carlo Code to Simulate Extensive Air Showers*, Forschungszentrum Karlsruhe Report FZKA 6019, 1998.

[64] B. T. Stokes *et al.*, *Astroparticle Physics*, **35**, pp. 759–766, 2012.

[65] B. T. Stokes *et al.*, "Using CORSIKA to quantify Telescope Array surface detector", *Proceedings of 31st International Cosmic Ray Conference*, 2009.

[66] J. Alcaraz *et al.*, *Physics Letters B*, **490**, pp. 27–35, 2000.

[67] J. Alcaraz *et al.*, *Physics Letters B*, **494**, pp. 193–202, 2000.

[68] T. Nonaka *et al.*, "Performance of TA Surface Array", *Proceedings of 31st International Cosmic Ray Conference*, 2009.

[69] A. Taketa *et al.*, "The trigger and DAQ system of the surface detector array of the Telescope Array experiment", *Proceedings of 31st International Cosmic Ray Conference*, 2009.

[70] *NOAA/ESRL Radiosonde Database*. http://www-frd.fsl.noaa.gov/mab/raob/

[71] T. Abu-Zayyad *et al.*, *Astroparticle Physics*, **61**, pp. 93–101, 2015.

[72] D. Ikeda, "Hybrid analysis of ultra-high energy cosmic rays observed with the Telescope Array", PhD thesis, University of Tokyo, 2009.

[73] T. Fujii, "Measurements of the Energy Spectrum and the Mass Composition of Ultra-High Energy Cosmic Rays with Telescope Array Fluorescence Detectors in Monocular Mode", PhD thesis, Osaka City University, 2012.

[74] T. Abu-Zayyad *et al.*, *Physical Review D*, **88**, 112005, 2013.

[75] The Pierre Auger Collaboration, *Astroparticle Physics*, **31**, pp. 399–406, 2008.

[76] K. Kampert *et al.*, "Highlights from the Pierre Auger Observatory", *Proceedings of 32st International Cosmic Ray Conference*, 2011.

[77] J. Abraham *et al.*, *Astroparticle Physics*, **29**, pp. 243–256, 2008.

[78] M. Ave *et al.*, *Physical Review Letters*, **88**, pp. 2244–2247, 2000.

[79] M. Ave *et al.*, *Physical Review D*, **65**, 063007, 2002.

[80] A. V. Glushkov *et al.*, *JETP Letters*, **85**, pp. 131–135, 2007.

[81] A. V. Glushkov *et al.*, *Physical Review D*, **82**, 041101, 2010.

[82] K. Shinozaki *et al.*, *The Astrophysical Journal*, **571**, L117, 2002.

[83] M. Risse *et al.*, *Physical Review Letters*, **95**, 171102, 2005.

[84] G. Gelmini *et al.*, *Journal of Experimental and Theoretical Physics*, **106**, 11, 2008.

[85] J. Ellis *et al.*, *Physical Review D*, **74**, 115003, 2006.

[86] M. Risse *et al.*, *Physics Letters A*, **22**, 749, 2007.